

N ° d'ordre 2013-XXXX-XXXX

September 2013

THÈSE

Nanostructures et auto-organisation : Inhomognètés et croissance

Prèsentée devant
Ecole centrale de Marseille

pour obtenir
le GRADE DE DOCTEUR

École doctorale :
Physique et Sciences de la Matiere

Spécialité :
**SCIENCE DES MATERIAUX - PHYSIQUE - CHIMIE -
NANOSCIENCES**

par
Xianbin XU

These soutenue le jour mois année devant la Commission d'examen

Jury

NOM DU PRÉSIDENT	Professeur	Président
NOM DU RAPPORTEUR 1	Professeur	Rapporteur
NOM DU RAPPORTEUR 2	Professeur	Rapporteur
UN AUTRE MEMBRE	Maitre de Conférences	Examinateur
ENCORE UN AUTRE	Ingénieur	Examinateur
JEAN-NOËL AQUA	CNRS, INSP, Paris	Directeur de these
THOMAS FRISCH	CNRS, INLN, Nice	Co-directeur de these
UN INVITÉ	Maitre de Conférences	Invité

INSP - UMR 7588 - UPMC
INSP - 4 place Jussieu, boite courrier 840 75252 PARIS (FRANCE)

Contents

Contents	i
1 Growth of SiGe quantum dots	1
1.1 Quantum nanostructures	2
1.2 Epitaxial growth	3
1.2.1 Epitaxial growth mode	3
1.2.2 Strain relief and dislocations	5
1.2.3 Molecular Beam Epitaxy	5
1.2.4 Ostwald coarsening	6
1.3 SK growth: SiGe system	7
1.3.1 SiGe films coherently grown on a Si substrate	7
1.3.2 Wetting layer growth and surface reconstruction	8
1.3.3 First stage of the morphological evolution under high strain: nucleation	8
1.3.4 First stages of the morphological evolution under low strain: ATG instability	10
1.3.5 Growth of anisotropic islands	13
1.3.6 Additional parameters	15
1.4 Growth on a pattern	18
1.4.1 Organize self-organization	18
1.4.2 Experimental results	18
1.4.3 Issue	22
2 Formation mechanisms	23
2.1 Surface diffusion	24
2.2 Elastic chemical potential	25
2.2.1 Mechanical equilibrium	25
2.2.2 Flat surface and flat substrate case	26
2.2.3 Small-slope approximation	27
2.3 ATG instability	28
2.4 Surface chemical potential: additional effects	28
2.4.1 Wetting	28
2.4.2 Anisotropy	30

Contents

2.5	Dynamical evolution of the ATG instability	32
2.5.1	Isotropic system	32
2.5.2	Anisotropic systems	34
2.6	Growth on a pattern	36
2.6.1	Equilibrium	36
2.6.2	Nucleation barriers	38
2.6.3	Dynamical analysis	39
3	Linear analysis of the morphological instability on a pattern	41
3.1	Elastic energy density	42
3.1.1	Geometry	42
3.1.2	Mechanical equilibrium	42
3.1.3	Small-slope approximation	44
3.1.4	Surface elastic energy density	45
3.2	Equilibrium state	46
3.3	Surface energy and wetting interactions	47
3.4	Evolution equation	48
3.5	Evolution	49
3.5.1	Initial condition	49
3.5.2	Analytical results	49
3.5.3	Kinetic phase diagram	54
3.6	Articles	56
4	Isotropic nonlinear evolution of the Asaro-Tiller-Grindel'd instability	75
	Bibliography	85

Chapter 1

Growth of SiGe quantum dots

Contents

1.1	Quantum nanostructures	2
1.2	Epitaxial growth	3
1.2.1	Epitaxial growth mode	3
1.2.2	Strain relief and dislocations	5
1.2.3	Molecular Beam Epitaxy	5
1.2.4	Ostwald coarsening	6
1.3	SK growth: SiGe system	7
1.3.1	SiGe films coherently grown on a Si substrate	7
1.3.2	Wetting layer growth and surface reconstruction	8
1.3.3	First stage of the morphological evolution under high strain: nucleation	8
1.3.4	First stages of the morphological evolution under low strain: ATG instability	10
1.3.5	Growth of anisotropic islands	13
1.3.6	Additional parameters	15
1.4	Growth on a pattern	18
1.4.1	Organize self-organization	18
1.4.2	Experimental results	18
1.4.3	Issue	22

1.1 Quantum nanostructures

Quantum nanostructures were first evidenced in alternate layers of different semiconductors of thickness of atomic order [ESA 70]. Their electronic and optical properties were found to deviate substantially from those of bulk materials, which opened the path to new fundamental research and applications. The historical example concerns the discovery of Giant MagnetoResistance (GMR) [BAI 88, BIN 89] in thin-film structures composed of alternating ferromagnetic and non-magnetic conductive layers, which led to the attribution of the 2007 Nobel Prize in Physics to Albert Fert and Peter Grünberg. GMR has since been used to develop extremely small and sensitive read heads for magnetic hard-disk drives, which is now a standard technology found in nearly all computers worldwide and in some digital cameras or MP3 players. Such thin film nanostructures confine charge carriers in only one dimension and are called quantum wells, Fig. 1.1a. Fabrication of nanostructures with additional dimensional confinement became more and more important, and led to quantum wires which confine in two dimensions (2D), Fig. 1.1b, and quantum dots (QDs), in three dimensions (3D), Fig. 1.1c. We focus mainly in the following on QDs.

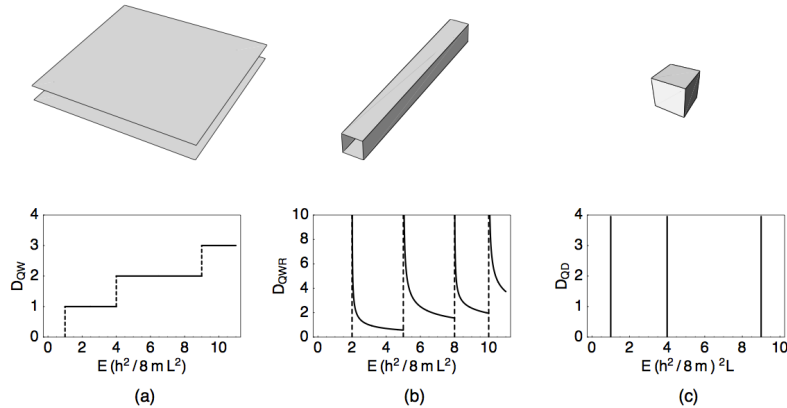


Figure 1.1: Schematic illustration of (a) a quantum well, (b) a quantum wire, and (c) a quantum dot. The planar surfaces represent infinite potential barriers separated by distance L . A charge carrier experiences quantum confinement (a) in one dimension (b) in two dimensions and (c) in three dimensions. The corresponding densities of states of free electrons within these structures are displayed in the bottom panels. The broken lines in (a) and (b) indicate the discrete levels of the confined states, from [VVE 10].

In finite geometries, when the confining dimension is large compared to the characteristic length of the charge carrier wave function, the electronic properties are similar to the ones in bulk system. However, quantization effects become apparent when the dimension of the confining region is comparable to the de Broglie wavelength of the charge carriers, $\lambda_{DB} = h/\sqrt{2\pi m^* k_B T}$, where h and k_B are the Planck and Boltzmann constants, T , the absolute temperature and m^* , the effective mass of electrons or holes. For a typical semiconductor, the de Broglie wavelength λ_{DB} of the charge carriers is of the order of $73 \sim 730 \text{ \AA}$

at 300 K and for electrons in InAs, GaAs and $\text{Si}_{1-x}\text{Ge}_x$ at room temperature, $\lambda_{\text{DB}} \approx 40$ nm, 24 nm [BOY 97] and 12 nm ($x < 0.85$) [STO 95] respectively. Thus, the confinement of the electrons wave function dramatically modifies the energy spectrum in nanostructured geometries leading to new discrete energy levels and to a dependance of the band-gap on the confinement size, see Fig. 1.1. Due to their special properties, QDs are expected to lead to new applications in micro-electronics [CRO 98, KAS 00, SIM 10b], optics [COL 94, COE 02, PRE 08a], energy production [TAL 07], solid-state quantum computation [KAN 98, PRE 08b, LIP 10, REZ 10, SIM 10a] and even in biology [MIC 05]. Here, we limit our discussion to Silicon-Germanium (SiGe) QDs, which is the paradigmatic system for electronic applications.

1.2 Epitaxial growth

There are three principal ways to fabricate QDs: lithography, colloidal chemistry and epitaxy which we study in this thesis. Epitaxial techniques offer the clear advantage of reproducibility and precise control of the growth parameters, which allows the investigation of the growth mechanisms from a fundamental perspective. Epitaxial growth concerns the deposition of an overlayer crystalline film on another crystalline substrate which dictates the film order. The word epitaxy comes for the Greek suffix *epi* (above) and *taxis* (in order manner). Epitaxial films may be grown from gaseous or liquid phase according to different epitaxial techniques. If the epitaxial film is deposited on a substrate of the same material, the process is called homoepitaxy; otherwise it is called heteroepitaxy.

1.2.1 Epitaxial growth mode

Numerous experiments have revealed three different epitaxial growth modes, see Fig. 1.2: the Frank-van der Merwe (FM) mode concerns the growth of flat single crystal films consisting of successive largely complete layers; the Volmer-Weber (VW) mode describes the formation of 3D clusters or islands separated by denuded areas of the substrate; and the Stranski-Krastanov (SK) mode, where 3D islands grow on top of a thin flat ‘wetting’ film that completely covers the substrate.

In epitaxial growth, the lattice constant is a measure of the structural compatibility between different materials. Lattice constant matching is important for achieving a good epitaxy of layers of one material on another one. For example, Gallium Arsenide, Aluminium Gallium Arsenide, and Aluminium Arsenide have almost equal lattice constants. For these lattice-matched systems, the FM and VW morphologies can be understood from thermodynamic wetting arguments based on interfacial free energies. We denote the free energy of the epilayer/vacuum interface by γ_e , that of the epilayer/substrate interface by γ_i , and that of the substrate/vacuum interface by γ_s . The FM growth mode is favored if $\gamma_e + \gamma_i < \gamma_s$. Alternatively, if $\gamma_e + \gamma_i > \gamma_s$, the VW growth is favored, as a flat layer is thermodynamically unstable against break-up into regions where the substrate is covered and others where it is uncovered. This analysis is similar to the analysis of the spreading

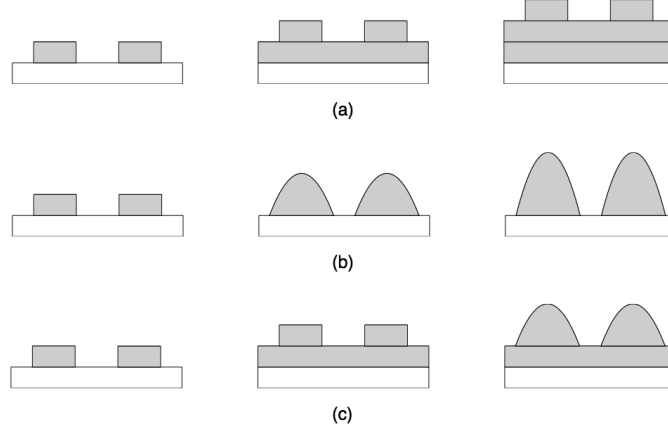


Figure 1.2: Schematic evolution during growth of the (a) Frank-van Merwe, (b) Volmer-Weber, and (c) Stranski-Krastanov heteroepitaxial growth modes.

of a liquid droplet on a solid surface where the Young equation, $\gamma_{sg} = \gamma_{sl} + \gamma_{lg} \cos \theta$, relates the surface energies of the solid/gas, solid/liquid and liquid/gas interfaces with the angle θ of the liquid/vapor interface.

On the other hand, when the film and substrate lattice parameters are significantly enough different, elastic energies also come into play and lead to the SK growth mode based on the accommodation of the misfit strain. It is characterized by the misfit parameter

$$m = \frac{a_f - a_s}{a_s}, \quad (1.1)$$

where a_s and a_f are the substrate and film lattice constants respectively. The SK growth mode results from the balance between the surface energy and the elastic energy corresponding to the misfit. In this mode, surface energy effects are initially predominant and enforce the growth of flat wetting films at low thickness. It is characterized by a layer-by-layer growth resulting in one or several complete monatomic layers, see Fig. 1.2c. In this wetting layer, the lateral lattice constant adapts itself to the substrate lattice constant thanks to lateral compression/tension, leading to a vertically tetragonal distortion (Poisson effect). In this uniformly strained layer, the elastic energy which is a volumic term increases linearly with the film thickness \bar{H} and overcomes surface effects above a thickness H_c called the critical thickness for morphological evolution. Hence, as this critical thickness is strongly dependent on the lattice misfit between the film and the substrate, and a greater misfit leads to a smaller H_c . Above H_c , the modulation of the surface above the wetting layer allows strain relaxation. In this case, the increase in the surface energy enforced by the departure from a flat geometry is overcompensated by the decrease in the strain energy enforced by the relaxation towards the film lattice constant in the upper parts of the modulation seen in the following, beside the misfit parameter m , the thickness \bar{H} of the film is of crucial importance as regards its growth.

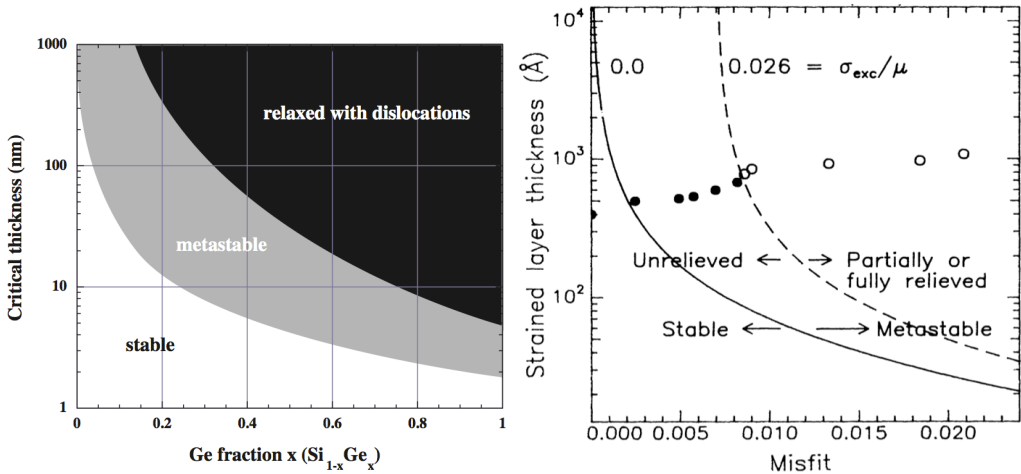


Figure 1.3: (left) The Matthews and Blakeslee critical thickness plotted against Ge fraction for pseudomorphic $\text{Si}_{1-x}\text{Ge}_x$ layers grown on bulk Si (001). Also included is a metastable curve for MBE growth at 550 °C, from [PAU 04]. (right) Thicknesses and misfits for a series of $\text{Si}_{1-x}\text{Ge}_x$ films grown at 494 °C. Fully strained (filled circles) and partially strain-relieved (open circles). The black line separates absolutely stable from metastable films, from [TSA 87].

1.2.2 Strain relief and dislocations

In hetero-epitaxy, strain relaxation can also occur via the creation of misfit dislocations. For a flat film it happens for high enough strain and/or large enough film thickness above some critical thickness, especially when one deposits an epitaxial film at low temperature so that any morphological evolution is inhibited. At equilibrium, this critical thickness corresponds to the Matthews and Blakeslee theory [MAT 74] for a flat film. However, metastable dislocation-free films with a thickness much larger than the Matthews and Blakeslee theory were growth e.g. in SiGe systems, which may be rationalised by a kinetic inhibition of the dislocation nucleation [PEO 85, TSA 87], see Fig. 1.3.

For a corrugated film where surface diffusion is at work, the morphological evolution relaxes the strain first, but additional relaxation via misfit nucleation can also be observed, especially in large islands. However, e.g. in small islands and/or in low strain system such as SiGe, dislocation-free islands are formed during the SK growth [EAG 90c] which are most wanted for applications and on which we focus in the following.

1.2.3 Molecular Beam Epitaxy

Epitaxy growth can be performed by many different techniques such as Liquid Phase Epitaxy (LPE) from liquid phase, or Vapor-Phase Epitaxy (VPE), Chemical Vapor Deposition (CVD) and Molecular Beam Epitaxy (MBE) from gaseous phase. We focus here on the latter case as it is most used for semiconductors for the fundamental investigation

1. Growth of SiGe quantum dots

of growth mechanisms.

MBE is an ultra-high vacuum technique based on the transfer of atoms onto the growing sample by means of atomic beams. The atoms or molecules are evaporated from solid sources in heated cells, collimated into beams, directed towards a heated substrate, and then deposited on the substrate. A large number of theoretical and experimental works [JOY 85, CHO 94, PIM 98] have established the foundation of the growth process which depends on the deposition rates of the different species, the surface temperature, the materials and the substrate crystallographic orientation, the presence of surface reconstruction... In MBE, the growth rate, may be adjusted to obtain a precise control of the layer composition and layer thickness. A low flux is in general used, typically of the order of a fraction of monolayer (ML) per second $\sim 10^{-2} - 10^{-1}$ ML/s. The slow income of material combined with the heating of the sample usually allows for non-equilibrium thermodynamic growth conditions. MBE was the original technique used for the growth of good epitaxial SiGe layers.

1.2.4 Ostwald coarsening

Ostwald coarsening, or ripening, is a phenomenon initially observed in solid solutions or liquid sols, which describes the change of an inhomogeneous structure over time, when small crystals or sol particles dissolve and redeposit onto larger crystals or sol particles. This phenomenon was first described by Wilhelm Ostwald in 1896 and describes the fact that large particles grow by drawing material from the smaller ones, see Fig. 1.4.

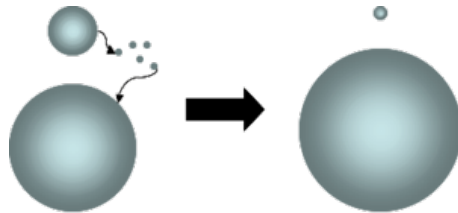


Figure 1.4: Schematic of the Ostwald coarsening process.

This thermodynamically-driven process spontaneously occurs because large particles are energetically more stable than smaller ones. This usually stems from the fact that molecules on the surface of a particle are energetically less stable than the ones already well ordered and packed in its interior. Large particles, with a lower surface to volume ratio, have therefore a lower energy. As the system tries to lower its overall energy, molecules on the surface of a small (energetically unfavorable) particle will tend to detach more frequently and diffuse through the solution to attach to the surface of a larger particle. Therefore, the small particles shrink, while larger particles continue to grow. In SK growth mode, after the appearance of islands, Ostwald coarsening may be observed as small islands on the surface shrink as surface diffusion allows mass transport towards the big islands, see Fig. 1.5.

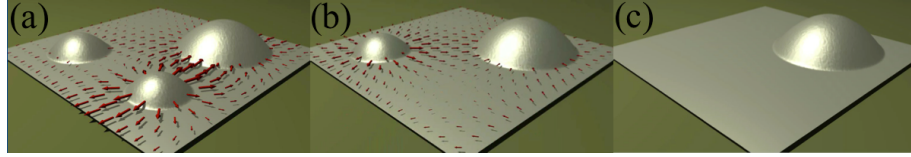


Figure 1.5: Schematic of the Ostwald coarsening process on a surface.

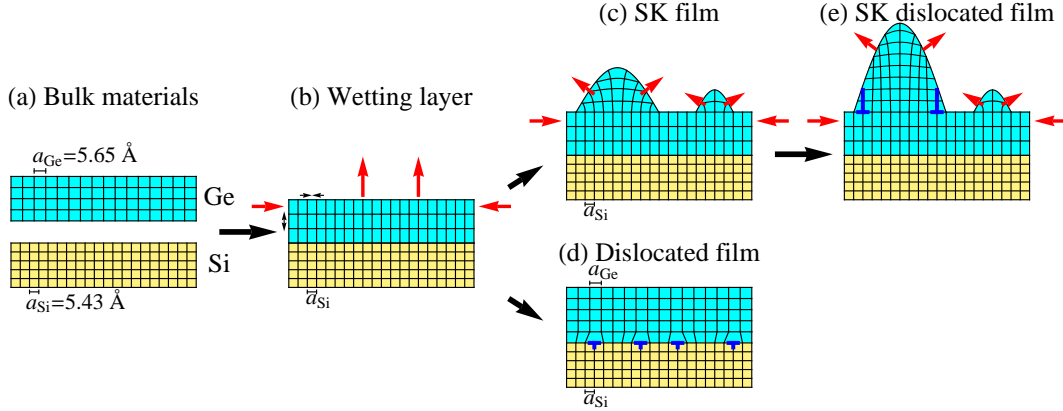


Figure 1.6: Schematic illustration of the mechanisms of heteroepitaxial growth of Ge on Si substrate. (a) The two bulk materials with different lattice parameters; (b) formation of a wetting layer; (c) the growth of islands; (d) dislocation formation on a flat film; (e) dislocation formation in a large island, such as super-domes. The red arrows show the direction of the displacements in the film.

1.3 SK growth: SiGe system

The general phenomenology of the SK growth was introduced in the previous Section. We now discuss the special case of SiGe systems. The Ge and Si lattice constants are $a_{Ge} = 5.65 \text{ \AA}$ and $a_{Si} = 5.43 \text{ \AA}$ which corresponds to a misfit of 4.2% for pure Ge on Si. For a $Si_{1-x}Ge_x$ heteroepitaxial films on Si, the misfit is related to the film composition x . According to this moderate misfit a certain number of SiGe layers can be grown coherently on top of Si and experiments revealed that coherent islands indeed occur both during growth [EAG 90a] and annealing [OZK 97b]. We discuss here the growth on Si (001) while growth on other orientations such as Si (111) is briefly discussed below.

1.3.1 SiGe films coherently grown on a Si substrate

Above a given thickness (Fig. 1.6), QDs arise during the epitaxy of SiGe on Si according to the classic SK mode, see Fig. 1.6c. However, complex mechanisms based on the competition between thermodynamics and kinetics occur during the epitaxy of $Si_{1-x}Ge_x$ on Si (001). Figure 1.7 is a kinetic morphological growth diagram describing the surface morphology as a function of the film thickness and misfit. The initial stage of layer-by-layer growth is associated with a change in the surface reconstruction (see Sec. 1.3.2),

corresponding to the regime I in Fig. 1.7. Then, as growth proceeds (\bar{H} increases), 3D islands arise either after a nucleation (see Sec. 1.3.3) or a morphological instability (see Sec. 1.3.4), depending on the Ge composition x as explained in the following. At this stage, some isotropic mounds (prepyramids) form and after some coarsening, transform into pyramids with rounded shapes and no noticeable facets. Then, as growth still pro-

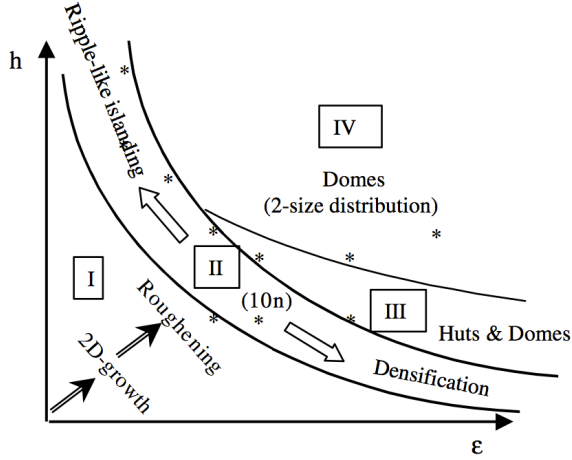


Figure 1.7: Kinetic phase diagram (at $T = 550$ °C) representing the main growth regimes of $\text{Si}_{1-x}\text{Ge}_x$ layers on Si (001) as a function of the deposited thickness \bar{H} and misfit δ , from [VOL 00].

ceeds or during annealing (see Sec. 1.3.5), the surface is covered by square-base ‘hut’ pyramids, corresponding to the regimes II and III in Fig. 1.7, by form domes or super-domes, associated to the regimes III and IV in Fig. 1.7. All the details are given in the following.

1.3.2 Wetting layer growth and surface reconstruction

The growth process begins with the formation of a flat wetting layer. Strain relief in this wetting layer occurs thanks to the formation of a $(2 \times N)$ surface reconstruction [BUT 92] that already starts for submonolayer coverages for pure Ge [SPE 91, WU 95]. Figure 1.8 shows STM images of the (2×1) reconstructed Si (001) surface (Fig. 1.8a) and the surface after deposition of Ge (Fig. 1.8b-h) which exhibits $(2 \times N)$ reconstruction. Allowing further strain relief, some roughness occurs and primarily consists of dimer vacancies [TER 92, WU 95], kinks and additional steps [ALE 88, ZHO 96].

1.3.3 First stage of the morphological evolution under high strain: nucleation

When the composition x of the $\text{Si}_{1-x}\text{Ge}_x$ film is large enough $x \gtrsim 0.5$, the film experiences a strong enough strain and 3D islands abruptly arise on top of a wetting layer above

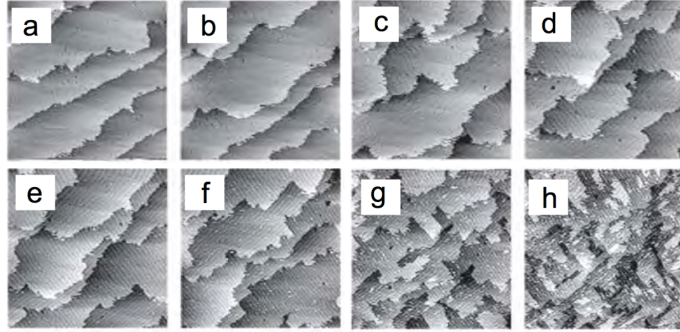


Figure 1.8: STM image of the wetting layer during the growth of Ge on Si (001) and the evolution of the $(2 \times N)$ surface reconstruction (image area: $1600 \text{ \AA} \times 1600 \text{ \AA}$, $T = 575 \text{ K}$, Ge coverages: 0, 0.33, 0.62, 0.92, 1.26, 1.58, 1.82, and 2.11 ML in (a)–(h), respectively). The distance between the trenches of the $(2 \times N)$ reconstruction decreases with coverage.

The orientation of the trenches rotates by 90° on neighboring terraces, from [SPE 91].

a critical thickness $\bar{H} > H_c$. This evolution follows a nucleation process which is intrinsic stochastic. The formation energy of an island of volume V , which is the difference between the island energy and the energy of the same amount of matter in a flat geometry, includes at least elastic and surface contributions

$$\Delta E = \Delta E^s + \Delta E^{el} \propto \gamma V^{2/3} - \alpha^{el} V, \quad (1.2)$$

where E^s is the contribution from the surface, E^{el} , the elastic energy, γ , the thick film surface energy and α^{el} is an elastic constant. As a first approximation, the elastic relaxation should give an energy proportional to the volume $\Delta E^{el} \propto -\alpha^{el}V$ while the cost in surface energy is proportional to the surface $\Delta E^s \propto \gamma V^{2/3}$. As a whole, ΔE displays a typical nucleation barrier ΔE_c , which has to be overcome to allow the growth of an island, see Fig. 1.9.

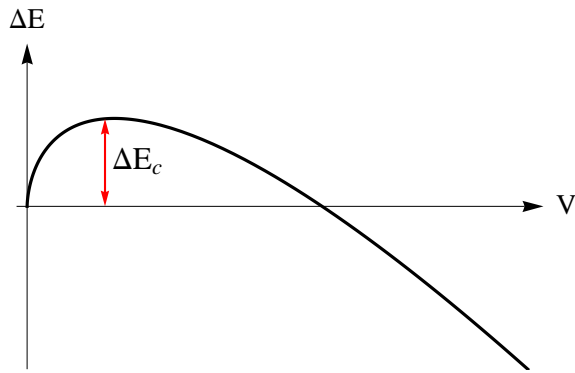


Figure 1.9: Typical variation of the energy difference between a cluster of volume V and a flat configuration.

When the film thickness is larger than some critical height so that the short-range wetting effect (which are not accounted for in Eq. 1.2) do no longer enforce

1. Growth of SiGe quantum dots

a layer-by-layer growth, nucleation of islands occurs rapidly by thermal fluctuation [VAI 00, EAG 90b, GOL 05]. These fluctuations can be quite large and their observation at 575 K showed that small nuclei with up to 270 atoms are subcritical and shrink, while large enough nuclei grow and display shallow and unfaceted mound shapes [VOI 01], see Fig. 1.11. Figure 1.10 shows that this 2D-3D transition occurs as 2D nuclei transform into ‘prepyramid’ islands when the film thickness exceeds 3 ML for pure Ge on Si (001) [EAG 90a, MO 90]. These small 3D prepyramid embryos [LI 03] are firstly formed (Fig. 1.10c-d) [RAS 03a, JES 00] and can nucleate near surface defects such as pits, step edges or irregularities on the surface reconstruction [CHE 95]. These prepyramids are

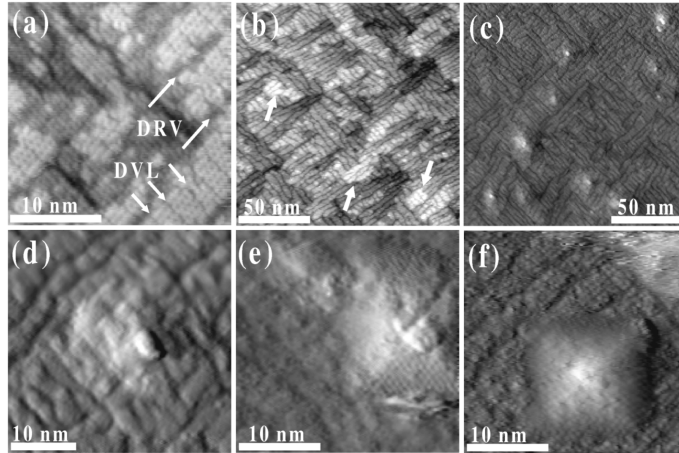


Figure 1.10: STM images showing the evolution of Ge grown on Si (001) : (a) and (b) 2D wetting layer at $\bar{H} = 2.8$ and 2.9 ML, respectively; (c) 3D prepyramid islands at $\bar{H} = 3.55$ ML; (d) initial prepyramid island at $\bar{H} = 3.55$ ML; (e) (001)-truncated (105) faceted pyramid at $\bar{H} = 3.85$ ML, and (f) completely formed (105)-faceted pyramid at $\bar{H} = 4.0$ ML. 2D islands in (b) are shown with arrows, from [VAI 00].

only present for a narrow range of Ge coverages before facets appear as explained below, see Fig. 1.10c-e. According to the stochastic character of nucleation, the resulting islands display a significant spatial disorder and size inhomogeneity.

1.3.4 First stages of the morphological evolution under low strain: ATG instability

1.3.4.1 Instability

For $\text{Si}_{1-x}\text{Ge}_x$ films on Si (001) with $x \lesssim 0.5$, strain is low enough so that nucleation is avoided and by-passed by a surface morphological instability [PID 92, CUL 92, OZK 97a, BER 98, FLO 99, TRO 00] which develops as a nucleationless process [SUT 00, TRO 00], see Fig. 1.12a. This instability was first predicted by Asaro and Tiller [ASA 72a] and re-derived by Grinfel'd [GRI 86] and called the Asaro-Tiller-Grinfel'd (ATG) instability. The typical spatial order that it produces on the surface is

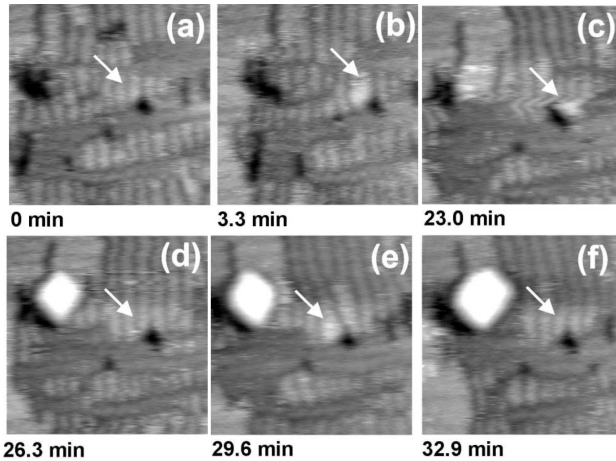


Figure 1.11: STM images taken from a movie of Ge deposited on Si (001) at 575 K. The size of the images is $500 \text{ \AA} \times 500 \text{ \AA}$. Two monolayer-high fluctuations containing about 270, 120 and 140 atoms occur at the arrowed pit after 3.3, 23.0 and 29.6 mins, respectively. Embryo sizes were measured to an accuracy of 15%, from [VOI 01].

displayed in Figs. 1.12, 1.13 and 1.14a and its Fourier transform is given in Fig. 1.14b. In this instability mode, the film develops thanks to surface diffusion a ‘ripple’ morphology above a critical thickness $\bar{H} > H_c$, see Figs. 1.12a and 1.13. Its typical wavelength λ_{ATG} depends on the balance between surface energy and strain relaxation as explained below. Figure 1.16 displays the dependence of the wavelength λ_{ATG} on the Ge concentration x . It shows that λ_{ATG} decreases with increasing x as strain relaxation is enhanced by rather small wavelengths. Besides Si/Ge systems, the ATG instability was experimentally evidenced on mechanically stressed ^4He surfaces by Balibar and co-workers [THI 92, Bal 05] following the observation of the modulation of a strained film [BOD 86]. It was also identified in polymerised polydiacetylene films deposited on their monomer substrate which induces a uniaxial stress [BER 92]. Note that this instability occurs only via surface diffusion and is not to be confused with the buckling instability of a film under an external load.

1.3.4.2 Coarsening and prepyramids

As time proceeds either during deposition or annealing, the instability keeps on growing and leads eventually in thick films to cracks as the strain concentrates in the valleys of the surface modulation, see Fig. 1.15. This singular behavior is also observed in other systems such as ^4He films and is associated with finite-time singularities of the non-linear analysis of the ATG instability as explained below. However, for thin films, experiments on SiGe systems showed that the development of the ATG instability on large time is characterized by a regular evolution without any singularity leading to the growth of rounded mounds separated by a wetting layer [SUT 00, FLO 99, TRO 00], see Fig. 1.12b. In this case, a crucial effect is the presence of wetting interactions which enforce a wetting layer

1. Growth of SiGe quantum dots

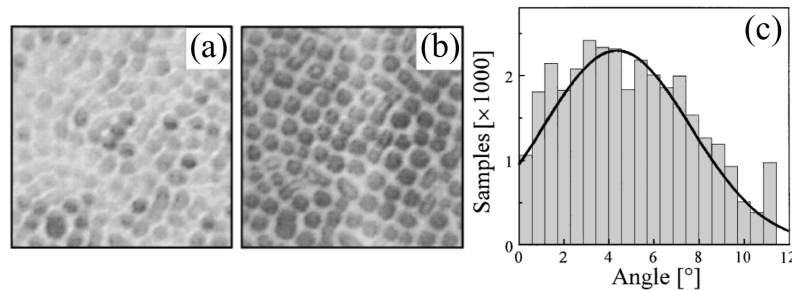


Figure 1.12: Sequence of bright-field LEEM images of the growth of a Si_{0.75}Ge_{0.25} alloy on Si (001) at T = 700 °C (growth rate: 6 ML/min). Image (a) was recorded at 54 ML alloy coverage and image (b) was taken after deposition of additional 24 ML of Si_{0.75}Ge_{0.25}. Field of view: 2 × 2 μm², from [SUT 00]. (c) Histogram of the distribution of sidewall angles of the mounds shown in (b). The solid line is a fit to a normal distribution. Note the peak at ∼11°, corresponding to the slope of (105) facets and a lack of angles above 11°, from [SUT 00].

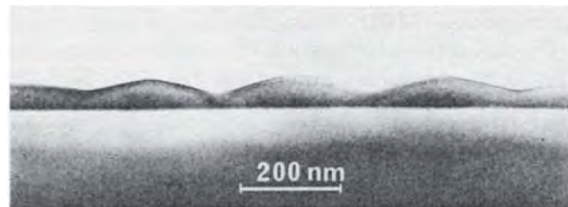


Figure 1.13: Cross-sectional TEM images, viewed along a (100) direction, from a 40 nm thick Si_{0.79}Ge_{0.21} layer grown at 750 °C on Si (001), from [PID 92].

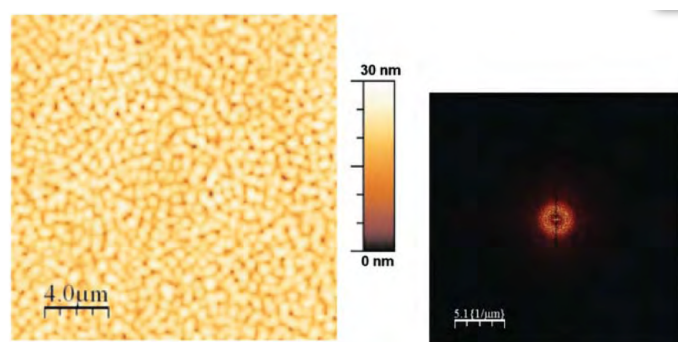


Figure 1.14: (left) AFM top-view image of a 130 nm-thick as-grown Si_{0.85}Ge_{0.15} layer on a Si (001) substrate and (right) its Fourier transform, from [AQU 11].

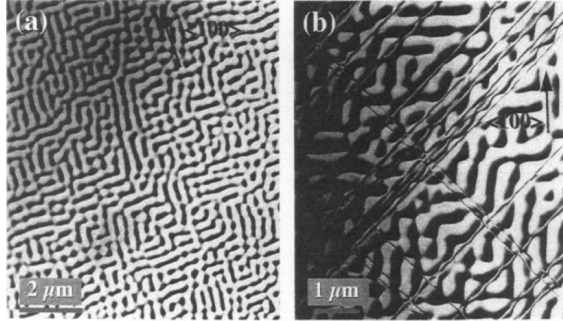


Figure 1.15: Plan view TEM images of a 500 Å thick $\text{Si}_{0.78}\text{Ge}_{0.22}$ film on Si (001) annealed at (a) 750 °C for 10 s, (b) 800 °C for 10 s , from [GAO 99b].

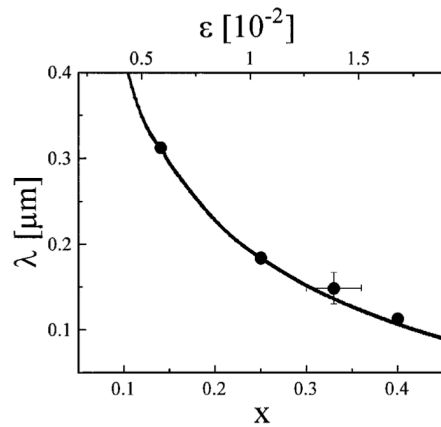


Figure 1.16: Dependence of the wavelength λ of the initial cell pattern on the Ge concentration x of the alloy film. Points denote values measured from LEEM images, from [SUT 00].

preventing the instability to deepen into the substrate, see Fig. 1.12a-b. Once the wetting layer and the islands are formed, the former allows surface mass transport so that the islands (called prepyramids) undergo some Ostwald coarsening, and increase their aspect ratio to relax more efficiently the elastic strain contrarily to the nucleation case. This evolution occurs continuously until facets develops on the islands as explained below.

1.3.5 Growth of anisotropic islands

1.3.5.1 Pyramids

In both the nucleation and the instability cases, the initial shallow islands grow and lead to faceted structures, see Fig. 1.17a-b, that we now discuss. After some coarsening, the prepyramids increase their aspect ratio until they reach a side angle of 11.3° corresponding to the (105) facets [RAS 03b], see Figs. 1.10f and 1.18. The histogram of the surface slopes in Fig. 1.12c shows a typical example of the gradual appearance of these

1. Growth of SiGe quantum dots

facets. The mostly rounded islands with a continuous distribution of side-angles evolve and display steeper slopes until (105) facets progressively form. After the appearance of (105) facets, no angle above 11.3° are seen initially and the 11.3° angle becomes more and more present above the normal distribution. Finally, when the film is not too thick, fully pyramidal islands result from the growth process. Note that the (105) facet is par-

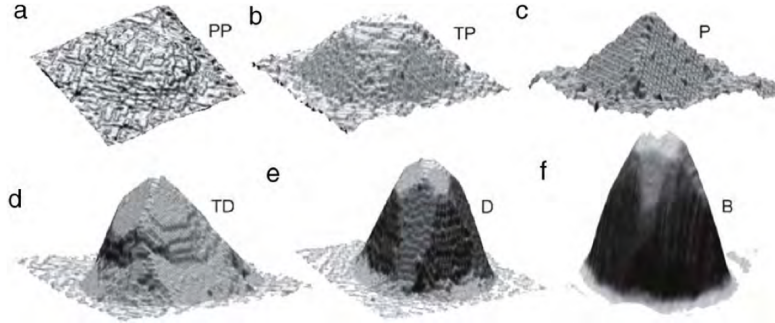


Figure 1.17: Scanning tunneling microscopy (a)–(e) and AFM (f) images of representative islands illustrating the morphological evolution during the growth of coherent SiGe islands on Si(001). Islands are prepyramids [PP, (a)], truncated pyramids [TP, (b)], pyramids [P, (c)], islands with shape intermediate between pyramids and domes [TD, (d)], domes [D, (e)], superdomes or barns [B, (f)]. Images were obtained on several samples grown under different conditions, from [RAS 06].

ticular to strained SiGe systems as it is not an equilibrium orientation but is stabilized by surface effects under stress [FUJ 02, MIG 04]. As time increases either during growth or

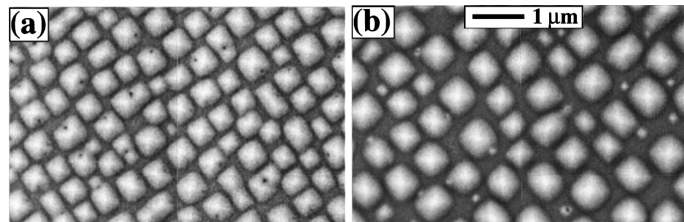


Figure 1.18: Plan-view scanning electron micrographs of $\text{Si}_{0.8}\text{Ge}_{0.2}$ on Si (001) hut cluster arrays grown by MBE at 755°C . (a) As-deposited (100 \AA thick); (b) annealed for 40 min at the growth temperature (100 \AA thick), from [FLO 00].

annealing, the surface evolves and leads to fully square-base or rectangular-base islands called ‘hut’ pyramids with four (105) facets, see Fig. 1.17c, associated with a 15% – 20% elastic relaxation [BER 09]. These pyramids may undergo some coarsening, Fig. 1.18. However, for thin enough films, the pyramid coarsening is interrupted after some time, both for in the nucleation [K⁺ 99, MCK 08] and instability [AQU 13], while it leads to new island shapes for thicker films.

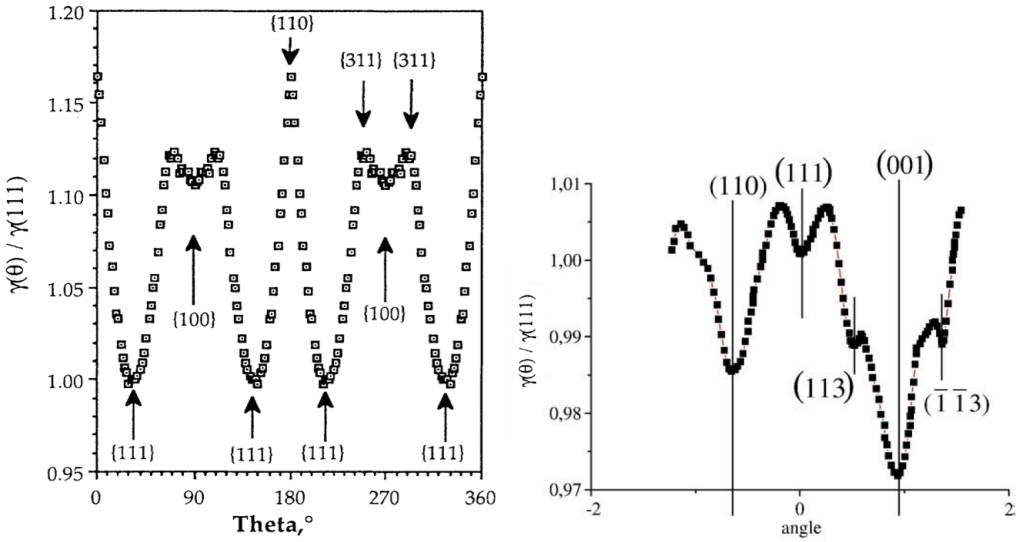


Figure 1.19: The surface energy plot $\gamma(\theta)$ for Si with θ the orientation of Si. Surface energy ratios extracted by reverse Wulff construction from voids shape imaged in high resolution down (110) axis. Averaged over three particles and symmetrized on the assumption that (110) and (001) are both mirror planes, from (left) [EAG 93a], (right) [MÜL 08].

1.3.5.2 Domes and superdomes

Either during deposition or annealing on thick enough films, hut islands progressively transform into dome islands, Fig. 1.17d-f, with (113) and (111) facets (at 25.2° and 54.7° of the (001) surface respectively) [MO 90, MED 98, FLO 99]. These facets are low energy orientations already observed in the equilibrium shape of Si, see Fig. 1.19. The formation of domes or super-domes is an efficient path to relax the strain (either by lateral elastic relaxation or by nucleation of misfit dislocations, see Fig. 1.6e), which was measured to lead to a 50% and 80% relaxation respectively [BER 09].

1.3.6 Additional parameters

1.3.6.1 Substrate orientation

The substrate orientation appeared to have an influence on the development of the ATG instability [EAG 90c, HUL 92, PCH 97, BER 09]. For example, the ATG instability is not observed on Si (111), see Fig. 1.20, while island nucleation does occur, see Fig. 1.21. The difference between these 2 orientations is their stiffness: (111) is a true facet orientation while (001) is a rather smooth one with a low stiffness and is characterized by a natural roughness, see e.g. [TER 02]. Most of the works concerning SiGe growth modes focused on heterostructures grown on Si (001) which is the dominant orientation used for device applications and which displays a wide variety of growth modes.

1. Growth of SiGe quantum dots

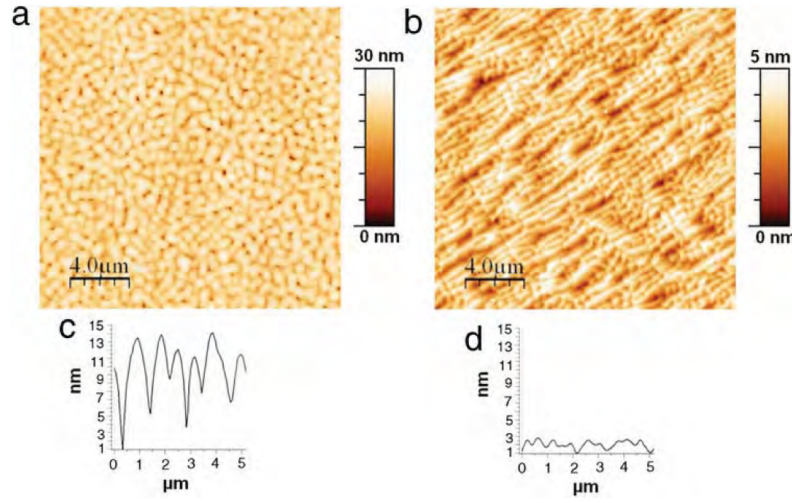


Figure 1.20: AFM top-view images of 130 nm-thick as grown $\text{Si}_{0.85}\text{Ge}_{0.15}$ layers (a) on (001) Si substrate and (b) on (111) Si substrate; side views are shaped in (c) and (d) respectively, from [AQU 11].

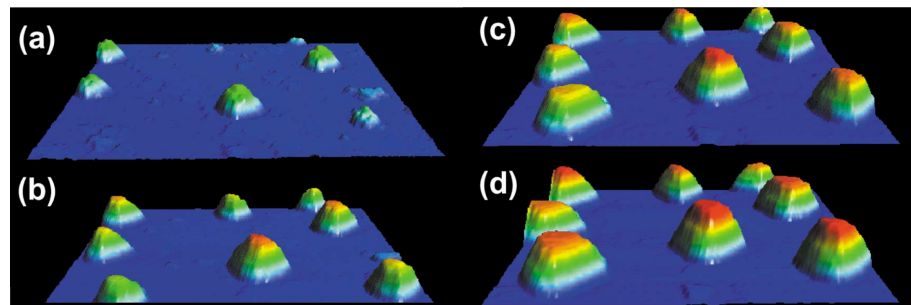


Figure 1.21: Perspective view of the growth of three-dimensional Ge islands on Si (111) after a coverage of 2.7, 4.1, 5.6, and 6.8 bilayers in (a)–(d), respectively. The complete evolution of the morphology can be followed during growth. The size of the images is 3300 Å × 3300 Å, from [VOI 01].

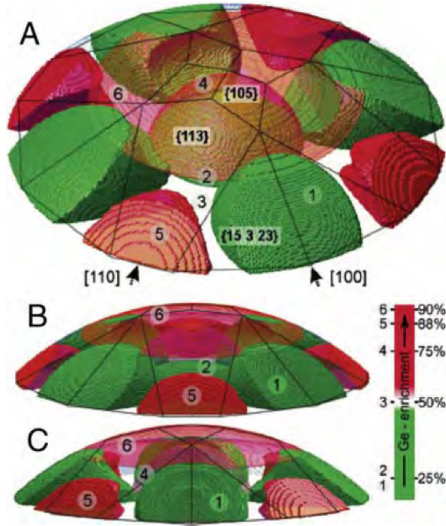


Figure 1.22: The 3D chemical model of the SiGe dome-shape islands on Si (001). (a) Perspective top view of the modeled chemical distribution within the island. The line boundaries show the faceted dome, where the facets families (braces) and the directions (brackets) are indicated. (b) and (c) Side views of the 3D model along the (011) and (001) directions, respectively. This model was constructed assuming a fourfold chemical symmetry. The colours differentiate Ge-rich (reddish) and Si-rich (green) regions. The numbers attributed to each region group refer to specific Ge content as indicated by the scale bar, from [MON 09].

1.3.6.2 Composition

Depending on the temperature, the growth of SiGe systems is in general influenced by the occurrence of alloying effects such as intermixing, segregation... [BER 12]. In this thesis, we mainly focus on the ATG instability at work in $\text{Si}_{1-x}\text{Ge}_x$ films on Si when the Ge composition $x \lesssim 0.4$ so that a change in composition is expected to have a rather small relative influence (contrarily to the case of pure Ge on Si). In addition, alloying effects can also be limited by the use of a low growth temperature ($T \sim 550$ °C). Consequently, the composition effects are not expected to be the driving force in these cases. However, for pure Ge on Si, alloying effects are significant and may also be the driving force of some evolution especially at high temperature. The decoupling of the strain and composition mass are still challenging experiments, especially X-ray diffractions. Three-dimensional chemical maps are now available and reveal, for large dome islands grown at 750 °C from Ge on Si, strong chemical fluctuations, from $x = 20\%$ up to $x = 95\%$ [RAT 04], see e.g. Fig. 1.22. For islands resulting from the deposition at 720 °C of Ge on a pit-patterned substrate, intermixing was shown to evolve and to lead to shape-oscillations [ZHA 10]. In similar conditions, difference of surface diffusivity may also lead to an anomalous smoothing of the pattern [BER 12].

1.4 Growth on a pattern

1.4.1 Organize self-organization

Good control of the QDs size and spatial organisation is important as regards their use in large-scale systems. The typical features of such nanostructures rely on the electronic properties of zero-dimensional systems as long as their sizes lie within a given range. A lower size is imposed by the constraint that the confinement potential should have at least one localized state. An upper size limit arises from the energy level spacing which should not be too small to avoid thermal smearing and evaporation of carriers from the dot. However, growing QDs with a uniform size and a good spatial order is still a challenge for experiments. QDs grown on nominal substrates display large size distribution and low spatial ordering, both in the nucleation and ATG cases (Figs. 1.10, 1.11 and 1.23), which may destroy the desired QDs properties [MIY 09]. This disorder is natural when

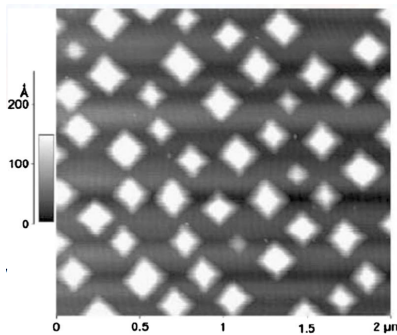


Figure 1.23: AFM images (scan size $2 \mu \times 2 \mu$) of $\text{Si}_{0.75}\text{Ge}_{0.25}$, ‘hut’ islands with $\bar{H} = 10$ nm stabilized during 18 h annealing at 550°C , from [BER 02].

the islands result from a nucleation process. However, it is disappointing as regards the islands resulting from the self-organized ATG instability which initially displays a rather good spatial order. It is linked in this case to the Ostwald coarsening at work between prepyramids and partially between pyramids. A way to produce better ordering consists in growing films on a morphologically patterned substrate. Various techniques were used to achieve substrate patterning and one may distinguish patterns created by full scale spontaneous growth processes and patterns fabricated by nanotechnological tools.

1.4.2 Experimental results

In order to control the positioning of individual islands, several groups have developed templates using lithographic patterning, such as UV-interference lithography or focused ion beam patterning [SZK 07, KIM 99, JIN 99]. We discuss in the following the influence of the pattern on the islands positioning in some typical case.

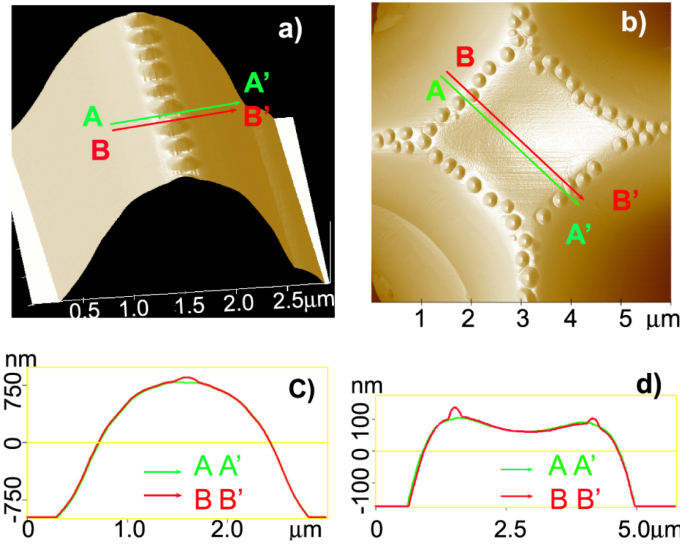


Figure 1.24: AFM images of Ge 3D island ordering on patterned Si (001) structures: (a) a stripe ridge; (b) a diamond-shaped stripe cross. (c) and (d) are the cross sections through (a) and (b) respectively, with AA' and BB' between dots and over dots. The nominal coverage is 60 ML, from [YAN 04].

1.4.2.1 Lithography

Ordering of Ge islands on patterned Si wafers using optical lithography was first proposed by Kamins et al. [KAM 97]. The size and position of Ge dots on patterned wafers was found to depend on the pattern size, and a single dot was found to grow in a given pit when the pattern period was less than 300 nm with a temperature $T = 700$ °C [KIM 98]. Using such lithography, the group of Lagally found a regular alignment of Ge dots on top of the most concave part of the surface (mesas, stripes) [YAN 04], at 650 °C on a 2.5 μm wide and 1.5 μm high stripe or on a 4.5 μm wide and 200 nm high crossed stripe, see Fig. 1.24. Using a lithographically patterned Si (001), Ge dots were also found on top of mesas with a 100 nm width and a 10 nm height [KIT 02].

Holographic lithography was also used to perform 2D pit-patterned Si templates, with periodicity in the sub-micrometer range on a centimeter-scale field. The deposition by solid-source MBE at 620 °C of Ge on these surfaces lead to the regular self-organization of islands at the bottom of the pits, contrarily to the result of the previous experiments. It was shown that a unimodal distribution of islands with dominant (111) facets and moderate aspect ratio (~ 0.37) can be achieved using such a process, see Fig. 1.25. It was rationalized on the basis of finite element calculations and molecular dynamics simulations which showed that islands in pits can have a lower misfit strain with respect to islands with the same shape but on a flat substrate [ZHO 07a].

In the Bauer's group, initial experiments showed that islands nucleation could nucleate on the pattern sidewall. In [ZHO 03b], 7 MLs of Ge were deposited at 650 °C and 0.1 Å/s with subsequent annealing at 650 °C on two different stripe-patterns. It is apparent that in

1. Growth of SiGe quantum dots

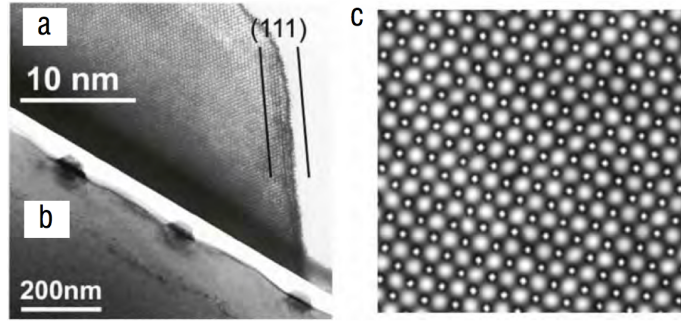


Figure 1.25: TEM cross-section of the Ge dome shaped islands which exhibit the presence of (111) facets on their side (a) and their ordering on the bottom of the pattern (b); (c) corresponding AFM image of the sample on $5 \times 5 \mu\text{m}^2$ large scale, from [ZHO 07a].

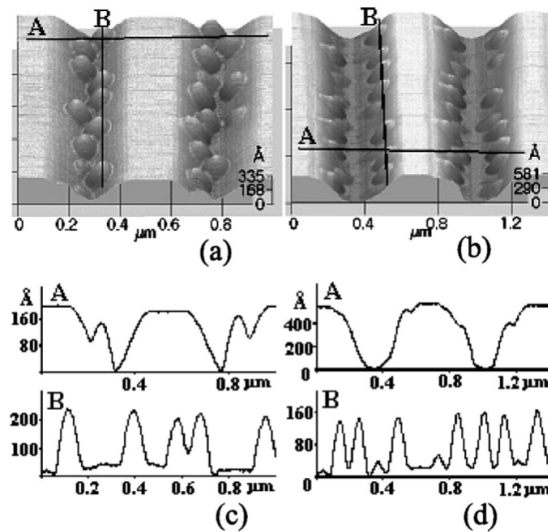


Figure 1.26: AFM images of the Ge islands from stripe pattern (a) with a 500 nm width and 175 nm height, (b) with a 670 nm width and 150 nm height, (c) height profile along lines A and B in (a), and (d) height profile along lines A and B in (b). The height scale is shown at the right-bottom of the images, from [ZHO 03b].

both patterns the islands are formed on the stripes sidewalls [ZHO 03b], see Fig. 1.26.

1.4.2.2 Electron-beam lithography

Electron-beam lithography (e-beam lithography) is one of way to overcome the limits of light diffraction and to produce features in the nanometer regime. It uses e-beam pre patterning which consists of e-beam lithography followed by etching was widely investigated. Partial overgrowth on the substrate showed that holes or pits act as preferential nucleation sites for dot formation [BOL 10]. Figure 1.27 shows an example where patterning of the Si (001) substrate was obtained by e-beam lithography before the deposition

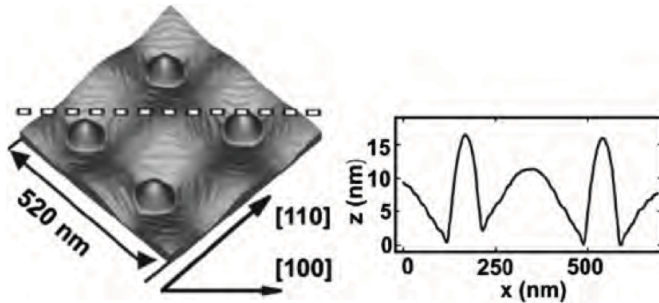


Figure 1.27: (left) AFM image of the prepatterned Si substrate with 5 MLs of Ge. (right) Line scan in (100) direction along the dashed line in (a), from [CHE 06].

of a thick Si buffer layer prior to Ge deposition. Deposition of 5 MLs of Ge at 620 °C on the well-defined Si pits with a 260 nm width and 10 nm height, resulted in well-ordered Ge domes which nucleate in the bottom of the pattern.

1.4.2.3 Focused ion beam

Patterning may also be done using Focused Ion Beam (FIB) nano-patterning which uses ions such as Ga, Si or Ge to perform the ablation of the substrate. With this tech-

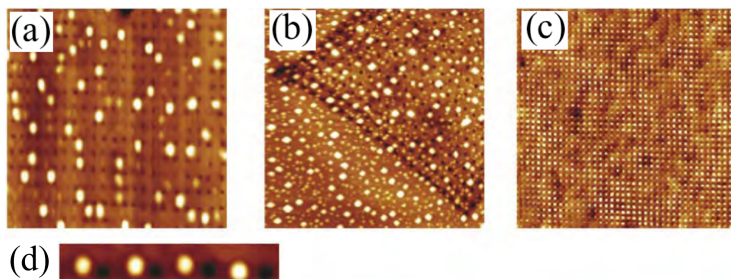


Figure 1.28: AFM images of the patterns after deposition of 7 MLs of Ge at: (a) $T = 700$ °C, hole-hole distance is 180 nm; (b) $T = 650$ °C, hole-hole distance is 180 nm; (c) $T = 550$ °C, hole-hole distance is 180 nm and (d) $T = 700$ °C, hole-hole distance is 350 nm, from [BER 09].

nique, one can precisely adjust the different pattern parameters (hole pitch, size...). Deposition of Ge on a FIB pattern with nano-pits lead in Berbezier group to three different configurations depending on the temperature, see Fig. 1.28 [BER 09]. At high temperature ($T \sim 700$ °C), Ge domes self-organized in-between the FIB holes, with four pits surrounding each Ge dot when the distance between the pits (180 nm) is comparable with the island size (100 nm), see Fig. 1.28a. When the distance between the pits becomes much larger than the island lateral size the nucleation still takes place on the flat terraces but close to the pit edges, see Fig. 1.28d. At intermediate growth temperature ($T \sim 650$ °C), islands arise randomly inside and outside the patterned areas with an equal probability, see Fig. 1.28b. Finally, at low growth temperature ($T \sim 550$ °C), Ge islands fill the

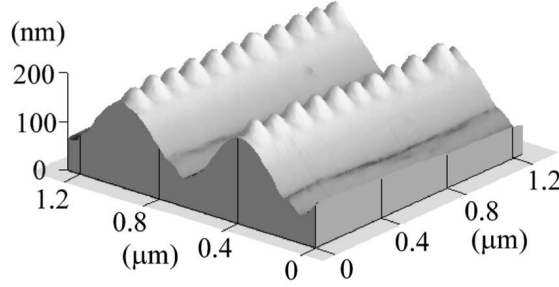


Figure 1.29: A 3D AFM image of the self-organized Ge islands on (110) oriented Si stripe mesas with a window width of $0.6 \mu\text{m}$. Self-aligned and well-spaced 1D arrays of Ge islands are formed on the ridges of the Si mesas after the deposition of 10 ML Ge, from [JIN 99].

FIB holes with a correspondence of one island per hole whatever the pattern pitch is, from 350 nm, to 200 nm and 75 nm, see Fig. 1.28c.

1.4.3 Issue

As explained above in some selected cases, experiments lead to different island positioning in seemingly similar experiments, either on top or edge of the pattern [JIN 99, KIT 02, YAN 04, SZK 04] (see Fig. 1.24, Figs.1.28a and 1.29), inside pits [ZHO 03a, ZHO 07b, BOL 10, MA 13, CHE 06] (see Fig. 1.27 and Fig. 1.28c) or even on its sidewalls [ZHO 03b] (see Fig. 1.26).

Moreover, these examples show that the location of the QDs is strongly sensitive to different parameters such as the temperature, deposition thickness, shape of the patterned substrate... These different findings reveal our incomplete understanding and control of the island self-organization on a pattern. The goal of this thesis is precisely to rationalize theoretically the influence of some basic ingredients on the growth of QDs on a pattern.

Chapter 2

Formation mechanisms

Contents

2.1	Surface diffusion	24
2.2	Elastic chemical potential	25
2.2.1	Mechanical equilibrium	25
2.2.2	Flat surface and flat substrate case	26
2.2.3	Small-slope approximation	27
2.3	ATG instability	28
2.4	Surface chemical potential: additional effects	28
2.4.1	Wetting	28
2.4.2	Anisotropy	30
2.5	Dynamical evolution of the ATG instability	32
2.5.1	Isotropic system	32
2.5.2	Anisotropic systems	34
2.6	Growth on a pattern	36
2.6.1	Equilibrium	36
2.6.2	Nucleation barriers	38
2.6.3	Dynamical analysis	39

In this chapter, we describe the mechanisms responsible for the morphological evolution leading to QDs self-assembly. We mainly focus on the ATG instability at work in $\text{Si}_{1-x}\text{Ge}_x$ films on Si (001) when the Ge composition $x \lesssim 0.4$, which corresponds to low-strained systems.

2.1 Surface diffusion

The morphological instability experienced by a strained film originates basically from the stress relaxation associated with a surface corrugation which is allowed to grow here by surface diffusion. It was first described in the framework of liquid epitaxy by Asaro and Tiller [ASA 72a] and re-derived by Grinfel'd [GRI 86] and then by Srolovitz [SRO 89], and is referred to as the ATG instability even if more complex mechanisms may also come into play in experiments. The usual description of this phenomenon is performed in the continuum limit. Surface diffusion is induced by the inhomogeneity of the local chemical potential on the surface [RIC 81]

$$\mu = \Omega \frac{\delta \mathfrak{F}}{\delta h}, \quad (2.1)$$

where Ω is the atomic volume, \mathfrak{F} is the system free energy and h is the function describing the film surface, see Fig. 2.1. In the linear response framework, surface mass currents may be considered as proportional to gradients of the surface potential

$$\mathbf{J} = -D \nabla \mu, \quad (2.2)$$

where D is the diffusion coefficient and μ , the local chemical potential [SPE 93]. The surface geometry is characterized by the film height $z = h(\mathbf{r}, t)$ with respect to the substrate, where \mathbf{r} is the 2D vector on the film/substrate interface plane, see Fig. 2.1. In the

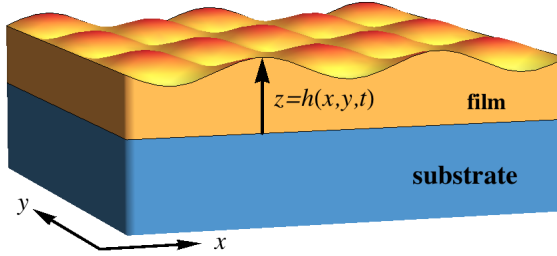


Figure 2.1: A film coherently deposited on a substrate experiences a morphological instability, where its free surface at $z = h(x, y, t)$ evolves by surface diffusion.

continuum description, mass conservation enforces

$$\frac{\partial h}{\partial t} = F + D \sqrt{1 + |\nabla h|^2} \Delta_s \mu, \quad (2.3)$$

where F is the deposition flux and Δ_s is the surface Laplacian [SPE 91]. In general, the system is characterized both by its strain energy and surface energy so that the system

free energy \mathfrak{F} is given by the sum of the surface energy $\mathfrak{F}^s = \int \gamma \sqrt{1 + |\nabla h|^2} d\mathbf{r}$, where γ is the film surface energy, and the elastic energy $\mathfrak{F}^{el} = \int_{z < h(\mathbf{r})} \mathcal{E}^{el}(\mathbf{r}, z) d\mathbf{r} dz$, where \mathcal{E}^{el} is the elastic energy density. In the original ATG instability, the surface energy γ is basically constant and depends neither on the film height nor on its orientation. The functional derivative Eq. 2.1 therefore leads to

$$\mu(\mathbf{r}) = \Omega \gamma \kappa(\mathbf{r}) + \Omega \mathcal{E}^{el}[\mathbf{r}, z = h(\mathbf{r})] + \mu_0, \quad (2.4)$$

where μ_0 is the crystal reference formation energy and κ is the mean curvature

$$\kappa = -\frac{\Delta h + h_y^2 h_{xx} + 2h_x h_y h_{xy} + h_x^2 h_{yy}}{(1 + |\nabla h|^2)^{3/2}}. \quad (2.5)$$

The contribution $\gamma \kappa(\mathbf{r})$ in (2.4) stabilizes the surface and favors its smoothing in order to reduce the surface energy of a corrugation. On the other hand, the elastic contribution described in next Section, favors a morphological evolution in order to reduce the strain originating from the lattice parameter misfit.

2.2 Elastic chemical potential

2.2.1 Mechanical equilibrium

The elastic contribution to the chemical potential is related to the elastic energy density at the free surface $\mu^{el} = \Omega \mathcal{E}^{el}[\mathbf{r}, z = h(\mathbf{r})]$ where

$$\mathcal{E}^{el} = \frac{1}{2} \boldsymbol{\sigma}_{ij} \mathbf{e}_{ij}, \quad (2.6)$$

where $\boldsymbol{\sigma}$ and \mathbf{e} are the stress and strain tensors. Mechanical equilibrium is supposed to be achieved as it occurs on a time scale much shorter than the time scale of the instability. As a consequence, the displacement vector \mathbf{u} satisfies the Navier-Cauchy equations

$$\partial_j \boldsymbol{\sigma}_{ij} = \mathbf{0}, \quad (2.7)$$

with summation over repeated indices $i, j = x, y, z$. We consider here isotropic elasticity, where the stress tensor $\boldsymbol{\sigma}$ is related to the strain tensor \mathbf{e} defined with respect to the stress-free reference state by

$$\boldsymbol{\sigma} = \frac{Y}{(1+\nu)} \left[\mathbf{e} + \frac{\nu}{(1-2\nu)} \text{Tr}[\mathbf{e}] \mathbb{1} \right], \quad (2.8)$$

with the Young modulus Y , Poisson ratio ν and the identity matrix $\mathbb{1}$. The Navier-Cauchy equations reduce to the Partial differential equations

$$\nabla(\text{div } \mathbf{u}) + (1-2\nu)\Delta \mathbf{u} = \mathbf{0}. \quad (2.9)$$

2. Formation mechanisms

Elastic anisotropy could be included at that stage but we do not consider it in order to simplify our calculations and because it is rather small on Si (001).

The solution of the displacement vector may be fully determined considering appropriate boundary conditions corresponding to the geometry under study. In MBE, the film grows in an ultra-high vacuum chamber so that the film surface is in contact with a vanishing vapour pressure. Moreover the surface stress is usually negligible in SiGe systems [LEV 07] so that the film surfaces is free of stress $\sigma \cdot n = 0$, with n , the unit vector perpendicular to the film free surface. Finally, the coherence between the film and substrate, which is at work in experimental observations, enforces the continuity of displacements and forces at the film/substrate interface.

If one considers as done in the following that the film and substrate have identical elastic constants (Young modulus and Poisson ratio), the solution in the film is identical to the solution of a unique semi-infinite film under the external bi-axial strain corresponding to the misfit m . Different elastic constants lead in fact to usually small differences in the resulting equations [AQU 07]. In the following, the displacements in the film and substrate are all computed with respect to the substrate reference state chosen to be the substrate free of deformation. Thus, the displacement in the film is $\tilde{\mathbf{u}}^f = \mathbf{u}^f - m\mathbf{r}$, where $\tilde{\cdot}$ denotes properties defined with respect to the film reference state, so that $e_{ij} = \frac{1}{2}(\partial_j u_i + \partial_i u_j)$ in the substrate and $\tilde{e}_{ij} = \frac{1}{2}(\partial_j u_i + \partial_i u_j) - m\mathbb{1}_{ij}$ in the film. Finally, the stress tensor in the film is given by

$$\sigma^f = \frac{Y}{1+\nu} \left[e + \frac{\nu}{(1-2\nu)} \text{Tr}[e]\mathbb{1} \right] - \frac{Y}{1-2\nu} m\mathbb{1}. \quad (2.10)$$

2.2.2 Flat surface and flat substrate case

We first consider the simplest case where a flat film lies on a flat substrate $h(\mathbf{r}) = \bar{H}$, where \bar{H} is the mean film thickness. In order to solve for the displacements, we suppose that \mathbf{u} does not depend on $\{x,y\}$, thanks to the invariance in these directions. We also search for a solution where the stress does not depend on $\{x,y\}$ and note with a $\bar{\cdot}$ such solutions. The Navier-Cauchy equations Eq. 2.7, lead to $\partial_z \bar{\sigma}_{xz} = \partial_z \bar{\sigma}_{yz} = \partial_z \bar{\sigma}_{zz} = 0$, which implies that $\bar{\sigma}_{xz}$, $\bar{\sigma}_{yz}$ and $\bar{\sigma}_{zz}$ are finally all constant. Thanks to the inverse relation of (2.8) giving e as a function of σ , one finds that $\partial_z \bar{u}_i = c^e$ thanks to the hypothesis $\partial_j \bar{u}_i = 0$, with $i = x, y, z$ and $j = x, y$. As a result, we get

$$\begin{pmatrix} \bar{u}_x \\ \bar{u}_y \\ \bar{u}_z \end{pmatrix} = \begin{pmatrix} a_x z + b_x \\ a_y z + b_y \\ a_z z + b_z \end{pmatrix}, \quad (2.11)$$

with 6 unknowns a_i and b_i with $i = x, y, z$ both in the film and substrate, to be set by the boundary conditions.

Deep in the substrate, when $z \rightarrow -\infty$ the displacement $\bar{\mathbf{u}}^s \rightarrow 0$ corresponding to a Si substrate free of stress. Thus, $a_i^s = b_i^s = 0$ so that $\bar{\mathbf{u}}^s = 0$. At the interface $z = 0$, the continuity of the displacements enforces $\bar{\mathbf{u}}^f|_{z=0^+} = \bar{\mathbf{u}}^s|_{z=0^-} = 0$ so that $b_i^f = 0$. The

continuity of forces at the coherence film/surface interface leads to

$$\bar{\sigma}^f \cdot \mathbf{z}|_{z=0^+} = \bar{\sigma}^s \cdot \mathbf{z}|_{z=0^-} = \mathbf{0}, \quad (2.12)$$

as $\bar{\mathbf{u}}^s = \mathbf{0}$. Thanks to Eq. 2.10 we get

$$\bar{\sigma}^f \cdot \mathbf{z}|_{z=0^+} = \frac{Y}{2(1+v)} \begin{pmatrix} a_x^f \\ a_y^f \\ \frac{2(1+v)}{1-2v} \left(\frac{1-v}{1+v} a_z^f - m \right) \end{pmatrix} = \mathbf{0}, \quad (2.13)$$

so that $a_x^f = a_y^f = 0$ and $a_z^f = \frac{1+v}{1-v} m$. Eventually, the displacement in the substrate and film with a flat film surface and flat film/substrate interface are respectively

$$\bar{\mathbf{u}}^s = \mathbf{0}, \quad \bar{\mathbf{u}}^f = \begin{pmatrix} 0 \\ 0 \\ m \frac{1+v}{1-v} z \end{pmatrix}. \quad (2.14)$$

Note that in this special geometry, the force along z is invariant along z so that the force continuity (2.12) enforces automatically the free-film surface boundary condition $\tilde{\sigma}^f \cdot \mathbf{z} = \mathbf{0}$ at $z = \bar{H}$. Finally given this solution, one gets the elastic energy density in the film

$$\bar{\mathcal{E}}^{el} = \frac{Ym^2}{1-v}. \quad (2.15)$$

2.2.3 Small-slope approximation

In the general case however, see Fig. 2.1, it is not possible to solve for the displacements analytically as the boundary conditions at the free film surface or interface cannot be solved exactly for any arbitrary shape. It can be done however in the small-slope approximation, when one can write

$$h(\mathbf{r}) = \bar{H} + \epsilon h_1(\mathbf{r}), \quad (2.16)$$

where \bar{H} is the mean film height and ϵ is a small parameter (derivatives of h_1 are supposed finite). This small slope approximation is justified in the early stage of the instability and as long as the system involves small slopes, which is the case for pyramids where (105) facets with 11.3° side angles are the steepest orientations, see Fig. 1.12c. As a result, one can search for a solution for \mathbf{u} as $\mathbf{u} = \bar{\mathbf{u}} + \delta\mathbf{u}$ where $\delta\mathbf{u}$ is expanded in series of ϵ . Thanks to the symmetry of the system and to the usual properties of Laplacians. Eq. 2.4 may be conveniently solved using Fourier transforms with respect to \mathbf{r}

$$\mathcal{F}[h](\mathbf{k}) \equiv \hat{h}(\mathbf{k}) = \frac{1}{(2\pi)^2} \int d\mathbf{r} e^{i\mathbf{k}\cdot\mathbf{r}} h(\mathbf{r}), \quad (2.17)$$

with the wave-vector \mathbf{k} . The solution for \mathbf{u} at first order in ε will be given in the next Chapter [AQU 10a] and the corresponding elastic energy density (2.6) at *first order* is then

$$\mu^{el}(\mathbf{r}) = \Omega \bar{\mathcal{E}}^{el} \{1 - 2(1+\nu)\mathcal{H}_{ii}(h)\}, \quad (2.18)$$

in terms of the generalized Hilbert transform defined as

$$\mathcal{H}_{ij}(h) = \mathcal{F}^{-1}[k_i k_j / |\mathbf{k}| \hat{h}(\mathbf{k})]. \quad (2.19)$$

It is the generalization to 2D variables of the usual Hilbert transform defined in 1D as $\mathcal{H}(f)(x) = \frac{1}{\pi} \text{P.V.} \int_{-\infty}^{+\infty} dy \frac{f(y)}{x-y}$ with P.V. principal value.

2.3 ATG instability

Thanks to the solution of the elastic equilibrium, the evolution equation (2.3) with (2.18) may be solved exactly in Fourier space in the small-slope approximation. One then finds that a perturbation $h(\mathbf{r}) = \bar{H} + \delta h_1 e^{ik \cdot r + \sigma t}$ evolves exponentially with time with the growth rate [ASA 72a, ASA 72b]

$$\sigma = |\mathbf{k}|^3 - \mathbf{k}^4, \quad (2.20)$$

in the dimensionless units defined with the length scale

$$l_0 = \frac{\gamma}{2(1+\nu)\bar{\mathcal{E}}^{el}}, \quad (2.21)$$

and time scale

$$t_0 = \frac{l_0^4}{D\gamma}. \quad (2.22)$$

The non-analytical term $|\mathbf{k}|$ in (2.20) signals the long range of the driving elastic interactions, and competes with the local and analytical term depicting the surface smoothing induced by the surface energy. The growth rate is positive for $|\mathbf{k}| \leq 1$, see Fig. 2.2, and the morphological instability occurs for perturbations with a large wavelength, beyond the critical wavelength $2\pi/l_0$. The maximum value in Fig. 2.2 corresponds to $k_{ATG} = 3/4$ and is related to the wavelength $\lambda_{ATG} = 2\pi/k_{ATG}$ in experiments, see Fig. 1.14. As the elastic energy density, the growth rate (2.20) does not depend on the film height \bar{H} , as the elastic problem is equivalent to a semi-infinite externally strained film (Section above) which satisfies translational invariance in the growth direction.

2.4 Surface chemical potential: additional effects

2.4.1 Wetting

In very thin films of thickness of the order of a few atomic lengths, wetting interactions between the film and the substrate come into play and yield a dependence of the surface

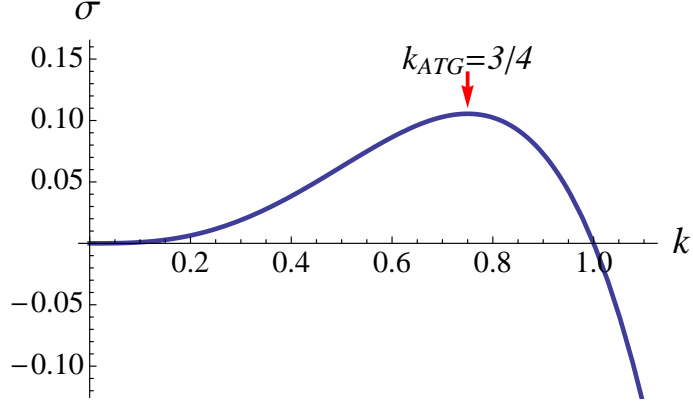


Figure 2.2: Variation of the basic growth rate $\sigma = |k|^3 - k^4$ of the ATG instability.

energy on the film height h [GAO 99a, MÜL 96, SPE 97, CHI 94]. Similarly to what is found in liquids, this dependence results from the change over a few atomic distances of the local environment of a particle, which difference rules the surface energy, see Fig. 2.3. These interactions are at the origin of the growth of the initially flat wetting layer which

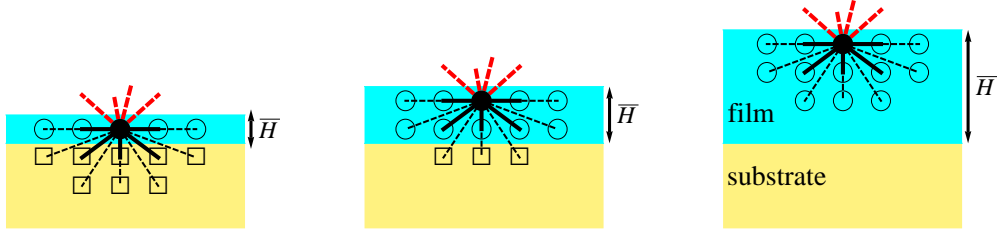


Figure 2.3: Schematic representation of a wetting layer on a flat substrate, where the local environment of a particle (related to the surface energy) depends on the film thickness H .

minimizes the wetting energy below a critical height [GAO 99a, MÜL 96]. They are also responsible for the existence of a thin wetting layer between islands once they are formed. For a Ge film on a Si substrate, *ab-initio* calculations show that the film surface energy decreases monotonically from 90 to 60 meV/Å² from a bare Si surface to a 5 layers film [LU 05], see Fig. 2.4. In the following, we model this smooth variation as [GAO 99a, MÜL 96]

$$\gamma(h) = \gamma_f [1 + c_w \exp(-h/\delta_w)], \quad (2.23)$$

where γ_f is the thick film surface energy, c_w and δ_w are the amplitude and the depth of the wetting interactions. The wetting interactions may be described in the continuum framework by considering that γ depends on the *local* film thickness h , $\gamma = \gamma(h)$. The functional derivative (2.1) then leads to

$$\mu = \Omega \gamma(h) \kappa + \Omega \frac{d\gamma}{dh} \frac{1}{\sqrt{1 + |\nabla h|^2}} + \mu^{el} + \mu_0. \quad (2.24)$$

2. Formation mechanisms

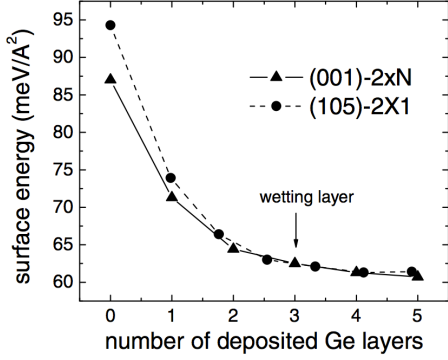


Figure 2.4: Surface energy of Ge/Si (105) and Ge/Si (001) as a function of the number of deposited Ge layers.

The second term in the r.h.s. of (2.24) (referred to as the wetting potential) enforces a modification of the spectrum of the ATG instability growth rate with a general lowest-order \mathbf{k}^2 term

$$\sigma(\mathbf{k}; \bar{H}) = -\frac{d^2\gamma}{dh^2}(\bar{H}) \mathbf{k}^2 + |\mathbf{k}|^3 - \mathbf{k}^4. \quad (2.25)$$

Hence, the growth rate σ gets here an explicit dependance on the film thickness \bar{H} , due to the translational invariance breaking the wetting interactions. A priori $d^2\gamma/dh^2$ is positive and vanishes for large \bar{H} , see Fig. 2.4. The first negative term in (2.25) qualitatively changes the behaviour of the growth rate, see Fig. 2.5. For small \bar{H} , $\sigma(\mathbf{k}; \bar{H})$ is always negative and the instability does not develop. On the contrary, for \bar{H} larger than some wetting dependent critical thickness H_c , $\sigma(\mathbf{k}; \bar{H})$ exhibits positive values over a finite wavelength interval and the instability can develop. These conclusions agree with the experimental observation that the morphological evolution does not occur below a critical thickness H_c (Sec. 1.3.2). We can solve for H_c by looking for the thickness where $\sigma(\mathbf{k}; \bar{H}) = 0$ has a non-zero solution where $\partial\sigma(\mathbf{k}; \bar{H})/\partial|\mathbf{k}| = 0$ (corresponding to a maximum), and find

$$H_c = -\delta_w \ln \left(\frac{\delta_w^2}{4c_w} \right). \quad (2.26)$$

2.4.2 Anisotropy

Anisotropy is also known to be a crucial factor in crystal growth which dictates both equilibrium and growth shapes [WUL 01, PIM 98]. For Si crystals, Fig. 1.19 shows different facets belonging to the equilibrium shape $\gamma_{111} \geq \gamma_{110} \geq \gamma_{113} \geq \gamma_{100}$ [BER 95, EAG 93b]. It certainly plays a role in the ATG instability since it was shown experimentally that it can develop on Si (001) and not on Si (111) and also since (105) facets quickly appear on islands. (105) facets are particular to strained SiGe systems (Sec. 1.3.5) as it is not an equilibrium orientation but is stabilised by the surface reconstruction under stress, as shown by *ab-initio* calculations [MIG 04]. In addition, it is expected that the

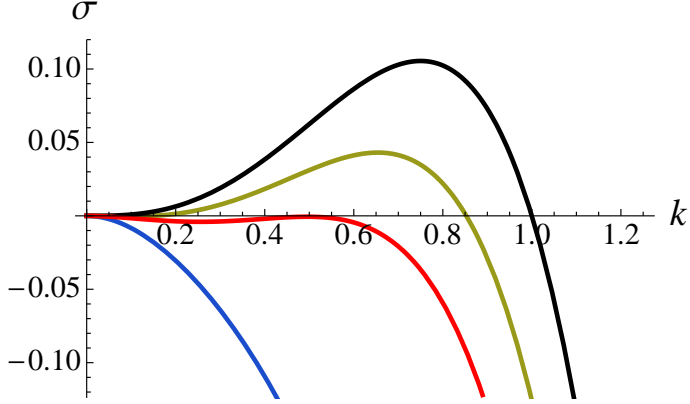


Figure 2.5: Variation of the basic growth rate $\sigma(k; \bar{H})$ for, from top to bottom, $c_w = 0$ and then $\bar{H} = 9, 8.3, 7$ $\delta_w = 0.1$.

(105) orientation is a stiffer orientation compared to (001) as well-defined (105) facets are clearly visible as opposed to the roughness of the (001) orientation [TER 02]. Thus, a crucial anisotropy which is missing in the basic ATG modelization is the surface energy anisotropy which dependence on the surface local orientation \mathbf{n} dictates equilibrium shapes [WUL 01, NOZ 91]. When one accounts for both anisotropy and wetting effects $\gamma = \gamma(h, \mathbf{n})$ and the surface chemical potential which results from the functional derivative reads

$$\begin{aligned} \mu = & \gamma(\mathbf{n}, h)\kappa - \frac{2}{\sqrt{1+|\nabla h|^2}} h_j h_{ij} \frac{\partial \gamma}{\partial h_i} - \sqrt{1+|\nabla h|^2} \left[h_{ij} \frac{\partial^2 \gamma}{\partial h_i \partial h_j} + h_i \frac{\partial^2 \gamma}{\partial h \partial h_i} \right] \\ & + \frac{\partial \gamma}{\partial h} \frac{1}{\sqrt{1+|\nabla h|^2}} + \mu^{el} + \mu_0. \end{aligned} \quad (2.27)$$

The linear analysis of the evolution equation leads to the growth rate in units of l_0 (2.21) and t_0 (2.22)

$$\sigma = -\frac{d^2 \gamma}{dh^2}(\bar{H}, \mathbf{n}_0) \mathbf{k}^2 + |\mathbf{k}|^3 - \tilde{\gamma}(\bar{H}, \mathbf{n}_0) \mathbf{k}^4, \quad (2.28)$$

with the initial orientation \mathbf{n}_0 which symmetry is supposed to enforce $\frac{\partial \gamma}{\partial h_i} \mathbf{n}_0 = 0$. In Eq. 2.28, we used the dimensionless surface stiffness $\tilde{\gamma} = (\gamma + \partial^2 \gamma / \partial h_i \partial h_i) / \gamma_f$, which generalizes the 2D formula $\gamma + \gamma''(\theta)$. Usually $\tilde{\gamma} > 1$ so that the surface stiffness naturally weakens the instability growth rate and diminishes the interval of unstable wave-vectors.

2.5 Dynamical evolution of the ATG instability

2.5.1 Isotropic system

2.5.1.1 Without wetting

The linear analysis is satisfactory for the description of the first stage of the ATG instability. However, the long time dynamics requires the analysis of non-linear effects, which avoid the trivial exponential increase of the instability. Non-linear terms are present both in the elastic energy due to the boundary conditions and in the decay of the wetting interactions. The first non-linear analyses concerned the elastic non-linear terms [YAN 93, SPE 94, XIA 02, KOH 03, GOL 03, PAN 06], which can be handled either with finite-element elasticity calculations, within the small-slope approximation or with a decomposition of the surface shape in terms of cycloids. The long time dynamics of the ATG instability was shown to be characterized by finite-time singularities associated with blow-up solutions: after the growth of instability initial corrugation, deep crack-like grooves grow on the surface before a singularity occurs for a dimensionless time $t = 0.07$, see Fig. 2.6. In two dimensions, the elasticity problem may be reduced to a boundary integral equation which can be solved analytically, showing the deepening of a groove [YAN 93, SPE 94]. In 3D, the cusp deepening was numerically evidenced based on a perturbation analysis both near the instability threshold in the small-slope approximation [GOL 03], or using a numerical implementation of the non-linear elastic analysis [PAN 06], see Fig. 2.7. This singular behavior recalls the cycloid solution of the elastic problem in 2D where stress is concentrated at the cusp and is relaxed elsewhere when the cycloid wavelength is larger than some critical value [CHI 93]. The singular stress concentration [SPE 94, CHI 93] is related to the occurrence in experiments of dislocations in strained thick films along singular points in the valleys of the surface corrugation [SPE 94, CHI 93].

2.5.1.2 With wetting

For thin films however, wetting interactions completely change this scenario. Combined with non-linear elastic effects they can lead to a regularized dynamics and avoid the formation cusp-like singularities [AQU 07]. The numerical resolution of the dynamical equation describing the ATG instability with wetting effects, i.e. (2.3) with (2.24) and with the result of μ^{el} at first non-linear order (see below) leads at its beginning to growing mounds. Once their bases touches the region where wetting is relevant (i.e. at a low thickness), their growth slows down and a flat wetting layer spreads in between the mounds, see Fig. 2.8. The result of this analysis is that the combination of both non-linear non-local elastic effects and even small wetting interactions allows the regularisation of the instability long-time dynamics. During annealing, these isotropic islands undergo a non-interrupted coarsening, similar to the Ostwald coarsening where large islands with a lower chemical potential grow at the expense of small ones. In order to describe quantitatively the dynamics of island growth, the surface roughness $w(t) = (\langle h^2 \rangle - \langle h \rangle^2)^{1/2}$, number of

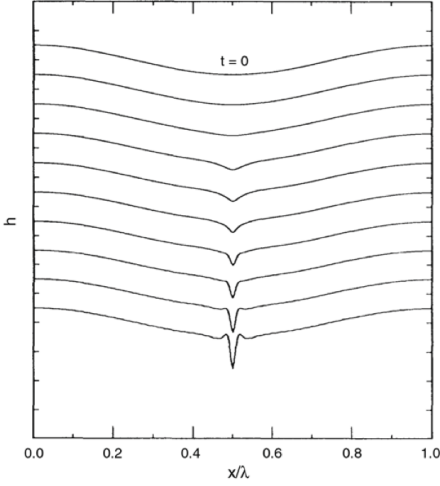


Figure 2.6: The temporal evolution of the surface profile under the influence of a bulk stress, from [YAN 93].

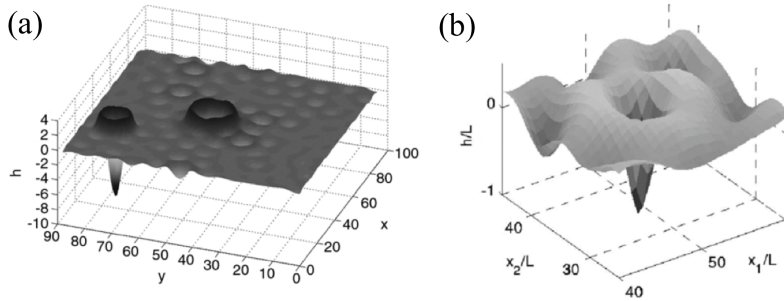


Figure 2.7: Blow-up solutions of the morphological instability from (a) [GOL 03], and (b) [PAN 06].

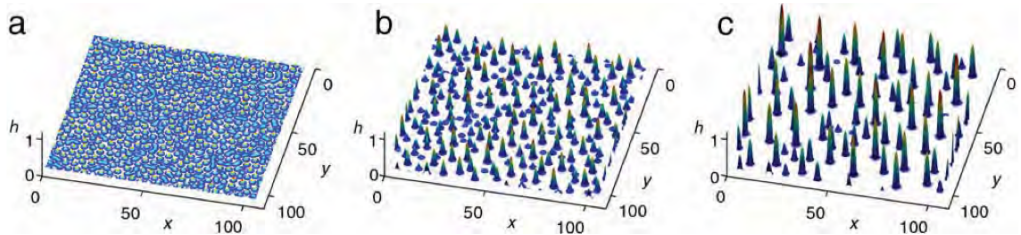


Figure 2.8: Non-interrupted coarsening resulting from the long time non-linear evolution of the ATG instability regularised with wetting interactions. The initial picture displays the initial exponentially growing stage of the instability, which is followed by the non-linear regime where islands separated by a wetting layer grow thanks to surface diffusion which allows Ostwald coarsening, from [AQU 07].

2. Formation mechanisms

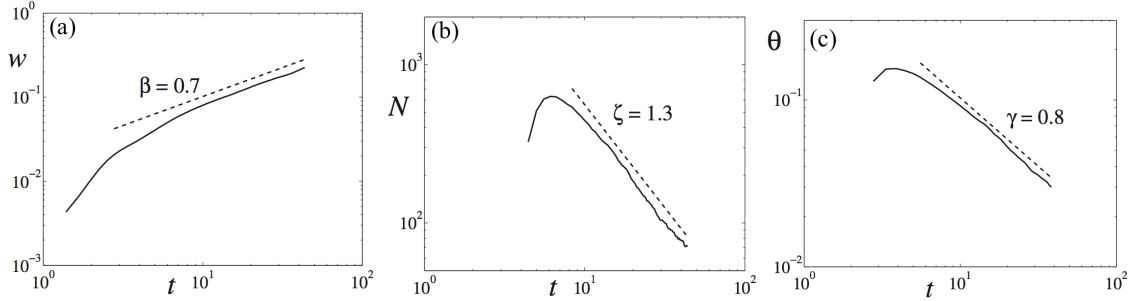


Figure 2.9: Evolution of (a) the roughness, (b) the number of islands, and (c) the surface coverage as function of time in 3D, from [AQU 07].

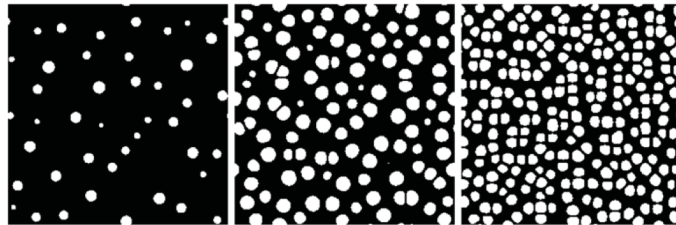


Figure 2.10: Different non-linear regimes of the wetting ATG instability for increasing deposition flux (from left to right, 10^{-4} , 10^{-2} and 10^{-1} ML/s in $128 l_0 \times 128 l_0$), corresponding respectively to deposition thickness $h_d = 13, 105, 283$ ML, from [AQU 10b].

islands $N(t)$, and the island surface coverage $\theta(t)$ were computed. 3D simulations revealed a non interrupted coarsening with power-law behaviours $w(t) \sim t^\beta$, $N(t) \sim 1/t^\zeta$, and $\theta(t) \sim 1/t^\gamma$, see Fig. 2.9. Over the last time decade of the 3D simulations, one finds $\beta=0.7$, $\zeta=1.3$, and $\alpha=0.8$ [AQU 07]. These exponents are significantly departing from the classical exponents associated with Ostwald coarsening for 3D islands with a 2D diffusion.

As already noticed, in addition to the regularization of the instability, the wetting interactions break the system invariance in the growth direction. As a consequence, the long-time dynamics of the instability explicitly depends on the deposition flux since the evolution equation explicitly depends on the film thickness \bar{H} which grows as Ft . As a result, different non-linear regimes ruled by the deposition flux F are found, characterized by different coarsening dynamics and spatial order, see Fig. 2.10. For a large enough flux, coarsening is frozen and islands mainly grow by collecting new deposited material.

2.5.2 Anisotropic systems

The first non-linear stage of the instability leads mainly to isotropic mounds. However, on larger time scales, anisotropy is unavoidable experimentally as the mounds transform into pyramids with well-defined facets (Sec. 1.3.5). To describe this growth, one must include the crystalline anisotropy in the instability evolution [ZHA 00, CHI 04, CHI 06]. It may be done in the continuum framework by considering an ad-hoc and continuum

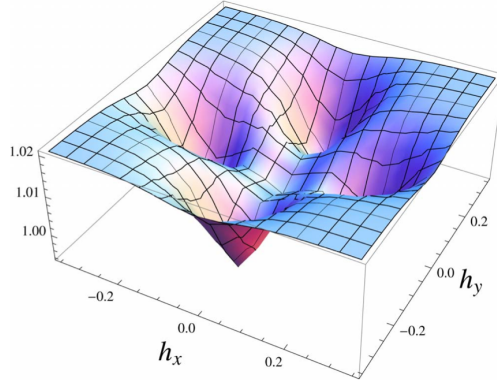


Figure 2.11: Dependence of the surface energy (in units of γ_f) on the local slopes h_x and h_y with one minimum for the (001) orientation and four minima corresponding to the (105) orientations, from [AQU 10a].

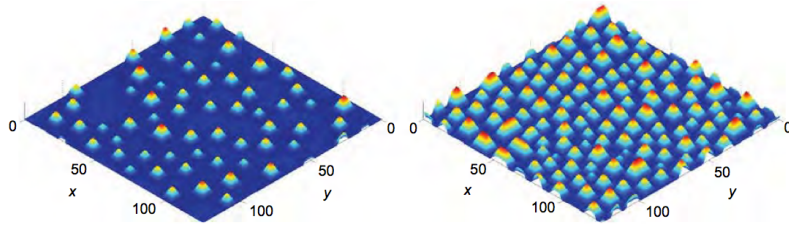


Figure 2.12: Simulation of the ATG instability with a SiGe dedicated anisotropy. If only square base pyramids are visible for low film thickness (left), a coexistence of both square base and rectangular base pyramids occurs for larger deposited height (right), from [AQU 10a].

variation of $\gamma(\mathbf{n})$ based on experimental observations. As regards SiGe films deposited on a nominal (001) surface, one expects $\gamma(\mathbf{n})$ to describe minima corresponding to a smooth (001) and stiff (105) orientations (see Sec. 2.4.2), see Fig. 2.11. If one considers such an anisotropy in the non-linear evolution equation [AQU 10a], one finds that the initial mainly isotropic islands (called ‘prepyramids’) grow with an increasing aspect ratio until their slopes reach the (105) angle, see Fig. 2.12. Once this is realised, the (105) facet quickly spreads over the island surface and transforms the island in square- or rectangular-base pyramids. After this stage, island coarsening stops after some time during annealing or growth and the system is characterized by pyramids when the film thickness is not too large.

The interruption of the coarsening in these systems is coherent with experimental findings showing that the pyramidal islands resulting from the ATG instability interrupt their coarsening after some time [AQU 13]. After 18 h annealing, some pyramids arise in groups, see Fig. 2.13b. On larger time, the wetting layer is fully covered and coarsening produces large pyramids, see Fig. 2.13c. Later on, the island density does not significantly evolve and the system reaches a nearly stationary state. Both square and

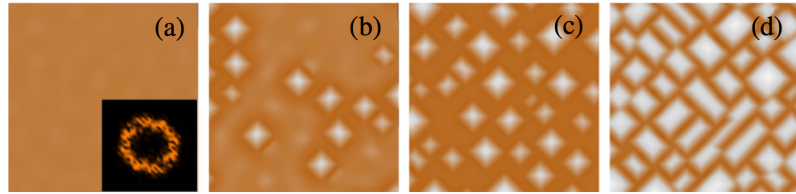


Figure 2.13: Numerical resolution for a strained anisotropic film for (a) a 5 nm film and annealing time $t=0$ (Fourier transform in inset), (b) 18 h (240 t_0), (c) 54 h (720 t_0), and (d) an 8 nm film and $t=18$ h (240 t_0). The scan area is $1.2 \times 1.2 \mu\text{m}^2$ and the vertical scale is 31 nm, from [AQU 13].

rectangular pyramids are visible, the latter being more numerous for larger thicknesses, see Fig. 2.13d. This dynamical evolution is qualitatively similar to the results of the continuum modelization and a quantitative comparison can even be done using appropriate wetting parameters [AQU 13]. This interrupted evolution may be ascribed to the vanishing of the coarsening driving force when islands display similar shapes with low chemical potential differences [AQU 13].

2.6 Growth on a pattern

As explained Chap. 1, the growth of islands on a pattern leads experimentally to contradicting results. We review here some of the theoretical results which apply to these systems when no alloying effects are at work. It was shown, on the basic of a continuum modelization with a diffusion of an alloy, that the composition dependance of the surface diffusivity may lead to an anomalous smoothing of the pattern prior to island growth. This analysis applies e.g. at high temperature ($T \sim 720$ °C) where alloying is at work. However, we mainly focus in the following on systems where it is not the case, which are dictated by the surface and elastic energies.

2.6.1 Equilibrium

One may first compute the elastic energy of different geometries and look for its minimization. Liu and co-workers [WAN 08] showed that for a sinusoidal substrate profile and for a sinusoidal film surface, the geometry which minimizes the total energy corresponds to a film with the same wavelength as the underlying substrate but shifted by half a wavelength (anti-phase configuration), see Fig. 2.14. In another geometry where an island sits on top of a pit, the calculation of Tersoff [KAT 08] also showed that the geometry which minimizes the total energy corresponds to the case where the island is centered on the trench, see Fig. 2.15.

An atomistic analysis based on Monte Carlo simulations of an island lying on a step patterned substrate was performed in [PAS 08]. The simulated structures concerned a Ge island on top of a Ge wetting layer deposited on a Si substrate in the (001) orientation with

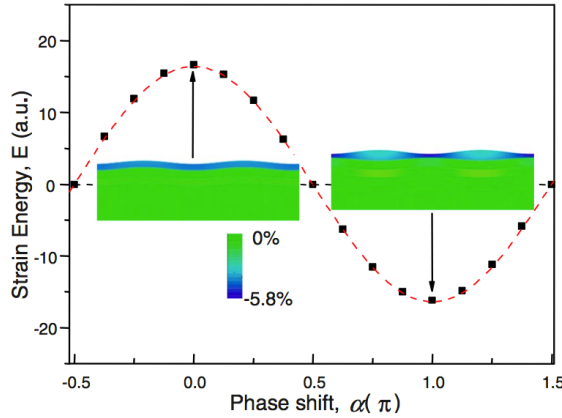


Figure 2.14: The strain energy as a function of phase shift α between a sinusoidal film on a sinusoidal pattern. The energy on a flat substrate is set as the reference energy. The (red) dashed line is a fit using a cos function to the calculated data (squares). The insets show the stress distributions at the maximum-energy ($\alpha=0$) and maximum-energy ($\alpha=\pi$) configurations respectively, from [WAN 08].

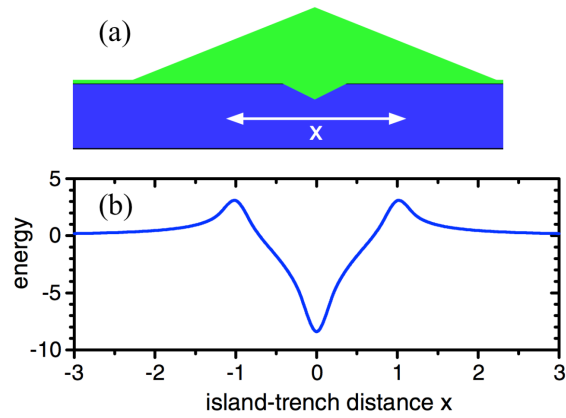


Figure 2.15: (a) Schematic illustration of the geometry used to calculate relaxation energy. The trench is 1/5 as wide as the island here. The plot is independent of the island size or slope, from [KAT 08].

2. Formation mechanisms

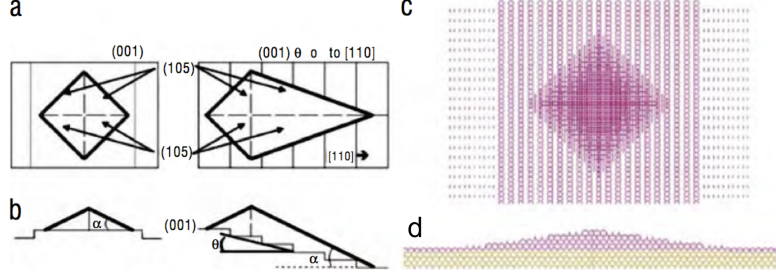


Figure 2.16: (a) Top view and (b) side view of a pyramidal island with (105) facets located on the terrace between two holes (left) and on the side of the hole (right). (c) Top view and (d) side view of the simulated structure consisting of a Ge island on top of the 2×1 reconstructed Ge wetting layer (between pits) itself on top of the Si substrate, from [PAS 08].

a pit pattern representing holes, see Fig. 2.16. The result of this microscopic analysis is that islands minimise their total energy on terraces separating pits rather than on stepped pit walls.

2.6.2 Nucleation barriers

In addition to the previous energetic considerations, it is well-known that the surface morphology produced in crystal growth also results from the growth kinetics. It may favor nucleation inside a hole (as compared to a flat terrace) because of a higher number of steps which act as favorable nucleation centers. In order to estimate energy barriers for nucleation, the strain relaxation allowed by the nucleation of islands on a sawtooth pattern was developed in [HU 08]. The strain energy difference between the island and the uniformly strained film was computed using the half-plane Green function within the small-slope approximation,

$$\mathcal{E}^{el} = -\frac{\sigma^2}{2} \int \int dx dx' G(x-x') \partial_i h(x) \partial_j h(x'), \quad (2.29)$$

where σ is the bulk stress acting on the island, x , the position along the surface, and G , the Green function relating the displacement at x' induced by a force at x . When considering only the force monopoles produced by the film thickness variation and neglecting the force dipoles induced by the surface waviness, one finds $E^{el} = -\epsilon_0 S (\tan \theta - \tan \phi)$. Accounting for the surface energy created by the island, the total island formation energy is then

$$\Delta E = -\epsilon_0 S (\tan \theta - \tan \phi) + 2\Gamma S^{1/2} (\tan \theta - \tan \phi)^{1/2}, \quad (2.30)$$

where $\epsilon_0 = 2 \ln 2 \sigma^2 (1 - v^2) / \pi Y$ is the scaled elastic energy density, $\Gamma = (\gamma_f \sec \theta - \gamma_w \sec \phi) / (\tan \theta - \tan \phi)$ with γ_f and γ_w , the surface energy of island facets and wetting layer respectively. The competition between the strain relaxation which is positive and the surface creation energy which is negative defines a critical island size

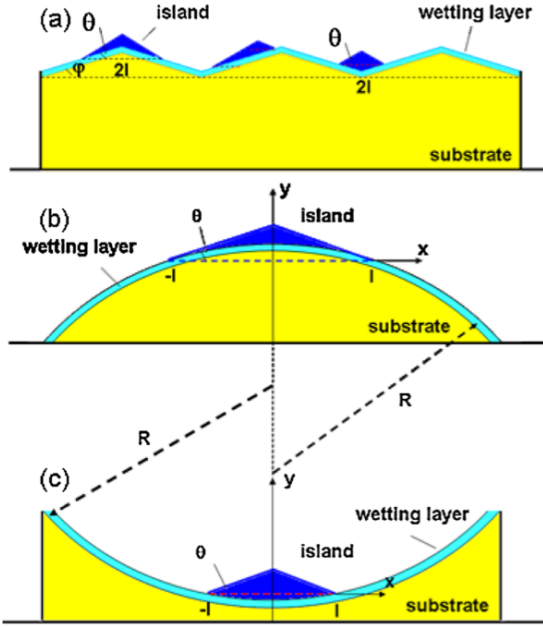


Figure 2.17: Schematic illustration of island nucleation: (a) on a sawtooth pattern; (b) on the apex of a concave surface; (c) in the valley of a convex surface, from [HU 08].

$S_c = (\Gamma/\varepsilon_0)^2 / (\tan \theta - \tan \phi)$ and an energy barrier $E_c = \Gamma^2 / \varepsilon_0$. In the case of an isotropic surface energy, for a given slope of the patterns and island facets, the results of this analysis [HU 08] show that both S_c and E_c are smaller in the valley than on the apex proving that in this situation, valleys are kinetically favored nucleation sites. It may be explained by a more effective strain relaxation for islands in the valley rather than on the apex as the thickness variation is smaller on the apex compared to the thickness variation in the valley, see Fig. 2.17.

2.6.3 Dynamical analysis

The dynamical analysis of the instability growing on a patterned substrate will be performed in the following chapters. However, one can already evaluate the influence of the different contributions to the chemical potential which dictates the surface diffusion and thence the dynamical evolution (2.3). The contribution to the surface chemical potential (2.24), proportional to the curvature favors diffusion towards the convex parts of the surface (film valleys). On the contrary, the elastic energy of the film alone (without any pattern) favors mass diffusion towards concave areas (film peaks), as a result of a more efficient relaxation. Another contribution to the elastic energy arises from the elastic energy linked to the pattern (buried elastic dipoles at the film/substrate interface). As seen in the following, this part favors surface diffusion towards the positions on top of the pattern valleys. As a consequence, the island positioning results from the competition of these three terms and requires a full analysis of the dynamical evolution.

2. Formation mechanisms

Chapter 3

Linear analysis of the morphological instability on a pattern

Contents

3.1	Elastic energy density	42
3.1.1	Geometry	42
3.1.2	Mechanical equilibrium	42
3.1.3	Small-slope approximation	44
3.1.4	Surface elastic energy density	45
3.2	Equilibrium state	46
3.3	Surface energy and wetting interactions	47
3.4	Evolution equation	48
3.5	Evolution	49
3.5.1	Initial condition	49
3.5.2	Analytical results	49
3.5.3	Kinetic phase diagram	54
3.6	Articles	56

In this chapter, we consider a dynamical continuum model describing the ATG instability on a patterned substrate. It describes the surface diffusion ruled by surface, wetting and elastic energies. In the small-slope approximation, we solve the mechanical equilibrium equations and study the film dynamics at linear order in the surface corrugation.

3.1 Elastic energy density

3.1.1 Geometry

We consider a film coherently deposited on a substrate. The semi-infinite substrate is supposed to be patterned and displays a wavy surface, see Fig. 3.1. In the continuum framework, the film surface and the film/substrate interface are defined respectively by $z=h(\mathbf{r})$ and $z=\eta(\mathbf{r})$, where $\mathbf{r} = \{x, y\}$ is the two-dimensional vector perpendicular to the growth direction z . The substrate shape is supposed to morphologically fixed.

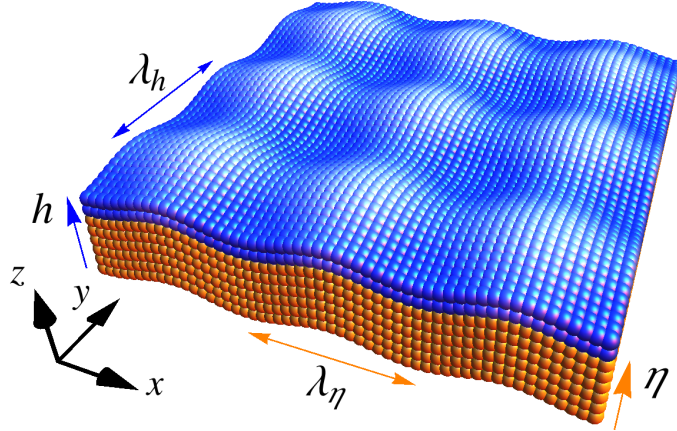


Figure 3.1: A film coherently with the free surface $z=h(x,y)$ deposited on a egg-carton substrate with the shape $z=\eta(x,y)$.

3.1.2 Mechanical equilibrium

We suppose that the system undergoes a quasi-static evolution where mechanical equilibrium is always achieved (Sec. 2.2.1). The Navier-Cauchy equations which describe the vanishing of the forces at equilibrium are given in isotropic systems in Eq. 2.9 and the appropriate boundary conditions in Sec. 2.2.1. A common way to solve these Partial Differential Equations, is to search for the displacements in Fourier space $\mathbf{u}(\mathbf{r},z) = e^{-i\mathbf{k}\cdot\mathbf{r}} \hat{\mathbf{u}}(\mathbf{k},z)$, where $\mathbf{k} = (k_x, k_y)$ is the two-dimensional wave-vector. In Fourier space, the Navier-Cauchy equations reduce simply to a set of second order differential equations

$$-\begin{pmatrix} k_x^2 \hat{u}_x + k_x k_y \hat{u}_y + i k_x \hat{u}'_z \\ k_x k_y \hat{u}_x + k_y^2 \hat{u}_y + i k_y \hat{u}'_z \\ i k_x \hat{u}'_x + i k_y \hat{u}'_y - \hat{u}''_z \end{pmatrix} + (1 - 2v) \left(-\mathbf{k}^2 + \frac{\partial^2}{\partial z^2} \right) \begin{pmatrix} \hat{u}_x \\ \hat{u}_y \\ \hat{u}_z \end{pmatrix} = \begin{pmatrix} 0 \\ 0 \\ 0 \end{pmatrix}. \quad (3.1)$$

where primes ' are derivatives with respect to z . This set of 3 second order differential equations is analytically solvable and involves in general 6 unknowns. One can get rid of the peculiar $\mathbf{k}=0$ mode by writing

$$h(\mathbf{r}) = \bar{H} + \delta h(\mathbf{r}). \quad (3.2)$$

One can then search for a solution for \mathbf{u} as

$$\mathbf{u} = \bar{\mathbf{u}} + \delta \mathbf{u}, \quad (3.3)$$

where $\bar{\mathbf{u}}$ is the solution in the flat geometry given in Eq. 2.14 and $\delta \mathbf{u}$ involves only non-zero \mathbf{k} . The general solution for $\delta \mathbf{u}$ is then in the film ($\alpha=f$) and substrate ($\alpha=s$)

$$\begin{aligned} \delta \hat{\mathbf{u}}^\alpha &= \frac{e^{-|\mathbf{k}|z}}{8|\mathbf{k}|^3(1-v)(1-2v)} \\ &\times \left(\begin{array}{l} (1-2v)[k_x^2(|\mathbf{k}|z+1)-4(1-v)\mathbf{k}^2]C_1^\alpha + (1-2v)(|\mathbf{k}|z+1)k_xk_yC_2^\alpha \\ -2i(1-v)\mathbf{k}^2k_xzC_3^\alpha + 2(1-v)[2(1-2v)|\mathbf{k}|-k_x^2z]\mathbf{k}^2C_4^\alpha \\ -2(1-v)\mathbf{k}^2k_xk_yzC_5^\alpha + i(1-2v)(|\mathbf{k}|z+1)\mathbf{k}^2k_xC_6^\alpha \end{array} \right) \\ &\times \left(\begin{array}{l} (1-2v)(|\mathbf{k}|z+1)k_xk_yC_1^\alpha + (1-2v)[k_y^2(|\mathbf{k}|z+1)-4(1-v)\mathbf{k}^2]C_2^\alpha \\ -2i(1-v)\mathbf{k}^2k_yzC_3^\alpha - 2(1-v)\mathbf{k}^2k_xk_yzC_4^\alpha \\ +2(1-v)[2(1-2v)|\mathbf{k}|-k_y^2z]\mathbf{k}^2C_5^\alpha + i(1-2v)(|\mathbf{k}|z+1)\mathbf{k}^2k_yC_6^\alpha \end{array} \right. \\ &\quad \left. \begin{array}{l} -i(1-2v)(k_xC_1^\alpha + k_yC_2^\alpha)\mathbf{k}^2z - 2(1-v)(3-4v+|\mathbf{k}|z)\mathbf{k}^2C_3^\alpha \\ +2i(1-v)(|\mathbf{k}|z+1)(k_xC_4^\alpha + k_yC_5^\alpha)\mathbf{k}^2 + (1-2v)[4(1-v)+|\mathbf{k}|z]|\mathbf{k}|^3 \end{array} \right) \\ &+ \frac{e^{|\mathbf{k}|z}}{8|\mathbf{k}|^3(1-v)(1-2v)} \\ &\times \left(\begin{array}{l} (1-2v)[k_x^2(|\mathbf{k}|z-1)+4(1-v)\mathbf{k}^2]C_1^\alpha + (1-2v)(|\mathbf{k}|z-1)k_xk_yC_2^\alpha \\ +2i(1-v)\mathbf{k}^2k_xzC_3^\alpha + 2(1-v)[2(1-2v)|\mathbf{k}|+k_x^2z]\mathbf{k}^2C_4^\alpha \\ +2(1-v)\mathbf{k}^2k_xk_yzC_5^\alpha + i(1-2v)(|\mathbf{k}|z-1)\mathbf{k}^2k_xC_6^\alpha \end{array} \right) \\ &\times \left(\begin{array}{l} (1-2v)(|\mathbf{k}|z-1)k_xk_yC_1^\alpha + (1-2v)[k_y^2(|\mathbf{k}|z-1)+4(1-v)\mathbf{k}^2]C_2^\alpha \\ +2i(1-v)\mathbf{k}^2k_yzC_3^\alpha + 2(1-v)\mathbf{k}^2k_xk_yzC_4^\alpha \\ +2(1-v)[2(1-2v)|\mathbf{k}|+k_y^2z]\mathbf{k}^2C_5^\alpha + i(1-2v)(|\mathbf{k}|z-1)\mathbf{k}^2k_yC_6^\alpha \end{array} \right. \\ &\quad \left. \begin{array}{l} i(1-2v)(k_xC_1^\alpha + k_yC_2^\alpha)\mathbf{k}^2z + 2(1-v)(3-4v-|\mathbf{k}|z)\mathbf{k}^2C_3^\alpha \\ +2i(1-v)(|\mathbf{k}|z-1)(k_xC_4^\alpha + k_yC_5^\alpha)\mathbf{k}^2 + (1-2v)[4(1-v)-|\mathbf{k}|z]|\mathbf{k}|^3 \end{array} \right), \end{aligned} \quad (3.4)$$

where $C_\beta^\alpha(\mathbf{k})$ with $\beta = 1, \dots, 6$ are unknown constants.

The general solution (3.4) has to be specified with the boundary conditions of the system, which can not be done for any shape in the general case. However, the lower boundary condition setting the reference of displacements deep in the substrate can already be

solved. Deep in the substrate when $z \rightarrow -\infty$, the displacement $\mathbf{u}^s \rightarrow \mathbf{0}$ corresponding to the Si free of stress. Thus, the term $e^{|\mathbf{k}|z}$ in Eq. 3.4 equals to zero, and we get

$$\begin{pmatrix} C_1^s \\ C_2^s \\ C_3^s \end{pmatrix} = \frac{1}{(3-4\nu)|\mathbf{k}|} \begin{pmatrix} [(3-4\nu)\mathbf{k}^2 + k_x^2]C_4^s + k_xk_yC_5^s + i|\mathbf{k}|k_xC_6^s \\ k_xk_yC_4^s + [(3-4\nu)\mathbf{k}^2 + k_y^2]C_5^s + i|\mathbf{k}|k_yC_6^s \\ i|\mathbf{k}|k_xC_4^s + i|\mathbf{k}|k_yC_5^s + 2(1-2\nu)\mathbf{k}^2C_6^s \end{pmatrix}. \quad (3.5)$$

3.1.3 Small-slope approximation

In order to solve analytically the boundary conditions describing the elastic equilibrium, we use the small-slope approximation described in Sec. 2.2.3 both for the film and the pattern. The surface and interface slopes are supposed smaller than unity so that one can decompose $h(\mathbf{r})$ as $h(\mathbf{r}) = \bar{H} + \varepsilon h_1(\mathbf{r})$, and $\eta(\mathbf{r})$ as $\eta(\mathbf{r}) = \varepsilon \eta_1(\mathbf{r})$. We then search for a solution where $\delta\mathbf{u}$ can be expanded in series of ε , $C_\beta^\alpha = \sum_{n=1}^{\infty} \varepsilon^n C_\beta^{\alpha(n)}$ with $n = 1, 2$ corresponding to the first and second orders. In this Chapter, we focus on the first order solution, while the second one is given in next Chapter.

The hypothesis of a coherent film/substrate interface enforces the continuity at the interface of displacements and forces

$$\mathbf{u}|_{z=\eta(\mathbf{r})^-} = \mathbf{u}|_{z=\eta(\mathbf{r})^+}, \quad (3.6)$$

$$\boldsymbol{\sigma}[\mathbf{u}] \cdot \mathbf{n}_\eta(\mathbf{r})|_{z=\eta(\mathbf{r})^-} = \boldsymbol{\sigma}[\mathbf{u}] \cdot \mathbf{n}_\eta(\mathbf{r})|_{z=\eta(\mathbf{r})^+}, \quad (3.7)$$

where \mathbf{n}_η is the unit vector perpendicular to the film/substrate interface

$$\mathbf{n}_\eta = \frac{1}{\sqrt{1 + |\nabla \eta|^2}} \begin{pmatrix} -\eta_x \\ -\eta_y \\ 1 \end{pmatrix}. \quad (3.8)$$

The film surface is supposed to be free of stress so that the boundary condition at the film surface is

$$\boldsymbol{\sigma}[\mathbf{u}] \cdot \mathbf{n}_h|_{z=h(\mathbf{r})} = \mathbf{0}, \quad (3.9)$$

where \mathbf{n}_h is the unit vector perpendicular to the film free surface

$$\mathbf{n}_h = \frac{1}{\sqrt{1 + |\nabla h|^2}} \begin{pmatrix} -h_x \\ -h_y \\ 1 \end{pmatrix}. \quad (3.10)$$

The boundary conditions (BC) (3.6), (3.7), (3.9) enforces 9 conditions for the 9 remaining unknowns (3 unknowns for the substrate C_β^s and 6 other unknowns for the film

C_β^f). Using the (3.6), we get

$$\begin{pmatrix} C_4^{s(1)} \\ C_5^{s(1)} \\ C_6^{s(1)} \end{pmatrix} = \begin{pmatrix} C_4^{f(1)} \\ C_5^{f(1)} \\ C_6^{f(1)} \end{pmatrix} + m \frac{1+\nu}{1-\nu} \hat{\eta}(\mathbf{k}) \begin{pmatrix} 0 \\ 0 \\ 1 \end{pmatrix}. \quad (3.11)$$

Using (3.7), we get

$$\begin{pmatrix} C_1^{f(1)} \\ C_2^{f(1)} \\ C_3^{f(1)} \end{pmatrix} = \frac{1}{(3-4\nu)|\mathbf{k}|} \begin{pmatrix} [(3-4\nu)\mathbf{k}^2 + k_x^2]C_4^{f(1)} + k_x k_y C_5^{f(1)} + i|\mathbf{k}|k_x C_6^{f(1)} \\ k_x k_y C_4^{f(1)} + [(3-4\nu)\mathbf{k}^2 + k_y^2]C_5^{f(1)} + i|\mathbf{k}|k_y C_6^{f(1)} \\ i|\mathbf{k}|k_x C_4^{f(1)} + i|\mathbf{k}|k_y C_5^{f(1)} + 2(1-2\nu)\mathbf{k}^2 C_6^{f(1)} \end{pmatrix} + 2m \frac{1+\nu}{3-4\nu} \hat{\eta}(\mathbf{k}) \begin{pmatrix} 2ik_x \\ 2ik_y \\ \frac{1-2\nu}{1-\nu} |\mathbf{k}| \end{pmatrix}. \quad (3.12)$$

Finally, using the BC. 3.9, one finds

$$\begin{pmatrix} C_4^{f(1)} \\ C_5^{f(1)} \\ C_6^{f(1)} \end{pmatrix} = m \frac{1+\nu}{1-\nu} \frac{e^{-|\mathbf{k}|\bar{H}}}{|\mathbf{k}|} \hat{h}(\mathbf{k}) \begin{pmatrix} ik_x[2(1-\nu) - |\mathbf{k}|\bar{H}] \\ ik_y[2(1-\nu) - |\mathbf{k}|\bar{H}] \\ |\mathbf{k}|(1-2\nu + |\mathbf{k}|\bar{H}) \end{pmatrix} + m \frac{1+\nu}{1-\nu} \frac{e^{-2|\mathbf{k}|\bar{H}}}{2|\mathbf{k}|} \hat{\eta}(\mathbf{k}) \begin{pmatrix} ik_x(4\nu - 3 - e^{2|\mathbf{k}|\bar{H}} + 2|\mathbf{k}|\bar{H}) \\ ik_y(4\nu - 3 - e^{2|\mathbf{k}|\bar{H}} + 2|\mathbf{k}|\bar{H}) \\ |\mathbf{k}|(4\nu - 3 - e^{2|\mathbf{k}|\bar{H}} - 2|\mathbf{k}|\bar{H}) \end{pmatrix}, \quad (3.13)$$

where \bar{H} is the mean film thickness. Eventually, the solution at *linear order* in ε for the displacement in the film is

$$\begin{aligned} \delta \mathbf{u}^{f(1)}(\mathbf{k}) &= m \frac{1+\nu}{1-\nu} \frac{e^{|\mathbf{k}|(z-\bar{H})}}{|\mathbf{k}|} \hat{h}(\mathbf{k}) \begin{pmatrix} [2(1-\nu) + |\mathbf{k}|(z-\bar{H})]ik_x \\ [2(1-\nu) + |\mathbf{k}|(z-\bar{H})]ik_y \\ [1-2\nu - |\mathbf{k}|(z-\bar{H})]|\mathbf{k}| \end{pmatrix} \\ &- m \frac{1+\nu}{1-\nu} \frac{1}{2|\mathbf{k}|} \hat{\eta}(\mathbf{k}) \begin{pmatrix} \{e^{-|\mathbf{k}|z} + e^{|\mathbf{k}|(z-2\bar{H})}\}[(3-4\nu) + 2|\mathbf{k}|(z-\bar{H})]ik_x \\ \{e^{-|\mathbf{k}|z} + e^{|\mathbf{k}|(z-2\bar{H})}\}[(3-4\nu) + 2|\mathbf{k}|(z-\bar{H})]ik_y \\ \{e^{-|\mathbf{k}|z} + e^{|\mathbf{k}|(z-2\bar{H})}\}[(3-4\nu) - 2|\mathbf{k}|(z-\bar{H})]|\mathbf{k}| \end{pmatrix}, \end{aligned} \quad (3.14)$$

where, beside the trivial height renormalisation described by $z - \bar{H}$, an explicit dependence on \bar{H} is associated with the buried elastic dipoles of the film/substrate interface which are naturally height-dependant.

3.1.4 Surface elastic energy density

According to Eq. 2.6, the surface chemical potential which drives surface diffusion is $\mu^{el} = \Omega \mathcal{E}^{el}[\mathbf{r}, z=h(\mathbf{r})] = \Omega \frac{1}{2} \boldsymbol{\sigma}_{ij} e_{ij}$. For the flat case (Sec. 2.2.2), it is given by $\bar{\mathcal{E}}^{el} =$

$Ym^2/(1-\nu)$. With the solution at first order $\mathbf{u}^f = \bar{\mathbf{u}}^f + \delta\mathbf{u}^{f(1)}$ (2.14 and 3.14), it reads $\mu^{el} = \bar{\mathcal{E}}^{el} + \mu^{el(1)}$ where

$$\frac{\mu^{el(1)}(\mathbf{r})}{2\Omega(1+\nu)\bar{\mathcal{E}}^{el}} = \int d\mathbf{k} e^{-i\mathbf{k}\cdot\mathbf{r}} |\mathbf{k}| \left[e^{-|\mathbf{k}|\bar{H}} \hat{\eta}(\mathbf{k}) - \hat{h}(\mathbf{k}) \right] \equiv \mathcal{H}_{ii}[\mathcal{B}[\eta]] - \mathcal{H}_{ii}[h], \quad (3.15)$$

in terms of the generalised Hilbert transform $\mathcal{H}_{ij}(h) = \mathcal{F}^{-1}[k_i k_j / |\mathbf{k}| \hat{h}(\mathbf{k})]$, and a new operator \mathcal{B} defined as

$$\mathcal{B}[h] = \mathcal{F}^{-1}[e^{-|\mathbf{k}|\bar{H}} \mathcal{F}[h]], \quad (3.16)$$

where the exponential term $e^{-|\mathbf{k}|\bar{H}}$ is a sign of the damping of elastic interactions in the vertical direction. It is noteworthy to mention that this damping occurs on the typical length scale k^{-1} associated with the variations in the horizontal direction, which can be rather large. Given this solution, we can compute the total elastic energy by functional integration (recall that $\mu^{el} = \Omega \frac{\delta \mathcal{E}^{el}}{\delta h}$), with the results

$$E_{tot}^{el} = \mathcal{E}^0 \int d\mathbf{r} \{ h(\mathbf{r}) - (1+\nu)h(\mathbf{r}) [\mathcal{H}_{ii}[h(\mathbf{r})] - 2\mathcal{H}_{ii}[\eta(\mathbf{r})]] \}. \quad (3.17)$$

3.2 Equilibrium state

We search in this section the geometry which minimizes the total energy in the case of a pattern with a simple sinusoidal shape. The energy involves both the elastic and surface energies, with the latter including the wetting effects. The elastic energy is given in (3.17). On the other hand, the surface energy in an isotropic system is merely

$$E^s = \int d\mathbf{r} \gamma[h(\mathbf{r}), \eta(\mathbf{r})] \sqrt{1 + |\nabla h|^2}, \quad (3.18)$$

where the film/substrate wetting interactions are embedded in the $h(\mathbf{r})$ and $\eta(\mathbf{r})$ dependence of the surface energy γ .

We consider a pattern with an harmonic shape $\eta(\mathbf{r}) = A_\eta e^{i\mathbf{k}\cdot\mathbf{r}}$ with the wave-vector \mathbf{k} and amplitude A_η . For a film with the same wave-vector \mathbf{k} as the pattern but with a phase shift φ and an amplitude A_h , $h(\mathbf{r}) = \bar{H} + A_h e^{i\mathbf{k}\cdot\mathbf{r} + \varphi}$, see Fig. 3.2, we find

$$E^{tot} \propto B(\bar{H}, \mathbf{k}) \cos \varphi, \quad (3.19)$$

where $B(\bar{H}, \mathbf{k}) = |\mathbf{k}| e^{-|\mathbf{k}|\bar{H}} - e^{-\bar{H}/\delta_w} c_w / \delta_w^2$. Thus, the sign of B gives the configuration of minimum energy. The root of $B(\bar{H}, \mathbf{k}) = 0$ is easily found a critical thickness H^{eq} for the phase exchange to be energetically favorable

$$H^{eq} = \frac{\delta_w \ln(|\mathbf{k}| \delta_w^2 / c_w)}{|\mathbf{k}| \delta_w - 1}. \quad (3.20)$$

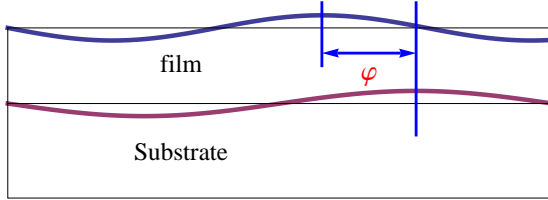


Figure 3.2: Schematic representation of a film and a substrate having the same wave-vector but a phase shift φ .

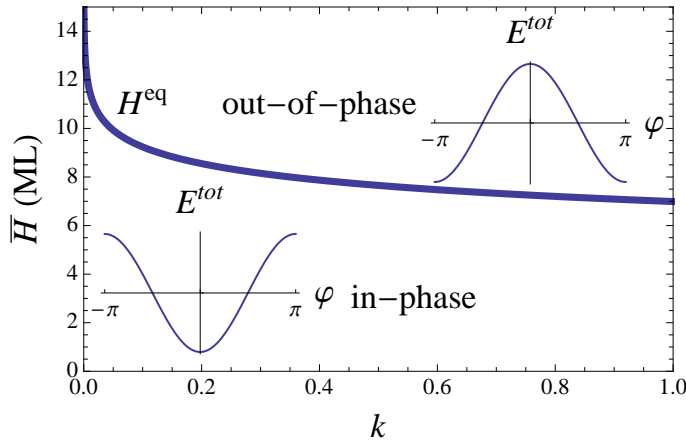


Figure 3.3: State of lowest energy for a film of thickness \bar{H} with the same wave-vector k as the substrate but with a phase-shift φ . The thick solid line corresponds to $H^{\bar{e}q}$. The equilibrium state corresponds to a film in-phase with the substrate below this line, and to an out-of-phase configuration above. Insets display the total energy as a function of the phase φ which is indeed minimum at $\varphi=0$ (resp. π) below (reps. above) the $H^{\bar{e}q}$ line.

It is plotted in Fig. 3.3. The amplitude B is always negative when \bar{H} is smaller than $H^{\bar{e}q}$ and is associated with a minimum at $\varphi=0$ where the film is in-phase with the substrate. The elastic energy is always minimum for an out-of-phase configuration ($\varphi=\pi$) and the $\varphi=0$ state is therefore enforced by wetting interactions which are indeed minimum in such a geometry. In contrast, when \bar{H} is larger than this root, B is positive and the minimum energy is found for $\varphi=\pm\pi$ which corresponds to an out-of-phase configuration which minimises the elastic energy. These results apply only to the equilibrium state and we now turn to the study of the evolution of the surface.

3.3 Surface energy and wetting interactions

For a flat substrate, the wetting potential describes the microscopic dependance of the broken bonds on the local film height (Sec. 2.4). A priori one could expect that the wetting potential of a film on a patterned substrate could also depend on the shape of the pattern.

In order to simplify the calculation, we neglect such a dependence and consider that the surface energy only depends on the local film height $h(\mathbf{r}) - \eta(\mathbf{r})$ which is all the more justified as we work within the small-slope approximation. Consequently, we consider in the following the generalization of Eq. 2.23

$$\gamma[h(\mathbf{r}), \eta(\mathbf{r})] = \gamma_f [1 + c_w e^{-[h(\mathbf{r}) - \eta(\mathbf{r})]/\delta_w}]. \quad (3.21)$$

3.4 Evolution equation

With the elastic chemical potential (3.15), the evolution equation (2.3) describing surface diffusion in presence of elastic, surface and wetting energy gradients is given at *linear order* in h and η by

$$\frac{\partial h}{\partial t} = \Delta \left\{ -\Delta h + a(\bar{H})(h - \eta) - \mathcal{H}_{ii}[h] + \mathcal{H}_{ii}[\mathcal{B}[\eta]] \right\} + F, \quad (3.22)$$

in units of l_0 (2.21) and t_0 (2.22), with the amplitude of the wetting interactions

$$a(\bar{H}) = \frac{\partial^2 \gamma}{\partial h^2}(\bar{H}). \quad (3.23)$$

The first and third terms in the r.h.s of (3.22) are common with the flat substrate case [AQU 10a]. The last term describes the influence of the buried elastic dipoles of the film/substrate interface while the second term arises from the wetting potential. In Fourier space, this equation may be written as

$$\frac{\partial \hat{h}(\mathbf{k})}{\partial t} = \sigma(\mathbf{k}; \bar{H}) \hat{h}(\mathbf{k}) + \left[a(\bar{H}) \mathbf{k}^2 - |\mathbf{k}|^3 e^{-|\mathbf{k}| \bar{H}} \right] \hat{\eta}(\mathbf{k}), \quad (3.24)$$

where

$$\sigma(\mathbf{k}; \bar{H}) = -a(\bar{H}) \mathbf{k}^2 + |\mathbf{k}|^3 - \mathbf{k}^4, \quad (3.25)$$

is the usual growth rate with wetting interaction.

We consider a film which grows as $\bar{H}(t) = \bar{H}_0 + Ft$ with \bar{H}_0 , the initial thickness and a constant deposition flux F . The evolution equation (3.24) is a first order linear equation which can be integrated straight forwardly, with the result [XU 13]

$$\begin{aligned} \hat{h}(\mathbf{k}, t) &= \hat{h}^0(\mathbf{k}) e^{\sigma_k^*(t)t} + \delta(\mathbf{k}) F t \\ &+ \hat{\eta}(\mathbf{k}) e^{\sigma_k^*(t)t} \int_0^t dt' \left[\mathbf{k}^2 \delta \gamma''[\bar{H}(t')] - |\mathbf{k}|^3 e^{-|\mathbf{k}| \bar{H}(t')} \right] e^{-\sigma_k^*(t')t}, \end{aligned} \quad (3.26)$$

where $\hat{h}^0(\mathbf{k})$ is the Fourier transform of the initial condition $h(\mathbf{r}, t = 0)$ and $\delta(\mathbf{k})$ is the Dirac delta function. We defined the time-average growth rate

$$\sigma_k^*(t) = \frac{1}{t} \int_0^t dt' \sigma(\mathbf{k}; \bar{H}(t')). \quad (3.27)$$

If one considers the exponentially decaying wetting potential (3.21), one has $\delta\gamma''[\bar{H}(t)] = \frac{c_w}{\delta_w^2} e^{-\bar{H}(t)/\delta_w}$.

If we consider annealing ($F=0$) of a film of thickness \bar{H} , the solution for h is simpler and one finds [XU 12]

$$\hat{h}(\mathbf{k}, t; \bar{H}) = \hat{h}^0(\mathbf{k}) e^{\sigma(\mathbf{k}; \bar{H})t} - C(\mathbf{k}, \bar{H}) \left[e^{\sigma(\mathbf{k}; \bar{H})t} - 1 \right] \hat{\eta}(\mathbf{k}), \quad (3.28)$$

with the coefficient

$$C(\mathbf{k}, \bar{H}) = \frac{|\mathbf{k}|^3 e^{-|\mathbf{k}|\bar{H}} - a(\bar{H})\mathbf{k}^2}{\sigma(\mathbf{k}; \bar{H})}. \quad (3.29)$$

3.5 Evolution

3.5.1 Initial condition

In the following, we consider a substrate with an egg-carton shape, see Fig. 3.1, with a wave-vector \mathbf{k}_η :

$$\eta(\mathbf{r}) = \frac{1}{2} A_\eta [\cos(\mathbf{k}_\eta^x \cdot \mathbf{r}) + \cos(\mathbf{k}_\eta^y \cdot \mathbf{r})], \quad (3.30)$$

with $\mathbf{k}_\eta^x = (k_\eta, 0)$ and $\mathbf{k}_\eta^y = (0, k_\eta)$. This basic shape allows to capture the main mechanisms at work and, as shown in the following, helps rationalizing results for other pattern geometries. We are mainly concerned by the annealing case where a film with thickness \bar{H} has grown by following the substrate shape initial wetting of the Stransky-Krastanov growth mode. Hence, we consider the initial condition

$$h(\mathbf{r}, t=0) = \bar{H} + \eta(\mathbf{r}) + \mathcal{R}, \quad (3.31)$$

where \mathcal{R} is a white noise with a few monolayers amplitude which describes the intrinsic noise after deposition together with the substrate roughness. The influence of the flux on the instability is rather small, see article [XU 13] in Sec. 3.6, and is thence discarded to simplify the analysis.

3.5.2 Analytical results

In the following, we focus on the annealing case, corresponding to the evolution equation (3.28). Given the initial condition (3.31), we get

$$\hat{h}(\mathbf{k}, t; \bar{H}) = \left[\bar{H} \delta(\mathbf{k}) + \hat{\mathcal{R}}(\mathbf{k}) \right] e^{\sigma(\mathbf{k}; \bar{H})t} + \hat{\eta}(\mathbf{k}) \left\{ [1 - C(\mathbf{k}; \bar{H})] e^{\sigma(\mathbf{k}; \bar{H})t} + C(\mathbf{k}; \bar{H}) \right\}, \quad (3.32)$$

with the coefficient $C(\mathbf{k}; \bar{H})$ given in (3.29). When $\bar{H} < H_c$ (2.26), the growth rate $\sigma(\mathbf{k}; \bar{H})t < 0$ so that the surface is stable with respect to a morphological evolution and follows quickly the substrate shape, in-phase. For $\bar{H} > H_c$, when time is small, $e^{\sigma t} \sim 1$ and the film surface still follows in-phase the substrate undulation. When time increases

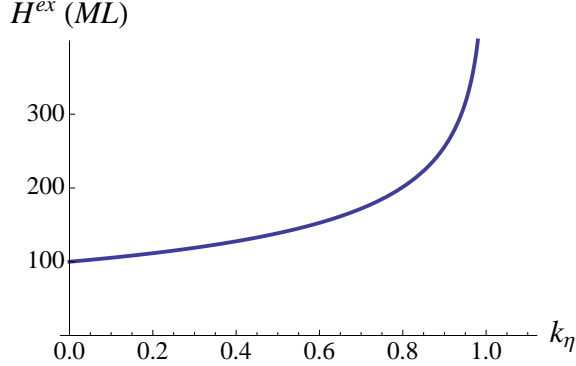


Figure 3.4: The thickness H^{ex} below which the surface skips after some time from in-phase to out-of-phase with respect to the pattern, as a function of the wave-vector of pattern k_η .

(but nevertheless in the regime where the film slopes remain small), the surface shape is ruled by the wave-vectors which have a positive growth rate $\sigma(\mathbf{k}; \bar{H})$, mainly for $k \leq 1$. Among these wave-vectors, two wave-vectors have a special role in the morphological evolution: the substrate mode k_η and the instability mode $k_{ATG} = 3/4$ which maximizes the growth rate σ for large \bar{H} (i.e. when wetting interactions are negligible, Sec. 2.3, Fig. 2.2). The pattern mode k_η has to be distinguished from the other modes as the initial condition (3.30) attributes a significant amplitude to this mode, contrarily to the roughness of the white noise distributed over all the modes.

We first study the evolution of the pattern mode k_η . Similarly to the flat-substrate case, for a small enough film thickness $\bar{H} < H_c$, the wetting interactions enforce the stability of the surface, as $\sigma(\mathbf{k}; \bar{H})$ is negative for every k . Consequently, the film remains in-phase with the substrate, which minimizes the total energy. For $\bar{H} > H_c$, the growth rate of k_η may be positive which is the case we study below. The evolution equation (3.32) gives $\hat{h}(\mathbf{k}_\eta, t) \approx \hat{\eta}(\mathbf{k}_\eta)$ for small t , while it behaves as $[1 - C(\mathbf{k}; \bar{H})]\hat{\eta}(\mathbf{k}_\eta)e^{\sigma(\mathbf{k}, \bar{H})t}$ for large t . Hence, when $C(\mathbf{k}; \bar{H})$ is larger than unity, $\hat{\eta}(\mathbf{k}_\eta)$ has to change its sign so that the surface skips from a configuration where it is in-phase with the substrate to a configuration where it is out-of-phase, when the film bumps coincide with the minima of the egg-carton substrate. In the limit of negligible wetting interactions (which is the case after a few deposited layers), the condition $C(\mathbf{k}; \bar{H}) > 1$ leads to the upper bound $h < H^{ex}$, where for $k_\eta < 1$

$$H^{ex}(k_\eta) = -\frac{\ln(1 - k_\eta)}{k_\eta}, \quad (3.33)$$

when the rate $\sigma(\mathbf{k}; \bar{H})$ is positive, see Fig. 3.4. Hence, the in- to out-of-phase exchange only occurs for a film thickness not too large as a result of the competition between the initial condition which sets an in-phase configuration and the elastic interactions which favor an out-of-phase geometry but which are exponentially damped in the vertical direction. When this condition is met, the time for the phase exchange may be estimated

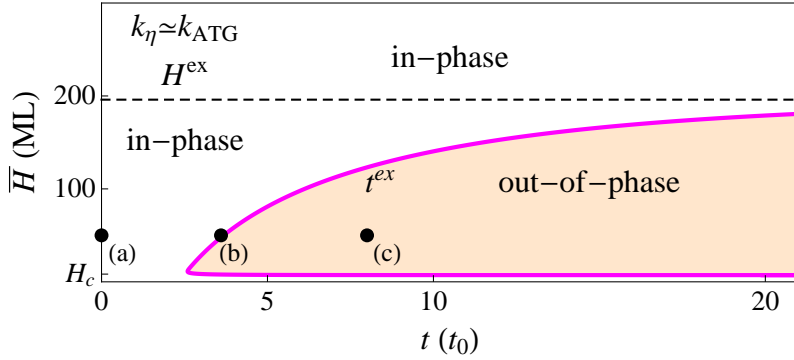


Figure 3.5: Kinetic phase diagram as a function of time and film thickness \bar{H} , for $k_{\eta} = k_{\text{ATG}}$ and parameters given in Sec. 3.5.3. The pink line t^{ex} refers to the time when the surface undulation vanishes before (resp. after) which the film surface is in- (resp. out-of) -phase. The horizontal black dashed line is the threshold H^{ex} below which the phase exchange can occur. The lower pink line refers to the thickness below which wetting interactions enforce an in-phase configuration.

as

$$t^{\text{ex}}(k_{\eta}, \bar{H}) = \ln \left[\frac{C(\mathbf{k}; \bar{H})}{C(\mathbf{k}; \bar{H}) - 1} \right] \frac{1}{\sigma(\mathbf{k}; \bar{H})}. \quad (3.34)$$

At t^{ex} , the amplitude of the k_{η} mode vanishes as this modulation must decrease first in order to change its sign and continue to grow exponentially. Hence, even when k_{η} corresponds to an unstable mode with a positive growth rate $\sigma(k_{\eta}; \bar{H}) > 0$, the roughness associated with this mode must vanish first in order to allow the out-of-phase exponential growth. The phase exchange time t^{ex} increases with \bar{H} as a result of the exponential damping in the vertical direction of the elastic interactions which are responsible for this exchange. Some examples of t^{ex} are given in Figs. 3.5 and 3.8. For $\bar{H} > H^{\text{ex}}$, the k_{η} mode remains in-phase as the effect of the initial condition is stronger than the effect of the pattern on the surface. These results are embedded in the kinetic phase diagram Fig. 3.5 showing the geometry of the film as a function of the film thickness \bar{H} and time, when $k_{\eta} = k_{\text{ATG}}$ drives the film evolution.

In the general case, the surface evolution is mainly ruled by the competition between the pattern mode and the instability mode k_{ATG} . Even if it is initially only induced by the white noise with a small amplitude, the k_{ATG} mode can overcome the k_{η} mode thanks to a faster growth rate, see Fig. 3.6. This cross-over may be relevant only if it occurs on a time-scale where the small-slope approximation is still satisfied and where the growing film surface did not cross the film/substrate interface. With the evolution equation (3.32), the spectrum of the film roughness is given by

$$\langle |\hat{h}(\mathbf{k}, t)|^2 \rangle = \langle |\hat{\mathcal{R}}(\mathbf{k})|^2 \rangle e^{2\sigma(\mathbf{k}; \bar{H})t} + \langle |\hat{\eta}(\mathbf{k})|^2 \rangle \left\{ [1 - C(\mathbf{k}; \bar{H})] e^{\sigma(\mathbf{k}; \bar{H})t} + C(\mathbf{k}; \bar{H}) \right\}^2, \quad (3.35)$$

as $\langle \hat{\mathcal{R}} \hat{\eta}^* \rangle = 0$ due to the zero-mean of the white noise $\hat{\mathcal{R}}$ and its independence with η . As the white noise is spread over all the modes, its amplitude in Fourier space includes

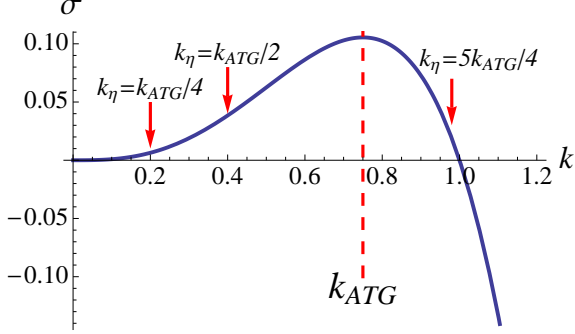


Figure 3.6: Variation of the growth rate σ with a maximum at k_{ATG} and values of k_η discussed in the text.

an extra small parameter compared to η . Indeed, for a typical noise equally distributed in the interval $[-A_R/2, A_R/2]$, where A_R is the amplitude of white noise, one can estimate the average over different realisations $\sqrt{|\hat{\mathcal{R}}|^2} = A_R \sqrt{N/12}$ for a system with N modes, which is negligible compared to $\hat{\eta}(k_\eta^\alpha) = A_\eta N/4$ (for $\alpha=x,y$) in the large N limit.

In order to describe the competition between the k_{ATG} and k_η modes in Eq. 3.35, we define

$$\begin{aligned} \Delta \langle |\hat{h}(\mathbf{k}, t)|^2 \rangle &= \langle |\hat{\mathcal{R}}(k_{ATG})|^2 \rangle e^{2\sigma(k_{ATG}; \bar{H})t} \\ &\quad - \langle |\hat{\eta}(k_\eta)|^2 \rangle \left\{ [1 - C(k_\eta; \bar{H})] e^{\sigma(k_\eta; \bar{H})t} + C(k_\eta; \bar{H}) \right\}^2, \end{aligned} \quad (3.36)$$

which is plotted in Fig. 3.7 for $k_\eta = k_{ATG}/2$. Initially, $\Delta \langle |\hat{h}(\mathbf{k}, t)|^2 \rangle$ is negative as the initial condition (the film wets the pattern) enforces a dominant k_η mode. In the case where the k_η mode undergoes a phase exchange, its amplitude first vanishes and then increases again, contrary to the k_{ATG} mode which keeps on growing. Consequently, when \bar{H} is not too large, $\Delta \langle |\hat{h}(\mathbf{k}, t)|^2 \rangle$ first vanishes and becomes slightly positive before becoming negative again, as a result mainly of the sole phase exchange of the k_η mode, while it eventually remains positive again for large time, as the k_{ATG} mode is dominant. When \bar{H} increases, $C(k, \bar{H})$ decreases and $\Delta \langle |\hat{h}(\mathbf{k}, t)|^2 \rangle$ only switch to positive values as the k_{ATG} mode is quickly dominant. In this case, there is only one solution for t for $\Delta |h|^2 = 0$ contrarily to the previous case characterized by three solutions. To characterize the time after which the dynamics is mainly ruled by the k_{ATG} mode, we define the time t^{max} after which $\Delta \langle |\hat{h}(\mathbf{k}, t)|^2 \rangle$ remains positive, see Fig. 3.7. This time is the typical time after which the instability may be considered as fully developed. When k_η is a growing mode not in the vicinity of k_{ATG} , t^{max} is not too large and may be observed in the linear regime. Hence, a new line is visible in the kinetic phase diagram in this case which delimits the initial configuration which is in-phase with the substrate, with a configuration where the instability of the flat case is fully developed with a lower spatial order, see Fig. 3.8. The time t^{ex} for the phase exchange is also indicated in Fig. 3.8 even though it is hidden by the instability development after t^{max} .

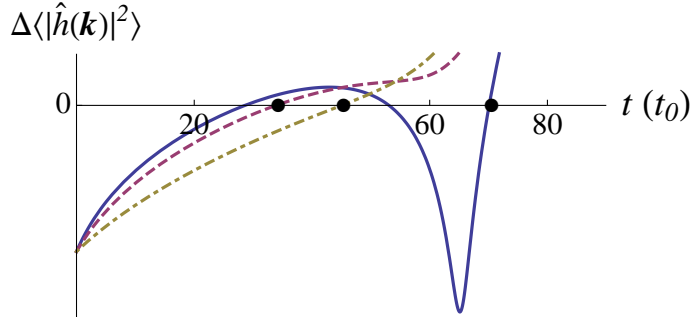


Figure 3.7: The competition between k_{ATG} and k_η modes described by the difference in their Fourier amplitudes $\Delta \langle |\hat{h}(\mathbf{k}, t)|^2 \rangle$ given in (3.36) for $\bar{H} = 66$ (solid line), 80 (the dashed line), 100 ML (the dot-dashed line) and $k_\eta = k_{\text{ATG}}/2$. The black points are related to t^{max} .

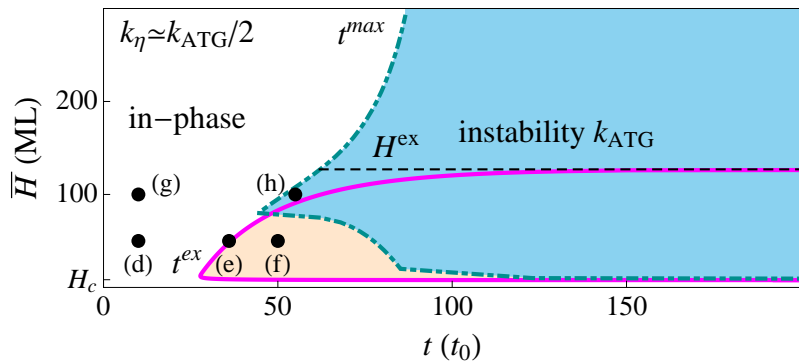


Figure 3.8: Kinetic phase diagram for $k_\eta = k_{\text{ATG}}/2$. The green dot-dashed line refers to the typical time t^{max} before which the film is mainly in-phase with the substrate at k_η and after which the instability is fully developed with the typical wave-vector k_{ATG} . The pink solid line characterizes the in- and out-of-phase exchange time t^{ex} of the sole k_η mode which occurs for $\bar{H} < H^{ex}$ (horizontal thin dashed line). The latter phase exchange is nevertheless often hidden by the growing mode k_{ATG} . Note that the cusp in the plot of t^{max} arises merely from the definition of t^{max} and from the shift from three to one solution of $\Delta \langle |\hat{h}(\mathbf{k}, t)|^2 \rangle = 0$, see Fig. 3.7.

3.5.3 Kinetic phase diagram

In order to picture the surface evolution during annealing in the linear regime we use a numerical plot of the solution (3.32) with the full spectrum and characterize kinetic phase diagrams which give the morphology as a function of time and thickness. We choose to depict a Si_{0.75}Ge_{0.25} film on a Si substrate. The Si structure is a diamond lattice with 8 atoms in a unit cell which is equivalent to a cubic lattice with $a^s = 0.27$ nm while $a^f = 1.01 a^s$ here. We consider the elastic parameters $v = 0.28$ and $E = 1.23 \times 10^{10}$ kg m⁻¹s⁻² and a surface energy $\gamma_f = 1.3$ J/m². One first finds $l_0 = 27$ nm [AQU 10a]. The diffusion coefficient is described by a typical Arrhenius law

$$D = \frac{D_s e^{-E_d/(k_B T)} a_f^4}{k_B T}, \quad (3.37)$$

with $E_d = 0.83$ eV, and $D_s = 8.45 \times 10^{-10}$ m²/s [SPE 05]. At the working temperature $T = 550$ °C, we find $t_0 = 450$ s. We extrapolate first-principles calculations of wetting interactions [LU 05] to this system by considering $c_w = 0.1$ and we set δ_w equal to one lattice parameter. The initial noise is described by a white noise with a roughness of 1 monolayer (ML). We consider a $128 l_0 \times 128 l_0$ box with periodic boundary conditions.

We first study the coincidence case $k_\eta = k_{\text{ATG}}$. The growth rate of the k_η mode is large enough so that it remains the dominant mode of the surface. The corresponding kinetic phase diagram is displayed in Fig. 3.5. For this system, the upper bound for the phase exchange to occur is $H^{ex} = 196$ ML. The geometry of a 50 ML thick film is plotted for three different times indicated in Fig. 3.5 (a) for an in-phase configuration, (b) at the phase exchange and (c) for an out-of-phase geometry in Fig. 3.9. The corresponding spectra $|\hat{h}(\mathbf{k})|^2$ are dominated by the k_η mode except at the phase exchange where it vanishes. Hence, after the phase exchange, the surface is nearly perfectly ordered with maxima located on top of the substrate minima, in the valleys of the substrate undulation. In contrast, for a larger film thickness, the elastic interactions with the substrate are sufficiently damped so that the initial in-phase geometry (a) is the only configuration and the surface maxima remain located on top of the substrate ones. Hence, the fact that k_η lies in the vicinity of k_{ATG} corresponds to the optimal ordering in the linear regime.

As described analytically before, when k_η is an unstable mode but not in the vicinity of k_{ATG} , the competition between these two modes rules the kinetic phase diagram, see Fig. 3.8. We consider this case when $k_\eta = k_{\text{ATG}}/2$, see Fig. 3.6. When \bar{H} is not too large ($\bar{H} = 50$ ML in Fig. 3.10), the film still undergoes a phase shift (d, e, f). However, when \bar{H} is large enough ($\bar{H} = 100$ ML in Fig. 3.11), the growth of the k_{ATG} mode occurs fast enough so that the phase exchange is hidden (g, h). In this case the film first grows in-phase with the substrate but the instability with k_{ATG} occurs after t^{max} and lowers the spatial order on the surface, see Fig. 3.10e. The geometry of the surface is displayed in Figs. 3.10d and 3.11g at early time when the film is mainly in-phase with the substrate, so that its roughness is dominated by the k_η mode. After some time, the phase exchange causes the smoothening of the surface at low thickness $\bar{H} = 50$ ML, Fig. 3.10e, while after some time, both the k_η and k_{ATG} mode are visible in the surface Fourier transform, but

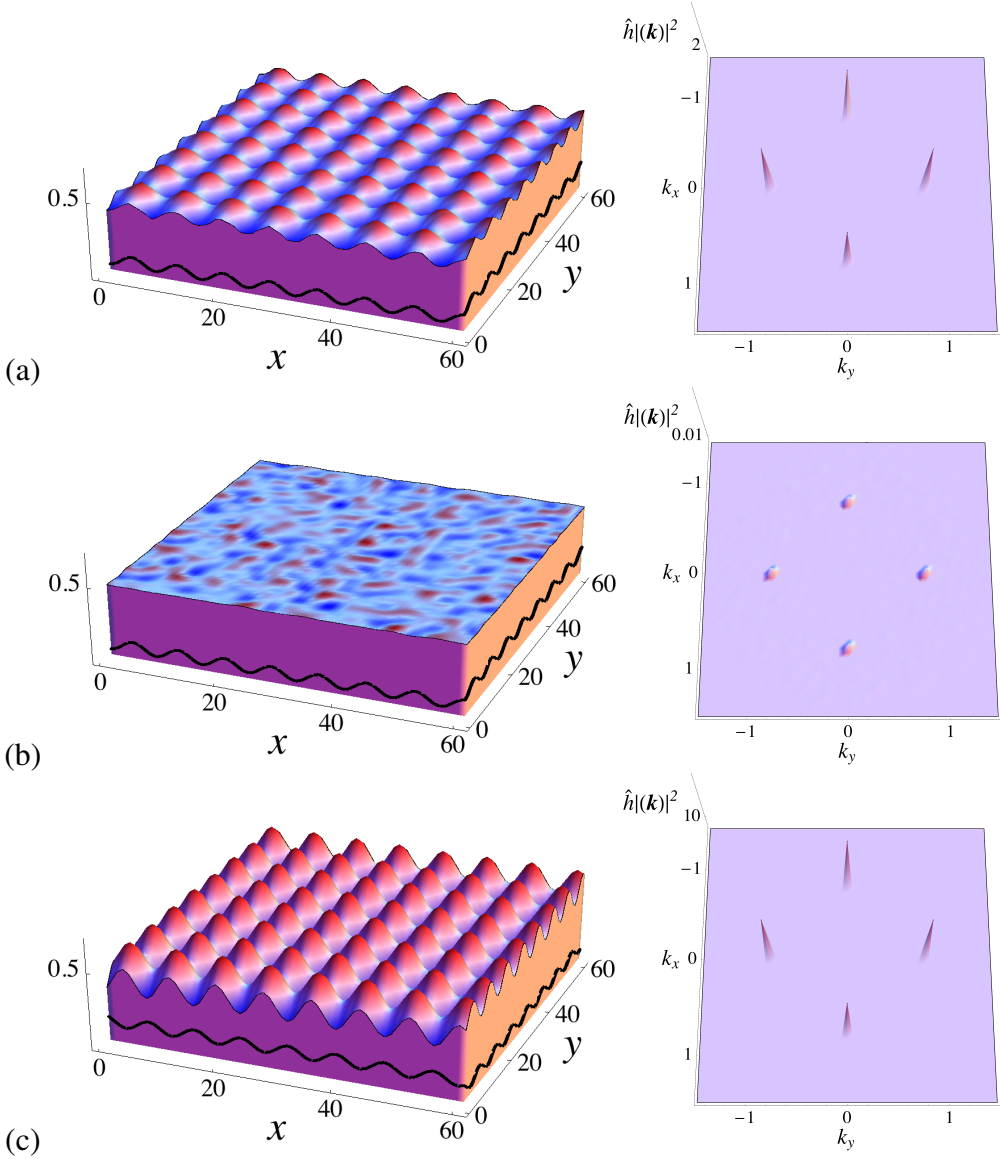


Figure 3.9: Surface geometry for the coincidence case $k_\eta = k_{\text{ATG}}$ for three different times for (a) the in-phase case ($0 t_0$), (b) at the phase exchange ($3.4 t_0$) and (c) the out-of-phase case ($8 t_0$), corresponding to the three labels (a, b, c) in the kinetic phase diagram in Fig. 3.5. The black line shows the patterned substrate. The corresponding spectrum $|\hat{h}(\mathbf{k})|^2$ is shown on the right side. The film thickness is $\tilde{H} = 50$ ML.

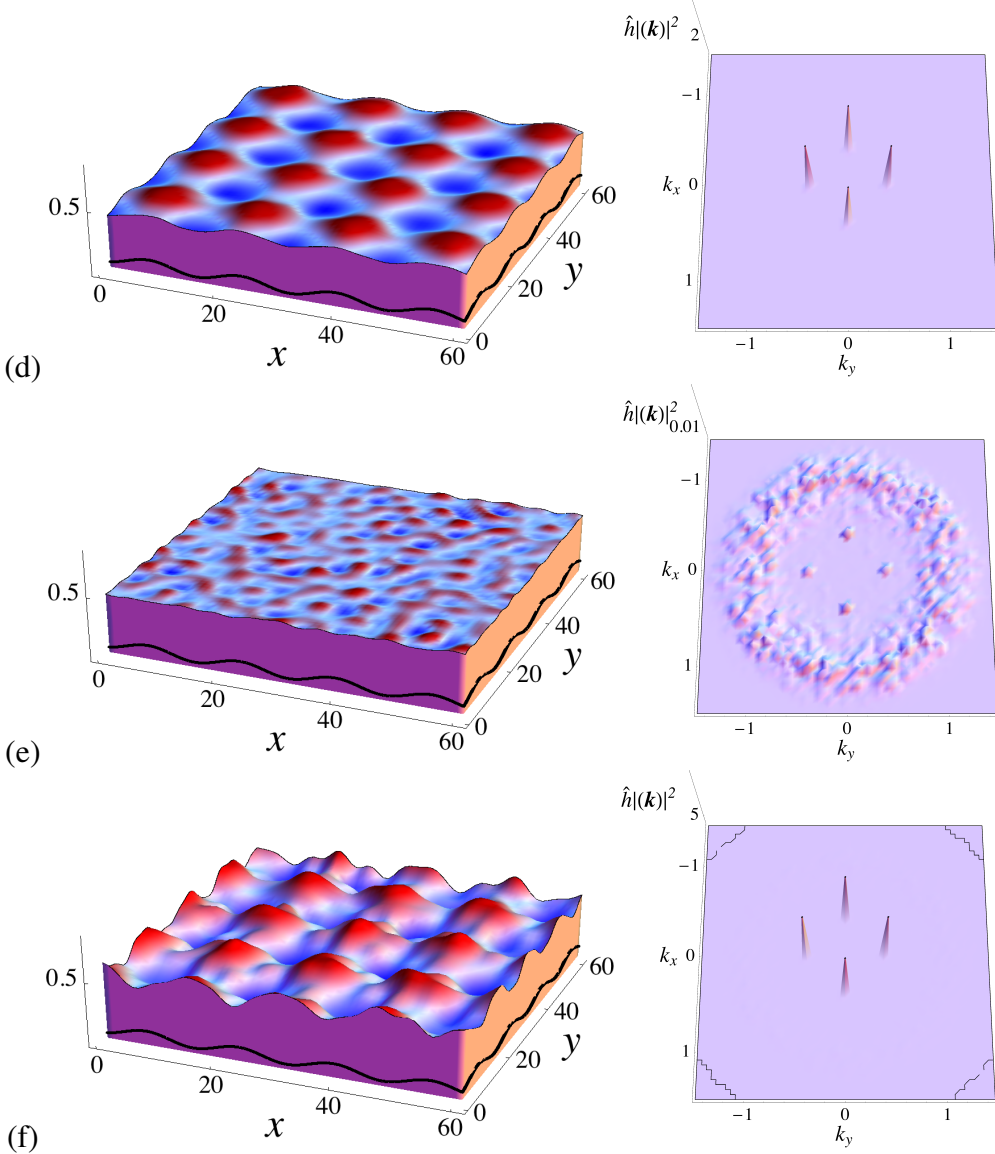


Figure 3.10: Surface geometry at $t = 10 t_0$ (d), $35 t_0$ (e) $50 t_0$ (f), corresponding to the three labels (d, e, f) in Fig. 3.8 for $k_\eta = k_{\text{ATG}}/2$. The corresponding roughness spectra are displayed in the right panels. The black line shows the pattern substrate. The film thickness is $\bar{H} = 50 \text{ ML}$.

the surface is still out-of-phase with respect to the substrate. For $\bar{H} = 100 \text{ ML}$, however, this phase exchange is hidden by the significant growth of the k_{ATG} mode which quickly becomes dominant and enforces a mainly disordered morphology, see Fig. 3.11e.

3.6 Articles

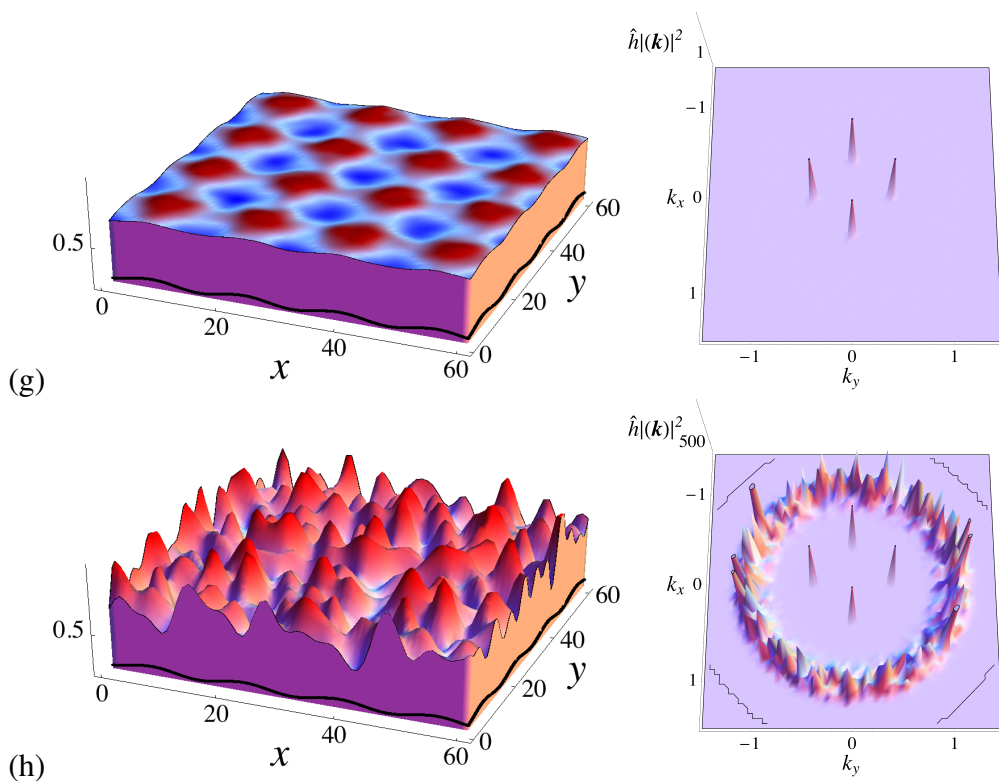


Figure 3.11: Surface geometry at $t = 10 t_0$ (g), $55 t_0$ (h), corresponding to the three labels (g, h) in Fig. 3.8 with $k_\eta = k_{\text{ATG}}/2$ and the corresponding roughness spectra (right panels). The black line is the patterned substrate. The film thickness is $\bar{H} = 100 \text{ ML}$.

Growth kinetics in a strained crystal film on a wavy patterned substrate

X Xu^{1,2}, J-N Aqua^{1,2} and T Frisch^{3,4}

¹ Institut Matériaux Microélectronique Nanoscience de Provence, Aix-Marseille Université,
UMR CNRS 6242, F-13997 Marseille, France

² Institut des Nanosciences de Paris, Université Pierre et Marie Curie, Paris 6 and CNRS UMR 7588,
4 place Jussieu, F-75252 Paris, France

³ Institut Non Linéaire de Nice, Université de Nice Sophia Antipolis, UMR CNRS 6618, 1361 routes des
Lucioles, Sophia Antipolis, F-06560 Valbonne, France

⁴ Centre de Recherche sur l'Hétéro-épitaxie et ses Applications, UPR CNRS 10, Rue Bernard Grégory,
06560 Valbonne, France

Received 27 September 2011, in final form 1 December 2011

Published 3 January 2012

Online at stacks.iop.org/JPhysCM/24/045002

Abstract

We study the combination of the Asaro–Tiller–Grinfeld morphological instability of a strained film and the organizing effect of an underlying patterned substrate. We use a continuum description of surface diffusion accounting for elasticity, surface energy and wetting interactions. We solve both the mechanical equilibrium and the growth dynamics during annealing at linear order in the film modulation amplitude. We characterize the kinetic phase diagram as a function of time, the film thickness and the ratio between the substrate and the instability wavelengths. We find that the film surface can skip from a configuration in phase with the substrate to either an out-of-phase or a non-ordered configuration, depending on the pattern wavelength and annealing time.

(Some figures may appear in colour only in the online journal)

1. Introduction

Controlling the self-organization of quantum dots is a requirement for their potential use in optical or electronic systems. Their relative position and geometric characteristics need to be finely monitored for optimizing their physical properties. One way to produce dots consists in growing coherently a crystal film on a lattice-mismatched substrate, e.g. using substrates and films made of Si and Ge. The elastic stress induces surface diffusion leading to the growth of islands which allow for partial elastic relaxation [1–4]. However, the resulting islands display some inhomogeneity which alters their quality, especially as regards their size distribution. A proposal for improving the surface characteristics is to grow islands on a patterned substrate.

Different kinds of templates have been dedicated for the growth of quantum dots using conventional optical lithography, e-beam lithography or focused ion beam (FIB) [5–10]. In some conditions, correlations are found between the pattern and the growing islands thus leading to almost regular arrays with an island separation which can be as small as 80 nm. For example, Ge dots grown on

stripes and mesas revealed ordering on the top concave part of the template [11–14]. In contrast, pit-patterned substrates produced by holographic lithography in the sub-micrometer range lead to the ordering of islands inside the pits, i.e. in the bottom convex part of the pattern [15], as found in similar geometries [16–19]. More recently, experiments on FIB nanopatterns [20, 1] showed the influence of the temperature: while islands can nucleate at low temperature inside the pits, they nucleate outside the holes at high temperature and nucleate randomly for intermediate temperature.

To get some understanding, one may recall the surface thermodynamics which rules surface diffusion. Writing $\mathcal{E}^{\text{el}}(\mathbf{r})$ the elastic energy density computed on the film free surface, the surface chemical potential is given by [21]

$$\mu = \mu_0 + \Omega\gamma\kappa(\mathbf{r}) + \Omega\mathcal{E}^{\text{el}}(\mathbf{r}), \quad (1)$$

where μ_0 is the bulk chemical potential, γ the surface energy and Ω the atomic volume. The second term stands for the energetic cost of an increase in the surface area and is proportional to the local curvature $\kappa(\mathbf{r})$ at the position \mathbf{r} on the surface. The last term describes the elastic energy density stored in an atomic volume at position \mathbf{r} . It is minimum at the

concave (top) part of a surface undulation where relaxation is maximum, while it is minimum in the convex part (bottom). In addition, the contribution from the buried film/substrate interface is maximum on the vertical of a concave region while it is minimum on the convex one. Finally, all these contributions compete with the surface energy term which is maximum at the concave part of the free surface, describing the smaller chemical bounding of an atom on top of a pattern. The complexity of this phenomena leads to a wide range of numerical and theoretical analysis. For example, Liu and co-workers [22] showed that, at equilibrium, the film surface has the same wavelength as the underlying substrate but with an anti-phase configuration. An atomistic analysis based on Monte Carlo simulations [20] showed that islands tend to locate at equilibrium on terraces separating pits rather than on stepped pit walls.

In addition to the previous energetic considerations, the surface morphology also results from the growth kinetics which favors nucleation inside a hole (as compared to a flat terrace) because of the higher number of steps which act as favorable nucleation centers. On the other hand, the computation of nucleation barriers (which is a difference of energy) shows that elastic relaxation favors island nucleation at the bottom of a pit rather than at its top, while large surface energy anisotropy favors nucleation at both places [23]. To investigate the evolution of the system, kinetic Monte Carlo (KMC) simulations were implemented to account for a pattern by adding an extra diffusion barrier [24, 25] which may depend on the localization with respect to the pattern or on an elastic term describing island relaxation. Well-ordered island arrays may be found but only in a narrow parameter range where the temperature is neither too low (when no positional order arises) nor too high (when Ostwald ripening occurs). Numerical resolution of the surface evolution equation based either on a Cahn–Hilliard phase field description of a system with a strain pattern [26], or on a mass conservation equation describing surface diffusion on a modulated substrate [27], in which elastic fields are solved using the finite element method, revealed that patterning may lead to an ordered self-organized quantum dot array.

When one considers SiGe systems, the morphological evolution of the surface depends crucially on the mismatch between the film and substrate, see, e.g., [1]. While a 2D/3D transition with island nucleation occurs at high strain, a nucleationless instability occurs at low strain and is reminiscent of the Asaro–Tiller–Grinfeld instability in strained films [28, 29]. We aim here at describing the dynamical equation governing this instability on a patterned substrate, where the competition between the instability and the pattern wavelength is a key effect. We thus consider a continuum model describing surface diffusion ruled by surface, wetting and elastic energies. In a quasi-static approximation, we solve the mechanical equilibrium equations using the small-slope approximation and study the film dynamics at linear order in the surface corrugation. The kinetic analysis reveals different states depending both on time, the pattern wavelength and the film thickness, that we summarize in a kinetic phase diagram.

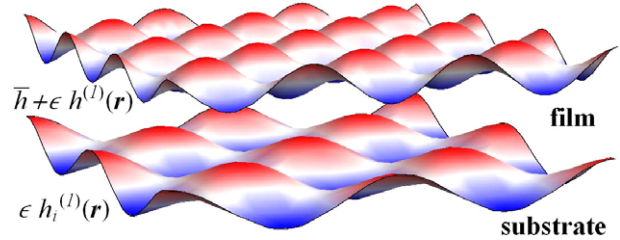


Figure 1. Geometry of a film deposited on a patterned substrate.

The substrate modulation influences the film dynamics both via elastic interactions which are long range in the growth direction and via the film initial conditions considered as pseudomorphic with the substrate. Depending on the film thickness, we find that the film surface can either stick to the substrate wavelength λ_i with an in-phase configuration or skip with time from in-phase to out-of-phase when λ_i is in the vicinity of the instability wavelength λ_{ATG} . In contrast, when λ_i is not in this vicinity, the surface is found to skip from an in-phase to a non-ordered noisy configuration characterized by the natural wavelength λ_{ATG} . In section 2, we recall the basic ingredients of the continuum description and give the growth dynamics solution at linear order in the film corrugation amplitude. In section 3, we discuss the consequences of the evolution equation for a thin film growing on an egg-carton-like pattern and characterize the kinetic phase diagram and the different possible evolutions.

2. Continuum model

2.1. Mechanical equilibrium

We consider a film coherently deposited on a substrate with a slightly different lattice parameter enforcing an elastic stress throughout the system. The substrate is supposed here to be patterned and to display a wavy surface, see figure 1. Of special interest is the interplay between the natural wavelength of the instability and the wavelength of the imposed pattern, but as we work only at linear order, no interference between the two will arise here. The film surface and the film/substrate interface are defined respectively by $z = h(\mathbf{r})$ and $h_i(\mathbf{r})$, where $\mathbf{r} = \{x, y\}$ is the two-dimensional vector perpendicular to the growth direction z . We suppose that the system undergoes a quasi-static evolution where mechanical equilibrium is always reached. Hence, the displacement vector \mathbf{u} satisfies the Lamé equations

$$\partial_n \sigma_{mn} = \mathbf{0}, \quad (2)$$

where $m, n = x, y, z$. In the linear isotropic framework, the stress tensor $\boldsymbol{\sigma}$ is related to the strain tensor \boldsymbol{e} via $\boldsymbol{\sigma} = E/(1 + \nu)[\boldsymbol{e} + \nu/(1 - 2\nu)\text{Tr}(\boldsymbol{e})\mathbb{1}]$, where E and ν are the Young modulus and Poisson ratio which are supposed to be identical in the film and substrate. We consider a reference state commensurate with the substrate so that $e_{ij} = \frac{1}{2}(\partial_j u_i + \partial_i u_j) - \hat{\delta} \mathbb{1}_{ij}$ with the misfit $\hat{\delta} = 1 - a_f/a_s$ in the film and 0 otherwise. The hypothesis of a coherent interface enforces the continuity at the interface of displacements $\mathbf{u}|_{z=h_i(\mathbf{r})^-} =$

$\mathbf{u}|_{z=h_i(\mathbf{r})^+}$ and stresses $\sigma[\mathbf{u}] \cdot \mathbf{n}_i|_{z=h_i(\mathbf{r})^-} = \sigma[\mathbf{u}] \cdot \mathbf{n}_i|_{z=h_i(\mathbf{r})^+}$, where \mathbf{n}_i is the unit vector perpendicular to the film/substrate interface. Finally, the film surface is supposed to be stress-free so that the last boundary condition is $\sigma[\mathbf{u}] \cdot \mathbf{n}|_{z=h(\mathbf{r})} = \mathbf{0}$, where \mathbf{n} is the unit vector perpendicular to the film free surface.

The Lamé equations can be solved in Fourier space $\mathcal{F}[h](\mathbf{k}) = (2\pi)^{-2} \int d\mathbf{r} e^{i\mathbf{k}\cdot\mathbf{r}} h(\mathbf{r})$ (with the shorthand notation $\hat{h}(\mathbf{k})$) using the small-slope approximation for solving the interface and free film boundary condition. Hence, the film free surface and film/substrate interface are characterized respectively by $z = \bar{h} + \epsilon h^{(1)}(\mathbf{r})$ and $h_i(\mathbf{r}) = \epsilon h_i^{(1)}(\mathbf{r})$, where \bar{h} is the film thickness and ϵ is a small parameter. The solution for the displacement vector is given in appendix B. With this solution in hand, one can compute the elastic energy density $\frac{1}{2} \sigma_{ij} e_{ij}$ at first order in ϵ and its value on the film free surface

$$\mathcal{E}^{\text{el}}(\mathbf{r}) = \mathcal{E}_0 \{1 - 2(1+\nu)\mathcal{H}[h] + 2(1+\nu)\mathcal{H}_i[h_i, \bar{h}]\}, \quad (3)$$

where $\mathcal{E}_0 = E\delta^2/(1-\nu)$ is the elastic energy density of a flat film on a flat substrate. The operators

$$\mathcal{H}[h] = \mathcal{F}^{-1}[|\mathbf{k}| \mathcal{F}[h]], \quad (4)$$

$$\mathcal{H}_i[h_i, \bar{h}] = \mathcal{F}^{-1}[|\mathbf{k}| e^{-|\mathbf{k}|\bar{h}} \mathcal{F}[h_i]], \quad (5)$$

are associated respectively with the elastic dipoles induced by the free surface, independently of the wavy interface [30], and to the buried dipoles of the interface. The exponential term $e^{-|\mathbf{k}|\bar{h}}$ is a sign of the damping of elastic interactions in the vertical direction which occurs nevertheless on the instability typical length scale which can be rather large. The configuration of minimum energy is analyzed in appendix A. When the film is not too thin, i.e. when wetting interactions are damped enough, the geometry which minimizes the total energy corresponds to a film out of phase with the substrate, which is dictated by the elastic energy. In contrast, when wetting interactions are strong enough, an in-phase geometry is favored, see appendix A.

2.2. Evolution equation

The dynamical evolution of the system is mainly ruled by surface diffusion as the bulk diffusion may be considered as negligible at the experimental working temperature. Mass conservation during annealing in the presence of surface diffusion enforces the dynamical equation

$$\partial h / \partial t = D \Delta_s \mu, \quad (6)$$

where D is a surface diffusion coefficient and Δ_s is the surface Laplacian. When one considers thin films, the general form of the surface chemical potential (1) needs to be augmented by wetting interactions between the film and the substrate. The latter can be included by adding an explicit h dependence in the surface energy $\gamma(h)$ which enforces also an additional $\Omega d\gamma/dh$ term in (1), see, e.g., [30]. The wetting potential in the case of a flat film/substrate interface may be fitted by a smooth exponential decrease with the film height, see, e.g., [31–33]. We extrapolate this result on a wavy substrate by considering a dependence on the local film height:

$$\gamma[h(\mathbf{r})] = \gamma_f(1 + c_w \exp\{-[h(\mathbf{r}) - h_i(\mathbf{r})]/\delta_w\}), \quad (7)$$

where γ_f is the thick film surface energy, while c_w and δ_w are the amplitude and range of the surface energy variation induced by wetting interactions. Eventually, in units of the space and time scales $l_0 = \gamma_f/[2(1+\nu)\mathcal{E}_0]$ and $t_0 = l_0^4/D\gamma_f$, the evolution equation is given at first order in the surface and interface slopes by

$$\frac{\partial h}{\partial t} = \Delta \{-\Delta h - \mathcal{H}[h] + \mathcal{H}_i[h_i] + a(\bar{h})(h - h_i)\}, \quad (8)$$

with the amplitude $a(\bar{h}) = c_w e^{-\bar{h}/\delta_w} / \delta_w^2$.

2.3. Solution at linear order

The evolution equation (8) is linear in h and can be solved straightforwardly in Fourier space. On a flat substrate, a single-mode perturbation $e^{i\mathbf{k}\cdot\mathbf{r}}$ grows exponentially with time $e^{\sigma t}$ with the growth rate

$$\sigma(k, \bar{h}) = -a(\bar{h}) k^2 + k^3 - k^4, \quad (9)$$

which depends only on $k = |\mathbf{k}|$. Wetting interactions induce the first stabilizing term, while elastic interactions enforce the second destabilizing term which non-analyticity is a sign of the long range elasticity. The last term originates from the surface energy stabilization which tends to smooth a surface corrugation. On a wavy interface, the source terms on the right-hand side of equation (8) must also be considered and one eventually finds

$$\hat{h}(\mathbf{k}, t; \bar{h}) = \hat{h}^0(\mathbf{k}) e^{\sigma t} - C(k, \bar{h}) \hat{h}_i(\mathbf{k}) (e^{\sigma t} - 1), \quad (10)$$

with the surface initial condition $\hat{h}^0(\mathbf{k})$ and the coefficient of the inhomogeneous solution:

$$C(k, \bar{h}) = [k^3 e^{-k\bar{h}} - a(\bar{h}) k^2] / \sigma(k, \bar{h}). \quad (11)$$

3. Results and discussion

In the following, we consider a substrate with an egg-carton shape, see figure 1, with a wavevector modulus k_i :

$$h_i(\mathbf{r}) = \frac{1}{2} \epsilon [\cos(\mathbf{k}_i^x \cdot \mathbf{r}) + \cos(\mathbf{k}_i^y \cdot \mathbf{r})], \quad (12)$$

with $\mathbf{k}_i^x = (k_i, 0)$ and $\mathbf{k}_i^y = (0, k_i)$. At time $t = 0$, we consider a film with a thickness \bar{h} which has grown by following the substrate shape so that

$$h^0(\mathbf{r}) = \bar{h} + h_i(\mathbf{r}) + \mathcal{R}, \quad (13)$$

where \mathcal{R} is a white noise which renders the intrinsic deposition noise and substrate roughness. The noise initiates growth of the different modes following the growth rate (9) but is supposed to have an amplitude at least an order of magnitude smaller than the substrate modulation in real space. In addition, as the noise is spread over all the modes, it is multiplied by an extra small parameter compared to h_i in Fourier space. Indeed, for a typical noise equally distributed in the interval $[-\epsilon/2, \epsilon/2]$, one can estimate the average over different realizations of the spectrum $(\langle |\hat{\mathcal{R}}(\mathbf{k})|^2 \rangle)^{1/2} = \epsilon^{3/2} \sqrt{N/12}$ for a system with N modes, which is negligible compared to $\hat{h}_i(\mathbf{k}_i^\alpha) = \epsilon N/4$ (for $\alpha = x, y$) in the large N limit.

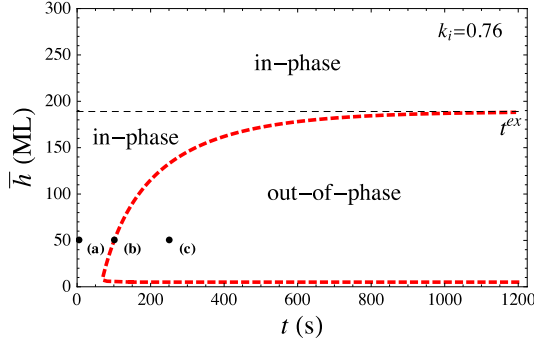


Figure 2. Kinetic phase diagram as a function of time and the film thickness \bar{h} , for $k_i = 0.76$ and parameters given in section 3.2. The red dashed line t^{ex} refers to the time when the surface undulation vanishes before (resp. after) which the film surface is in (resp. out of) phase. The horizontal black line is the threshold h^{ex} below which the phase exchange can occur. The lower dotted-dashed line refers to the thickness below which wetting interactions enforce an in-phase configuration.

3.1. Kinetic phase diagram

When time is small, $\hat{h}(\mathbf{k}, t)$ is similar to \hat{h}^0 which means, given the surface initial condition (13), that the film free surface follows the substrate shape and is therefore in phase with the substrate undulation. On the other hand, when time is large enough (but nevertheless in the regime where the film slope remains small), the surface shape is mainly ruled by two modes, the substrate mode k_i and the instability mode $k_{\max} = 3/4$ which maximizes the growth rate σ for large \bar{h} (i.e. when wetting interactions are negligible).

We first study the evolution of the unstable mode k_i for the film free surface. Given the initial condition (13) and the fact that the white noise is negligible in Fourier space compared to the k_i mode, the solution (10) behaves as $\hat{h}(\mathbf{k}_i^\alpha, t) \approx \hat{h}_i(\mathbf{k}_i^\alpha)$ for small t while it behaves as $(1 - C)\hat{h}_i(\mathbf{k}_i^\alpha) e^{\sigma(k_i, \bar{h})t}$ for large t . Hence, when C is larger than unity, $\hat{h}_i(\mathbf{k}_i^\alpha)$ has to change its sign and the surface skips from a configuration where it undulates in phase compared to the substrate to an out-of-phase configuration, where the film bumps coincide with the minima of the egg-carton substrate. In the limit of negligible wetting interactions (which is after a few deposited layers), the condition $C > 1$ leads to the upper bound $h < h^{\text{ex}}$, where $h^{\text{ex}} = -k_i^{-1} \ln(1 - k_i)$ for $k_i < 1$ when the k_i mode has a positive growth rate σ . Hence, the in- and out-of-phase exchange may only occur for a film thickness not too large as a result of the competition between the initial condition which sets an in-phase configuration and the elastic interactions which favor an out-of-phase geometry but which are exponentially damped in the vertical direction. When this condition is met, the time for the phase exchange may be estimated as $t^{\text{ex}}(k_i, \bar{h}) = \ln[C/(C - 1)]/\sigma$. At t^{ex} , the k_i mode vanishes and the modulation must decrease first in order to change its sign and continue to grow exponentially. As a direct consequence, even with an unstable mode with a positive growth rate σ , the surface roughness must go to zero first in order to allow the out-of-phase exponential growth. The phase exchange time t^{ex} increases with increasing \bar{h} as

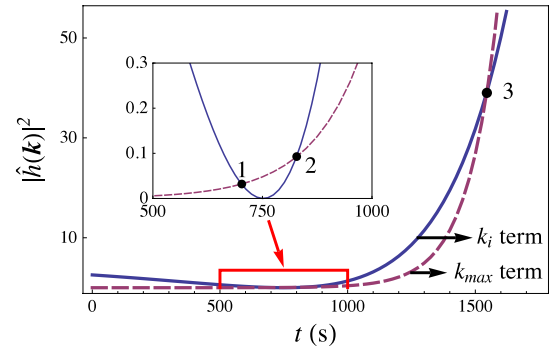


Figure 3. Evolution of the amplitude of the Fourier modes of the film surface $|\hat{h}(\mathbf{k}, t)|^2$ with time for the substrate mode $k_i = 0.42$ (blue line) and the instability mode k_{\max} (red dashed line), for $\bar{h} = 50$ ML and parameters given in section 3.2. The inset displays a zoom of the interval where the k_i mode vanishes. The typical time t_{\max} corresponds in this case to the third intersection point labeled 3.

a result of the exponential damping of elastic interactions in the vertical direction which are responsible for this exchange. These conclusions are sketched, for example, in the kinetic phase diagram of figure 2 for a substrate modulation with $k_i = 0.76$. The film/substrate out-of-phase geometry that we find here is related to the results of the dynamical analysis of a film on a patterned substrate [22], or, in another but similar geometry [34], with the quantum dot growth on either sides of a thin substrate of anticorrelated islands. Finally, we also find that, for a small enough film thickness, the wetting interactions enforce the stability of the surface, as σ is negative for every k , see, e.g., [30], which leads again to an in-phase geometry which minimizes the dominant wetting energy, see figure 2.

Besides the forcing mode k_i , the surface dynamics is also ruled by the typical mode of the instability k_{\max} . Even if it is initially induced by the noise with a small amplitude, the k_{\max} mode can overcome the k_i mode thanks to its faster growth rate on a time not too large within the linear framework and satisfying the constraint that the growing surface does not cross the film/substrate interface. The spectrum of the film roughness is given by $|\hat{h}(\mathbf{k}, t)|^2 = [(1 - C)e^{\sigma t} + C]^2 |\hat{h}_i(\mathbf{k})|^2 + e^{2\sigma t} |\mathcal{R}(\mathbf{k})|^2$. One can then compare the amplitudes of the k_i and k_{\max} modes. In the case where the k_i mode displays a phase exchange, its amplitude first vanishes and then increases again, contrary to the k_{\max} mode which keeps on growing. We consider the time t_{\max} when the two amplitudes are equal and when the k_{\max} mode is finally becoming dominant, see figure 3. This time is the typical time after which the instability may be considered as fully developed, even though the noise may be visible before this time. When k_i is still a growing mode but not in the vicinity of k_{\max} (contrary to the case of figure 2), t_{\max} is not too large and may be observed before the free surface crosses the film/substrate interface. Hence, a new line is visible in the kinetic phase diagram which delimits the initial configuration which is in phase with the substrate, with a configuration where the instability is fully developed, see figure 4. The time t^{ex} for the phase exchange is also indicated in figure 2

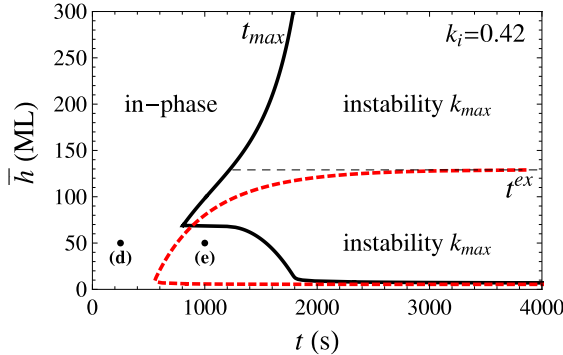


Figure 4. Kinetic phase diagram for $k_i = 0.42$. The black line refers to the typical time t_{\max} before which the film is mainly in phase with the substrate at k_i and after which the instability is fully developed with the typical wavevector k_{\max} . The red dashed line characterizes the in- and out-of-phase exchange time t^{ex} of the sole k_i mode which occurs for $h < h^{\text{ex}}$ (horizontal thin dashed line). The latter phase exchange is nevertheless often hidden by the growing mode k_{\max} . Note that the cusp in the plot of t_{\max} arises merely from a change in the intersections between the k_i and k_{\max} spectra in figure 3.

even though it is hidden by the instability development. The decrease in the growth rate σ causes naturally the increase in the time t^{ex} necessary for this time exchange.

3.2. Numerical resolution

In order to picture the surface evolution during annealing in the linear regime which corresponds to the instability regime in SiGe experiments, we perform a numerical analysis of equation (10) using a multi-mode computation of the evolution equation (8). We choose to depict an Si_{0.75}Ge_{0.25} film on an Si substrate. At the working temperature $T = 700^\circ\text{C}$, one finds the instability scales [35] $l_0 = 27$ nm and $t_0 = 25$ s. We extrapolate first-principles calculations of wetting interactions [33] to this system by considering $c_w = 0.09$ and we set δ_w equal to one lattice parameter. The initial noise is considered to correspond to a white noise with a roughness of 1 monolayer (ML). We consider a 128×128 box with periodic boundary conditions.

We consider first $k_i = 0.76$ which lies in the vicinity of the most unstable wavevector. The growth rate of the k_i mode is large enough so that it remains the dominant mode of the surface and t_{\max} is too large to be depicted. The kinetic phase diagram when the system is still in the linear regime and when the film free surface is above the substrate is shown in figure 2. For this k_i value, the upper bound for the phase exchange to occur is $h^{\text{ex}} = 189$ ML. The geometry of a 50 ML thick film is plotted for three different times (a) for the in-phase configuration, (b) at the phase exchange and (c) for the out-of-phase case in figure 5. The corresponding spectra $|\hat{h}(\mathbf{k})|^2$ are dominated by the k_i mode except at the phase exchange where it vanishes before changing its sign; as a consequence, the typical spectrum of the instability displays a maximum around k_{\max} . Hence, after the phase exchange, the surface is nearly perfectly ordered with maxima located on top of the substrate minima in the valleys of the substrate undulation. In contrast, for a larger film thickness, the elastic

interactions with the substrate are sufficiently damped so that the initial in-phase configuration (a) is the only stage of the instability and the surface maxima are located on top of the substrate ones. Hence, the fact that k_i lies in the vicinity of k_{\max} corresponds to the optimal ordering of the surface during the instability evolution.

On the other hand, when k_i is an unstable mode but not in the vicinity of the instability wavevector, the competition between these two modes comes into play and affects the kinetic phase diagram, see figure 4. The film first grows in phase with the substrate but the instability with k_{\max} occurs before the phase exchange may happen. The geometry of the surface for $k_i = 0.42$ is displayed in figure 6(d) at an early time, when the film is mainly in phase with the substrate and when the roughness spectrum is dominated by the k_i mode and (e) at larger time when the instability is fully developed with a spectrum characterized by the k_i mode in addition to the instability spectrum centered at k_{\max} but with a finite variance (the corresponding times are indicated in figure 4). The coexistence of the two spectra at k_i and around k_{\max} results in a surface which mainly looks like a non-ordered one.

Finally, when the substrate modulation corresponds to a stable mode for the ATG instability, we find that the surface quickly skips from an in-phase to an out-of-phase configuration which does not grow (except at low thickness where wetting interactions enforce an in-phase geometry). However, the instability increases at larger wavelengths and the instability then fully develops after some time t_{\max} . The corresponding kinetic phase diagram is plotted in figure 7 for $k_i = 1.46$ which corresponds to a pattern with a small enough wavelength.

4. Conclusion

We have studied the dynamics of the morphological instability of a strained film on a modulated substrate. We solved both the mechanical equilibrium and evolution equation at linear order in the film modulation amplitude. We find different states depending on time, the pattern wavelength and the film thickness. The substrate modulation influences the film dynamics both via elastic interactions and via the film initial conditions when the film initially follows the substrate shape. When the substrate wavelength λ_i lies in the vicinity of the ATG instability wavelength λ_{ATG} , the film surface is ruled mainly by λ_i with an in-phase configuration for large enough deposited height \bar{h} while it skips with time from in phase to out of phase when \bar{h} is not too large. In contrast, when λ_i is not in the vicinity of λ_{ATG} , the film skips from an in-phase to a random configuration characteristic of the natural instability on a flat substrate. These different configurations which characterize the initial stage of the elastic instability exhibit corrugations which develop either in or out of the valleys of a patterned substrate. Experiments found islands which develop in or out of these valleys depending on the experimental conditions. However, the present analysis which is restricted to the initial instability regime is not sufficient to investigate the further development of islands arising from the initial instability, and one may not draw a strong conclusion from

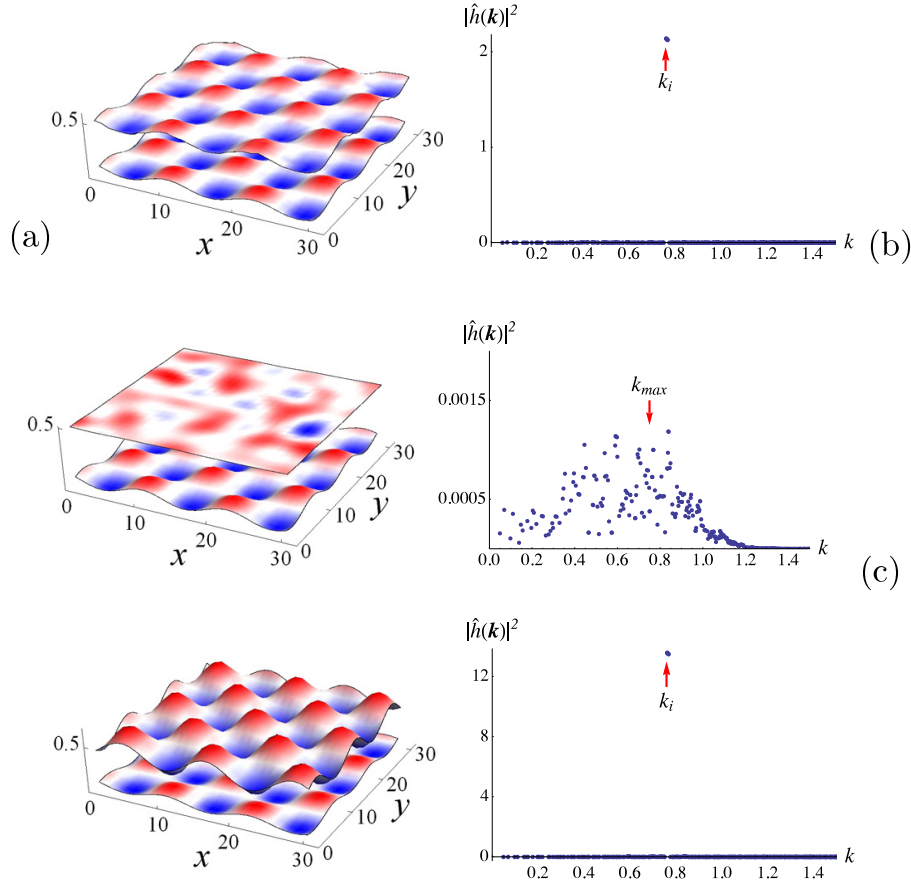


Figure 5. Surface geometry for three different times for (a) the in-phase case, (b) at the phase exchange and (c) in the out-of-phase case, corresponding to the three labels in the kinetic phase diagram in figure 2. The wavevector of the substrate is $k_i = 0.76$ and lies in the vicinity of the ATG instability wavevector $k_{max} = 0.75$. The corresponding spectrum $|\hat{h}(\mathbf{k})|^2$ is shown on the right side. At the phase exchange time, the roughness is vanishing (even though the growth rate $\sigma(k_i)$ is positive) so that the spectrum displays many modes but with a smaller amplitude compared to the (a) and (c) cases. The film thickness is $\bar{h} = 50$ ML and annealing times, 0 s (top), 100 s (middle) and 250 s (bottom).

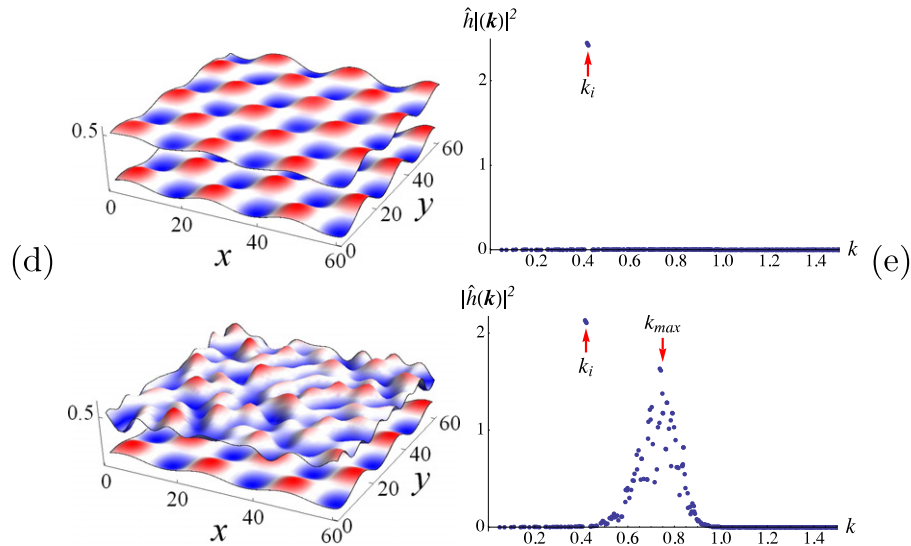


Figure 6. Surface geometry at an early time (top) and larger time (down) corresponding to the two labels of figure 4 with $k_i = 0.42$ and the corresponding roughness spectra (right panels). The film thickness is $\bar{h} = 50$ ML and anneal times, 250 s (top) and 1000 s (bottom).

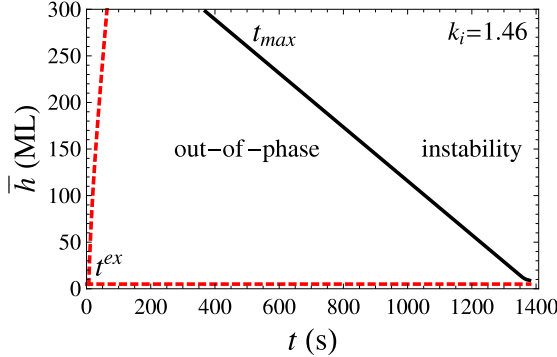


Figure 7. Kinetic phase diagram for $k_i = 1.46$ where the pattern wavelength is small enough compared to the instability wavelength. The film changes quickly (dashed red line) from an in-phase to an out-of-phase geometry but which does not grow. The instability keeps on growing and overcomes the k_i mode after the time t_{\max} (solid black line).

this sole analysis. Further analysis in the fully developed island regime which will allow a more instructive comparison with experimental findings is under investigation.

Appendix A. Equilibrium state

The calculation of the energy of a film/substrate geometry involves both the elastic and surface energies, with the latter including the wetting effect. Elastic energy may be computed from the surface elastic energy density (3) by functional integration [36], and is given here by

$$E_{\text{tot}}^{\text{el}} = \mathcal{E}^0 \int d\mathbf{r} \{h(\mathbf{r}) - \frac{1}{2} \omega h(\mathbf{r}) \mathcal{H}[h](\mathbf{r}) + \omega h(\mathbf{r}) \mathcal{H}_i[h_i](\mathbf{r})\}. \quad (\text{A.1})$$

On the other hand, the surface energy is merely $E^s = \int d\mathbf{r} \gamma[h(\mathbf{r})] \sqrt{1 + |\nabla h|^2}$, where the film/substrate wetting interactions are embedded in the \mathbf{r} -dependent surface energy γ .

For a given substrate with a cosine shape, energetic calculation without wetting [22] show that the configuration with lowest energy corresponds to a film with the same wavevector as the underlying substrate but in an out-of-phase geometry. For a film with the same wavevector \mathbf{k} as the substrate but with a phase shift φ , $h_i(\mathbf{r}) = A_i e^{i\mathbf{k}\cdot\mathbf{r}}$ and $h(\mathbf{r}) = \bar{h} + A e^{i\mathbf{k}\cdot\mathbf{r}+\varphi}$, we find $E^{\text{tot}} \propto B(\bar{h}, k_i) \cos \varphi$, where $B(\bar{h}, k) = |\mathbf{k}|e^{-|\mathbf{k}|\bar{h}} - c_w/\delta_w^2 e^{-\bar{h}/\delta_w}$. Thus the sign of B gives the configuration of minimum energy. The root of $B(\bar{h}, k) = 0$ is easily found and is plotted in figure A.1 in the region of interest. The amplitude B is always negative when \bar{h} is smaller than this root and is associated with a minimum at $\varphi = 0$ where the film is in phase with the substrate. The elastic energy is always minimum for an out-of-phase configuration and the latter state is therefore enforced by wetting interactions which are indeed minimum in such an in-phase geometry. In contrast, when \bar{h} is larger than this root, B is positive and the minimum energy is found for $\varphi = \pm\pi$ which corresponds to an out-of-phase configuration which minimizes the elastic energy. Note that these results apply to

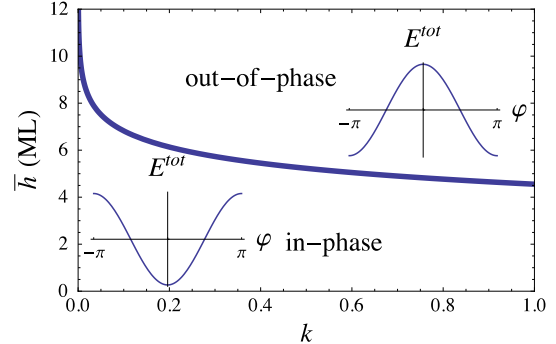


Figure A.1. State of lowest energy for a film of thickness \bar{h} with the same wavevector k as the substrate. The thick solid line corresponds to $B(\bar{h}, k_i) = 0$. The equilibrium state corresponds to a film in phase with the substrate below the thick solid line, and to an out-of-phase configuration above. Insets display the total energy as a function of the phase φ between the film and substrate which is indeed minimum at $\varphi = 0$ (resp. π) below (resp. above) the line.

the equilibrium state but are not relevant to explain the kinetic phase diagram where wetting interactions are damped for the large film thicknesses under scrutiny.

Appendix B. Displacement vector

The displacement vector which satisfies the Lamé equations and boundary conditions given in section 2.1 can be found in the small-slope approximation where both the film free surface and the film/substrate interface are supposed to display small slopes. Indeed, in this framework, the solution can be sought as a series in ϵ characterizing the slope amplitude, see section 2.1. At first order in ϵ , one finds in the film

$$\mathbf{u} = \bar{\delta} \frac{1 + \nu}{1 - \nu} z \begin{pmatrix} 0 \\ 0 \\ 1 \end{pmatrix} + \mathbf{u}^{(1)}(h) + \mathbf{u}_i^{(1)}(h_i), \quad (\text{B.1})$$

with a correction due to the free surface, see [35]:

$$\begin{aligned} \mathbf{u}^{(1)}(h) &= \bar{\delta} \frac{1 + \nu}{1 - \nu} \frac{e^{|\mathbf{k}|(z - \bar{h})}}{|\mathbf{k}|} \hat{h}^{(1)}(\mathbf{k}) \\ &\times \begin{pmatrix} [2(1 - \nu) + |\mathbf{k}|(z - \bar{h})] i k_x \\ [2(1 - \nu) + |\mathbf{k}|(z - \bar{h})] i k_y \\ [1 - 2\nu - |\mathbf{k}|(z - \bar{h})] |\mathbf{k}| \end{pmatrix}, \end{aligned} \quad (\text{B.2})$$

and a correction due to the buried interface:

$$\begin{aligned} \mathbf{u}_i^{(1)}(h_i) &= -\bar{\delta} \frac{1 + \nu}{1 - \nu} \frac{1}{2|\mathbf{k}_i|} \hat{h}_i^{(1)}(\mathbf{k}) \\ &\times \begin{pmatrix} \{e^{-|\mathbf{k}_i|z} + e^{|\mathbf{k}_i|(z - 2\bar{h})}[(3 - 4\nu) + 2|\mathbf{k}_i|(z - \bar{h})]\} i k_i^x \\ \{e^{-|\mathbf{k}_i|z} + e^{|\mathbf{k}_i|(z - 2\bar{h})}[(3 - 4\nu) + 2|\mathbf{k}_i|(z - \bar{h})]\} i k_i^y \\ \{e^{-|\mathbf{k}_i|z} + e^{|\mathbf{k}_i|(z - 2\bar{h})}[(3 - 4\nu) - 2|\mathbf{k}_i|(z - \bar{h})]\} |\mathbf{k}_i| \end{pmatrix} \end{aligned} \quad (\text{B.3})$$

which is similar to the results found in [37].

References

- [1] Berbezier I and Ronda A 2009 SiGe nanostructures *Surf. Sci. Rep.* **64** 47
- [2] Stangl J, Holý V and Bauer G 2004 Structural properties of self-organized semiconductor nanostructures *Rev. Mod. Phys.* **76** 725
- [3] Teichert C 2002 Self organization of nanostructures in semiconductor heteroepitaxy *Phys. Rep.* **365** 335
- [4] Voigtländer B 2001 Fundamental processes in Si/Si and Ge/Si epitaxy studied by scanning tunneling microscopy during growth *Surf. Sci. Rep.* **43** 127
- [5] Mui D S L, Leonard D, Coldren L A and Petroff P M 1995 Surface migration induced self-aligned InAs islands grown by molecular beam epitaxy *Appl. Phys. Lett.* **66** 1620
- [6] Seifert W, Carlsson N, Petersson A, Wernersson L E and Samuelson L 1996 Alignment of InP Stranski-Krastanow dots by growth on patterned GaAs/GaInP surfaces *Appl. Phys. Lett.* **68** 1684
- [7] Ishikawa T, Kohmoto S and Asakawa K 1998 Site control of self-organized InAs dots on GaAs substrates by *in situ* electron-beam lithography and molecular-beam epitaxy *Appl. Phys. Lett.* **73** 1712
- [8] Konkar A, Madhukar A and Chen P 1998 Stress-engineered spatially selective self-assembly of strained InAs quantum dots on nonplanar patterned GaAs(001) substrates *Appl. Phys. Lett.* **72** 220
- [9] Kim E S, Usami N and Shiraki Y 1999 Selective epitaxial growth of dot structures on patterned Si substrates by gas source molecular beam epitaxy *Semicond. Sci. Technol.* **14** 257
- [10] Szkutnik P D, Sgarlata A, Balzarotti A, Motta N, Ronda A and Berbezier I 2007 Early stage of Ge growth on Si(001) vicinal surfaces with an 8° miscut along [110] *Phys. Rev. B* **75** 033305
- [11] Kamins T I and Stanley Williams R 1997 Lithographic positioning of self-assembled Ge islands on Si(001) *Appl. Phys. Lett.* **71** 1201
- [12] Jin G, Liu J L, Thomas S G, Luo Y H, Wang K L and Nguyen B-Y 1999 Controlled arrangement of self-organized Ge islands on patterned Si(001) substrates *Appl. Phys. Lett.* **75** 2752
- [13] Kitajima T, Liu B and Leone S R 2002 Two-dimensional periodic alignment of self-assembled Ge islands on patterned Si(001) surfaces *Appl. Phys. Lett.* **80** 497
- [14] Yang B, Liu F and Lagally M G 2004 Local strain-mediated chemical potential control of quantum dot self-organization in heteroepitaxy *Phys. Rev. Lett.* **92** 025502
- [15] Zhong Z, Schwingen W, Schäffler F, Bauer G, Vastola G, Montalenti F and Miglio L 2007 Delayed plastic relaxation on patterned Si substrates: coherent SiGe pyramids with dominant {111} facets *Phys. Rev. Lett.* **98** 176102
- [16] Vescan L, Stoica T, Hollander B, Nassiopoulos A, Olzierski A, Raptis I and Sutter E 2003 Self-assembling of Ge on finite Si(001) areas comparable with the island size *Appl. Phys. Lett.* **82** 3517
- [17] Zhong Z, Halilovic A, Muhlberger M, Schaffler F and Bauer G 2003 Ge island formation on stripe-patterned Si(001) substrates *Appl. Phys. Lett.* **82** 445
- [18] Zhong Z, Halilovic A, Fromherz T, Schaffler F and Bauer G 2003 Two-dimensional periodic positioning of self-assembled Ge islands on prepatterned Si(001) substrates *Appl. Phys. Lett.* **82** 4779
- [19] Sanduijav B, Matei D, Chen G and Springholz G 2009 Shape transitions and island nucleation for Si/Ge molecular beam epitaxy on stripe-patterned Si(001) substrate *Phys. Rev. B* **80** 125329
- [20] Pascale A, Berbezier I, Ronda A and Kelires P C 2008 Self-assembly and ordering mechanisms of Ge islands on prepatterned Si(001) *Phys. Rev. B* **77** 075311
- [21] Srolovitz D J 1989 On the stability of surfaces of stressed solids *Acta Metall.* **37** 621
- [22] Wang H, Zhang Y and Liu F 2008 Enhanced growth instability of strained film on wavy substrate *J. Appl. Phys.* **104** 054301
- [23] Hu H, Gao H J and Liu F 2008 Theory of directed nucleation of strained islands on patterned substrates *Phys. Rev. Lett.* **101** 216102
- [24] Nurminen L, Kuronen A and Kaski K 2000 Kinetic Monte Carlo simulation of nucleation on patterned substrates *Phys. Rev. B* **63** 035407
- [25] Bergamaschini R, Montalenti F and Miglio L 2010 Optimal growth conditions for selective Ge islands positioning on pit-patterned Si(001) *Nanosc. Res. Lett.* **5** 1873
- [26] Wise S M, Lowengrub J S, Kim J S, Thornton K, Voorhees P W and Johnson W C 2005 Quantum dot formation on a strain-patterned epitaxial thin film *Appl. Phys. Lett.* **87** 133102
- [27] Liu P, Lu C and Zhang Y W 2007 Formation of surface structures during heteroepitaxial thin film growth on prepatterned substrates *Phys. Rev. B* **76** 085336
- [28] Asaro R J and Tiller W A 1972 Interface morphology development during stress-corrosion cracking: part 1. Via surface diffusion *Metall. Trans.* **3** 1789
- [29] Grinfeld M A 1986 Instability of the separation boundary between a nonhydrostatically stressed elastic body and a melt *Sov. Phys.—Dokl.* **31** 831
- [30] Aqua J-N, Frisch T and Verga A 2007 Nonlinear evolution of a morphological instability in a strained epitaxial film *Phys. Rev. B* **76** 165319
- [31] Chiu C-H and Gao H 1995 A numerical study of stress controlled surface diffusion during epitaxial film growth *Thin Films: Stresses and Mechanical Properties V (MRS Symposia Proceedings vol 356)* ed S P Baker *et al* (Pittsburgh, PA: Materials Research Society) p 33
- [32] Müller P and Kern R 1996 The physical origin of the two-dimensional towards three-dimensional coherent epitaxial Stranski-Krastanov transition *Appl. Surf. Sci.* **102** 6
- [33] Lu G-H and Liu F 2005 Towards quantitative understanding of formation and stability of Ge hut islands on Si(001) *Phys. Rev. Lett.* **94** 176103
- [34] Ni Y and He L H 2010 Spontaneous formation of vertically anticorrelated epitaxial islands on ultrathin substrates *Appl. Phys. Lett.* **97** 261911
- [35] Aqua J-N and Frisch T 2010 Influence of surface energy anisotropy on the dynamics of quantum dot growth *Phys. Rev. B* **82** 085322
- [36] Rice J R and Chuang T-J 1981 Energy variations in diffusive cavity growth *J. Am. Ceram. Soc.* **64** 46
- [37] Huang Z-F and Desai R C 2002 Epitaxial growth in dislocation-free strained alloy films: morphological and compositional instabilities *Phys. Rev. B* **65** 205419



Crystal growth / Croissance cristalline

Growth of a strained epitaxial film on a patterned substrate

Croissance d'un film épitaxié contraint sur un substrat patterné

Xianbin Xu^a, Jean-Noël Aqua^{a,*}, Thomas Frisch^b

^a Institut des nanosciences de Paris, université Pierre-et-Marie-Curie-Paris-6, CNRS UMR 7588, 4, place Jussieu, 75252 Paris, France

^b Institut non linéaire de Nice, université de Nice-Sophia Antipolis, CNRS UMR 6618, 1361, routes des Lucioles, 06560 Valbonne, France

ARTICLE INFO

Article history:

Available online 1 February 2013

Keywords:

Strained epitaxial film
Asaro-Tiller-Grinfel'd instability
Patterning

Mots-clés :

Film épitaxié contraint
Instabilité d'Asaro-Tiller-Grinfel'd
Structuration

ABSTRACT

We study the influence of the growth kinetics on the Asaro-Tiller-Grinfel'd instability of a thin film deposited on a patterned substrate. We use a continuum model that we solve at first order in the surface slope. Both wetting interactions and elastic fields induced by the film/substrate interface introduce an explicit dependence on the film thickness. As a consequence, the translational symmetry in the growth direction is broken and the deposition flux cannot be trivially accounted for. Similarly to the evolution during annealing, the instability can skip during growth from an in-phase to an out-of-phase geometry depending on the growth duration and film thickness. We compare the evolution of the instability using different deposition fluxes. We find that the kinetic phase diagram found in the annealing case also explains the evolution during growth in usual growth conditions.

© 2012 Académie des sciences. Published by Elsevier Masson SAS. All rights reserved.

RÉSUMÉ

Nous étudions l'influence de la cinétique de croissance sur l'instabilité d'Asaro-Tiller-Grinfel'd qui se développe sur un film mince sur un substrat structuré. Nous utilisons un modèle continu qui est résolu au premier ordre en la pente de la surface. Les interactions de mouillage ainsi que le champ élastique induit par l'interface film/substrat introduisent une dépendance explicite dans l'épaisseur du film. En conséquence, la symétrie par translation dans la direction de croissance est brisée et le flux de déposition n'est pas un paramètre trivial de l'instabilité. Comme dans le cas du recuit, nous trouvons que l'instabilité peut évoluer d'une configuration en phase vers une configuration en opposition de phase avec le substrat, en fonction du temps de déposition et de l'épaisseur du film. Nous comparons l'évolution de l'instabilité pour différents flux de croissance. Le diagramme des phases cinétique obtenu dans le cas du recuit rend aussi compte de l'évolution du film lors de la croissance dans ses conditions courantes.

© 2012 Académie des sciences. Published by Elsevier Masson SAS. All rights reserved.

* Corresponding author.

E-mail address: aqua@insp.jussieu.fr (J.-N. Aqua).

1. Introduction

Controlling the self-organization of quantum dots is a requirement for their potential use in optical or electronic systems. Their position, geometry and size distribution need to be precisely defined if one wants to draw benefit of their physical properties. This control addresses fundamental questions regarding the growth mechanisms of quantum dots (QDs) and the interplay between self-organization and an external forcing. The coherent deposition of a crystal film on a lattice-mismatched substrate is known to be a good way to generate QDs following the Stransky-Krastanov growth mode, where strain relaxation leads to an island after the completion of a wetting layer [1,2]. However, when grown on a flat substrate, the randomness of surface diffusion leads to disordered objects with a significant size dispersion. Recent developments have been made to combine the strain induced self-assembly with surface patterning in an effort to improve the size uniformity and spatial order [3].

Different kinds of templates have been dedicated to the growth of quantum dots using optical lithography, e-beam lithography, focused ion-beam (FIB), vicinal substrates, growth instabilities, etc. [3–9]. In some conditions, a strong correlation is found between the pattern and the growing islands leading to regular arrays. For example, Ge dots grown on stripes and mesas revealed ordering on the top concave part of the template [10–13]. On the contrary, pit-patterned substrates produced by holographic lithography in the sub-micrometer range lead to ordering of islands inside the pits, i.e. in the bottom convex part of the pattern, see e.g. Ref. [14], as found in similar geometries [15–18]. More recently, experiments on FIB nano-patterns [3,19] evidenced the influence of the temperature: while islands nucleate at low temperature inside the pits, they nucleate outside at high temperature and randomly at intermediate temperature.

On the theoretical front, no clear and comprehensive description of the preferential growth of islands on a pattern arises. As regards equilibrium, Yang, Liu and Lagally [13] showed that local minima of the surface chemical potential arise in convex regions due to an enhanced strain relaxation, so that growth should occur preferentially on top of the pattern. On the other hand, Monte Carlo simulations [19] showed that equilibrium corresponds to dots sitting between holes, whereas metastable states are found at low T , where dots grow in the pits. Finally, note that a simple calculation assuming a sinusoidal surface and pattern shapes [20] showed that the geometry which minimizes the energy corresponds to a substrate out-of-phase with respect to the substrate where the surface maxima lie on top of the substrate minima. As regards kinetics, the computation of the variation of the nucleation barrier due to the sole elastic relaxation showed that nucleation should be directed in the bottom of a pit [21]. Finally, kinetic Monte Carlo simulations using a basic description of elastic relaxation with a given chemical potential for different islands volume, argued that, whereas the most energetically favorable sites are in the center of the pits, nucleation occurs randomly at low T , and preferentially in the holes at intermediate and high T , the latter undergoing a significant Ostwald ripening. Our goal is to clarify the different outcomes and to investigate the ordering resulting from the diffusion equation on a surface which describes the essential mechanisms at work on large scales.

The island growth may follow different pathways. In SiGe systems, islands nucleate spontaneously during an abrupt 2D–3D transition when the strain is high enough, i.e. concerning a $\text{Si}_{1-x}\text{Ge}_x$ film on Si, when x is high enough. However, when the strain is not too large, the island growth follows an initial nucleationless morphological instability [22] reminiscent of the Asaro-Tiller-Grinfel'd (ATG) instability [23,24]. The absence of nucleation in this case is a promising route for increasing the spatial order resulting from the island self-organization, especially when growth occurs on top of a patterned substrate. We aim here at describing the evolution governing this instability on a patterned substrate. We performed in Ref. [25] a linear analysis of this instability on a pattern for a given film thickness. It corresponds to experiments where one grows a film one a time scale where mass transport does not have time to occur, and then performs annealing where the instability occurs. We investigate here the influence of the growth kinetics on the instability development and study the evolution during deposition also and its dependence on the flux.

We consider a continuum model describing surface diffusion ruled by surface energy, elastic relaxation and wetting interaction between the film and the substrate. Using a quasi-static approximation, we find the mechanical equilibrium solution within the small-slope approximation and solve the film evolution at linear order in the surface corrugation. We find different geometries depending on the pattern wavelength, film thickness, annealing time, and deposition flux. The film can either mainly develop a corrugation equal to the substrate shape but either in-phase or out-of-phase, or develop a ‘classic’ ATG-like morphology with little impact of the pattern. We compare these results with the dynamics resulting from the annealing case and find that the kinetic phase diagram which gives the typical geometry as a function of time and film thickness, is still relevant under deposition when typical growth conditions are used. Of special interest is the time where a phase shift occurs, i.e. where the instability is first in-phase with the substrate, vanishes and subsequently develops an out-of-phase configuration [25]. This change of geometry is important for the localization of the subsequent quantum dots which will grow on the basis of the instability initial stage.

2. Continuum model

We describe the hetero-epitaxial system by a film with a free surface $z = h(\mathbf{r}, t)$, where z is the growth direction and $\mathbf{r} = (x, y)$, deposited on a substrate with an interface $z = h_i(\mathbf{r})$. The lattice mismatch between the film and substrate is $m = 1 - a_f/a_s$, with the film a_f and substrate a_s lattice parameters. Mechanical equilibrium is reached on the instability time scale so that the Navier-Lamé equations, $\partial_t \sigma_{ij} = \mathbf{0}$, apply in the entire system. The film surface is supposed to be

free of stress, while the film/substrate interface is coherent, with the continuity of displacements and forces. An analytical solution of the Navier–Lamé equations can be found in Fourier space $\mathcal{F}[h](\mathbf{k}) = (2\pi)^{-2} \int d\mathbf{r} e^{i\mathbf{k}\cdot\mathbf{r}} h(\mathbf{r})$ when using the small-slope approximation for solving the interface and free film boundary conditions. Given the elastic displacements and strain tensor \mathbf{e} , one can compute the elastic energy density $\mathcal{E}^{el} = \frac{1}{2} \sigma_{ij} e_{ij}$ at first order, which reads on the surface [25]

$$\mathcal{E}^{el}(\mathbf{r}) = \mathcal{E}_0 \{ 1 - 2(1 + \nu) \mathcal{H}[h] + 2(1 + \nu) \mathcal{H}_i[h_i, \bar{h}] \} \quad (1)$$

where $\mathcal{E}_0 = Ym^2/(1 - \nu)$ is the elastic energy density of a flat film on a flat substrate, while ν and Y are the film Poisson ratio and Young modulus respectively. The operators

$$\mathcal{H}[h] = \mathcal{F}^{-1} [|\mathbf{k}| \mathcal{F}[h]] \quad (2)$$

$$\mathcal{H}_i[h_i, \bar{h}] = \mathcal{F}^{-1} [|\mathbf{k}| e^{-|\mathbf{k}|\bar{h}} \mathcal{F}[h_i]] \quad (3)$$

are associated respectively with the elastic dipoles induced by the free surface and to the buried dipoles of the film/substrate interface which involve the mean film thickness \bar{h} .

The morphological evolution that we study is ruled solely by surface diffusion, which is relevant for experiments at not too high temperature where intermixing could also come into play. The diffusion flux on the surface enforces the mass conservation equation

$$\frac{\partial h(\mathbf{r}, t)}{\partial t} = D \Delta_s \mu + F \quad (4)$$

where D is a surface diffusion coefficient, Δ_s is the surface Laplacian, μ is the chemical potential and F is the deposition flux. The chemical potential μ is the sum of the elastic energy on the surface $\mathcal{E}^{el}(\mathbf{r}) a_f^3$, and a term describing the surface energy. Wetting interactions between the film and the substrate induce a dependence of the surface energy on the film thickness h when the latter is a few atomic layer large. In order to depict SiGe systems where a small variation of γ is found [26], we decompose the latter dependence as $\gamma(h) = \gamma_f(1 + \delta\gamma_h)$, where γ_f is the pure film surface energy while $\delta\gamma_h = c_w \exp(-h/\delta_w)$, with the amplitude c_w and decay length δ_w . Given that the local thickness is $h(\mathbf{r}) - h_i(\mathbf{r})$, we consider on a patterned substrate the dependence $\gamma(h - h_i)$. The surface contribution to the chemical potential is thence $\gamma(h - h_i)\kappa + \frac{\partial\gamma}{\partial h} \frac{1}{\sqrt{1+|\nabla h|^2}}$, where κ is the surface curvature equal to $-\Delta h$ at first order in the surface slope. Eventually, in units of the space and time scales $l_0 = \gamma_f/2(1 + \nu)\mathcal{E}_0$ and $t_0 = l_0^4/D\gamma_f$, the evolution equation at first order in the surface and interface slopes reads

$$\frac{\partial h}{\partial t} = \Delta \{ -\Delta h - \mathcal{H}[h] + \mathcal{H}_i[h_i] + a(\bar{h})(h - h_i) \} + F \quad (5)$$

with the amplitude of the wetting term $a(\bar{h}) = c_w e^{-\bar{h}/\delta_w} / \delta_w^2$.

For a given film thickness \bar{h} on a flat substrate, a single mode modulation of the film surface $e^{i\mathbf{k}\cdot\mathbf{r}}$ grows as $e^{\sigma t}$ with the growth rate

$$\sigma(\mathbf{k}; \bar{h}) = -a(\bar{h})\mathbf{k}^2 + |\mathbf{k}|^3 - \mathbf{k}^4 \quad (6)$$

The typical $|\mathbf{k}|^3 - \mathbf{k}^4$ spectrum corresponds to the usual ATG instability which is hindered by the $-\mathbf{k}^2$ wetting term, as wetting favors the surface to follow the pattern shape. Below a given thickness h_c , σ is negative for every \mathbf{k} and the instability is suppressed due to wetting interactions [27], as usual in the Stransky–Krastanov growth mode. On the contrary, above h_c , the instability grows and we define for convenience $k_{ATG} = 3/4$ as the wave-vector which maximizes the ATG growth rate when no wetting interactions are at work, and which defines the typical length scale of the ATG instability. The influence of the forcing terms in Eq. (5) on the morphological evolution at constant thickness \bar{h} was analyzed in Ref. [25] where we described the kinetic phase diagram of the instability: Depending on the substrate wavelength, film thickness and annealing time, the surface geometry was found either to follow exactly the pattern, to follow the pattern shape but with an anti-coincidence geometry, or to merely develop the instability typical geometry quite independently of the pattern.

In order to depict growing films and the influence of the growth kinetics, we now consider a two-step growth mode, where the film is first grown at constant deposition flux before annealing occurs, see Fig. 5. The film evolution is now explicitly function of the film thickness (\bar{h}) which depends on time. During the first step $\bar{h}(t) = h_c + Ft$, while it is constant during annealing. We do not consider the dynamics below the critical height where no evolution occurs because of strong enough wetting interactions. Once a given thickness is reached, that we choose in most cases equal to 20 monolayers (ML) for practical reasons, annealing is performed at constant thickness $\bar{h}(t) = cst$. The evolution equation at linear order (5) can be solved analytically, and one finds

$$h(\mathbf{k}, t) = h_0(\mathbf{k}) e^{\sigma_k^*(t)t} + \delta(\mathbf{k}) F t + h_i(\mathbf{k}) e^{\sigma_k^*(t)t} \times \dots \times \int_0^t dt' [\mathbf{k}^2 \delta\gamma_h''[\bar{h}(t')] - |\mathbf{k}|^3 e^{-|\mathbf{k}|\bar{h}(t')}] e^{-\sigma_k^*(t')t'} \quad (7)$$

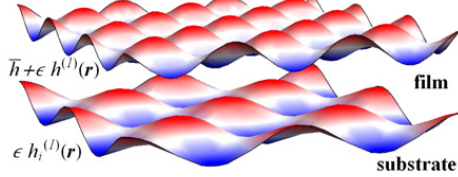


Fig. 1. (Color online.) Geometry of a film deposited on a patterned substrate with an egg-carton shape.

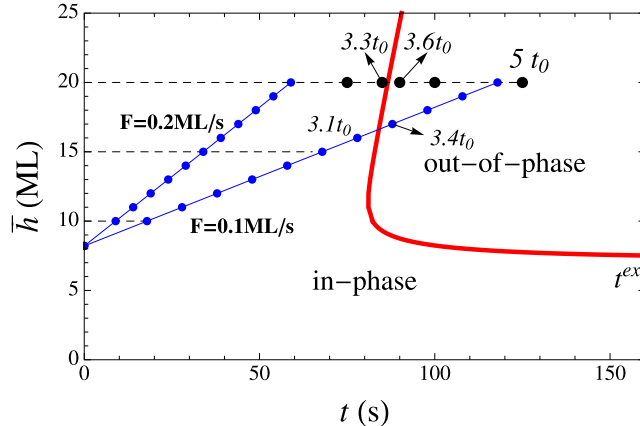


Fig. 2. (Color online.) Kinetic phase diagram for $k_i = k_{\text{ATG}}$. The red line t^{ex} characterizes the time when the instability skips from a configuration parallel to the pattern but in-phase with it to a configuration out-of-phase. The blue lines with dots show the film thickness evolution under consideration related to deposition fluxes $F = 0.1 \text{ ML/s}$ and $F = 0.2 \text{ ML/s}$ respectively. The blue points refer to the times corresponding to the deposition of each monolayer from h_c up to 20 ML, and characterize the line scans shown in Figs. 3 and 4. The black points on the horizontal line refer to the different times during annealing also shown in Figs. 3 and 4.

where $h_0(\mathbf{k})$ is the initial condition $h(\mathbf{r}, t = 0)$ in Fourier space, while we defined the time-average growth rate $\sigma_k^*(t) = \frac{1}{t} \int_0^t dt' \sigma[\mathbf{k}; \bar{h}(t')] \delta \gamma_h''$ as the second derivative of $\gamma(h)$ with respect to h . Eq. (7) shows that the film evolution is dictated firstly by a term linked to the initial condition h_0 which enforces a classic ATG instability dynamics. On the other hand, the term linked to h_i favors the film surface to follow the pattern geometry, in-phase if its amplitude is positive, or out-of-phase otherwise.

3. Results and discussion

In the following, we consider a substrate which displays a typical egg-carton shape, see Fig. 1, with a wave-vector modulus k_i ,

$$h_i(\mathbf{r}) = \epsilon [\cos(k_i x) + \cos(k_i y)] \quad (8)$$

where ϵ is a small parameter which ensures the small-slope approximation. When $\bar{h} < h_c$, the instability does not occur and wetting interactions enforce a surface which follows the pattern geometry. We compute the evolution after the thickness h_c and choose for the initial condition

$$h_0(\mathbf{r}) = h_c + h_i(\mathbf{r}) + \mathcal{R} \quad (9)$$

where \mathcal{R} is a white noise which describes the intrinsic deposition noise and substrate roughness that we choose to correspond to a roughness of 1 ML [25]. We perform a numerical computation of Eq. (7) using a decomposition on the Fourier modes, with the parameters appropriate for a $\text{Si}_{0.75}\text{Ge}_{0.25}$ film on a Si substrate, $c_w = 0.09$, $\delta_w = 1 \text{ ML}$ while $l_0 = 27 \text{ nm}$ [28]. At the working temperature $T = 700^\circ\text{C}$, the instability time scale is $t_0 = 25 \text{ s}$. These parameters and initial condition (9) correspond to the system under study in Ref. [25]. It was shown in this reference that there exists a typical time $t^{\text{ex}}(k_i; h)$ for which the surface morphology skips during annealing from two geometries parallel to the pattern but either in- or out-of-phase, through a nearly flat configuration in between (even when the growth rate of the k_i mode is positive).

We first consider the simplest case $k_i = k_{\text{ATG}}$ where a single characteristic wavelength occurs and where the pattern influence is maximal. We plot in Fig. 2, the film thickness evolution for two different fluxes together with the t^{ex} line which results from the annealing analysis. We choose a film thickness of 20 ML while $F = 0.2 \text{ ML/s}$ for which growth occurs mainly in the in-phase region of the annealing phase diagram, and $F = 0.1 \text{ ML/s}$, for which growth is still acting at t^{ex} . Line scans of the corresponding surface geometries at different times are plotted in Figs. 3 and 4. For the time under investigation, the surface geometry is mainly dictated by the pattern shape. It skips from an in-phase configuration to an out-of-phase one roughly at the same time t^{ex} compared to the annealing case. For this case, self-organization is found to

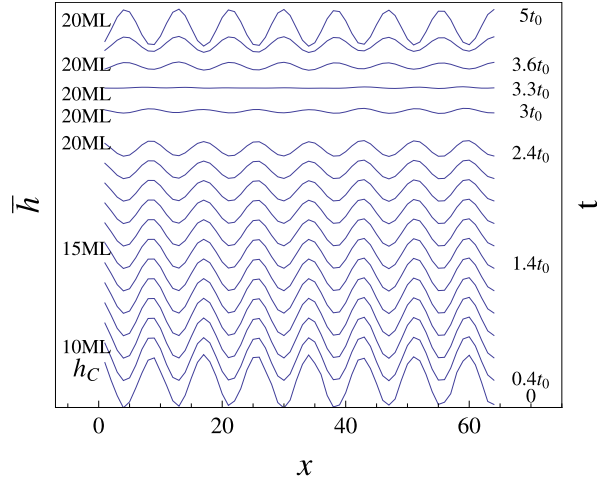


Fig. 3. (Color online.) Line scan of the surface geometry at each monolayer from initial thickness up to 20 ML during deposition and subsequent annealing, with $k_i = k_{\text{ATG}}$ and $F = 0.2 \text{ ML/s}$.

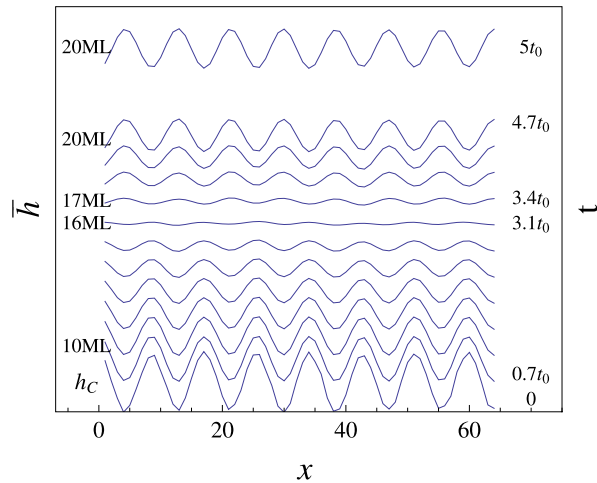


Fig. 4. (Color online.) Same characteristics as in Fig. 3 but with $F = 0.1 \text{ ML/s}$. Note the change from in-phase to out-of-phase as indicated by arrows.

be perfectly controlled by the influence of the pattern with either a localization on top (initially) or in the bottom (at large time) of the pattern depending mainly on the growth duration (either growth or annealing).

We now consider the case $k_i = \frac{1}{2}k_{\text{ATG}}$, where the system is ruled by two different characteristic length scales. In this case, the dynamics results from the competition between the growth of the k_i mode, which favors a change from an in-phase to an out-of-phase configuration, and the growth of the k_{ATG} mode, which favors a typical ATG instability morphology. This instability is characterized by a moderate spatial order in real space and a ring of maxima in Fourier space. In the annealing case, beside the t^{ex} line, an extra t^{max} line characterizes the full development of the instability at k_{ATG} , see the upper black line in Fig. 5. The time t^{max} is defined in Fourier space by the fact that the spectrum $|h(\mathbf{k})|^2$ at k_{ATG} is larger than the spectrum at k_i [25]. Two growth scenarios are investigated at two different fluxes, $F = 0.1$ and 0.01 ML/s , see Fig. 5. The former corresponds nearly to the annealing case where deposition occurs quickly before any evolution occurs, while in the latter case, the surface evolution occurs already during deposition. For $F = 0.1 \text{ ML/s}$, the t^{ex} line is still relevant to characterize the first vanishing of the amplitude of the k_i mode prior to its phase shift, but the surface geometry for this time gets clearly an extra noisy modulation due to the growth of the ‘classic’ k_{ATG} mode. Similarly, for $F = 0.01 \text{ ML/s}$, the vanishing of the amplitude of the k_i mode is still well described by the t^{ex} line, but the subsequent growth is also clearly modified by the k_{ATG} mode. We plot in Fig. 8(a) the full geometry of the film after the shift from the in-phase to the out-of-phase geometry. The film clearly gets some noise corresponding to the k_{ATG} mode but the geometry enforced by the pattern is still clearly visible. In addition, when the deposition time exceeds the time t^{max} , the ‘classic’ instability is again fully developed, see Figs. 5 and 8(b), and overcomes the pattern mode, as seen in Fourier space in Fig. 9.

These findings put emphasis on the importance to consider a dynamical approach to investigate such structures. Minimization of energy would lead, when no wetting interactions are at work, to a geometry where the film is out-of-phase relatively to the substrate [20]. When wetting interactions are included, an in-phase configuration would be stable for thin enough films, while the out-of-phase one is again stable above a given thickness [25]. Here, we find that either states can be found depending on the time used to grow the film, with a transition from the in-phase to the elastic energy minimizing

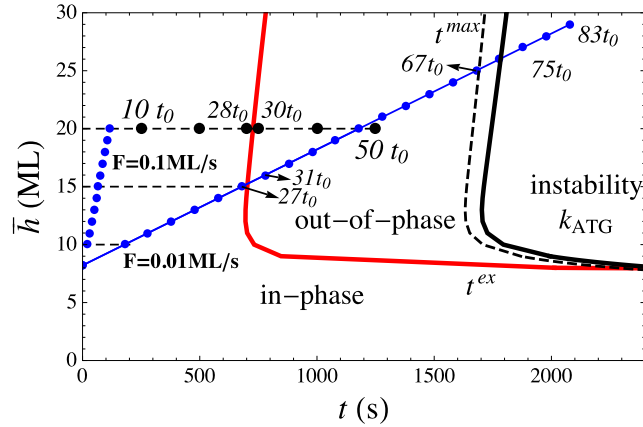


Fig. 5. (Color online.) Same notation as in Fig. 2 but for $k_i = \frac{1}{2}k_{\text{ATG}}$, and with deposition fluxes $F = 0.1$ and 0.01 ML/s corresponding respectively to the line scans in Figs. 6 and 7. The extra upper black line, referred to as the t^{\max} line in the text, delimits the region where the instability mode k_{ATG} is stronger than the k_i one. The dash line corresponds to the t^{\max} line on a stripe pattern, see Fig. 10, as discussed in Appendix A.

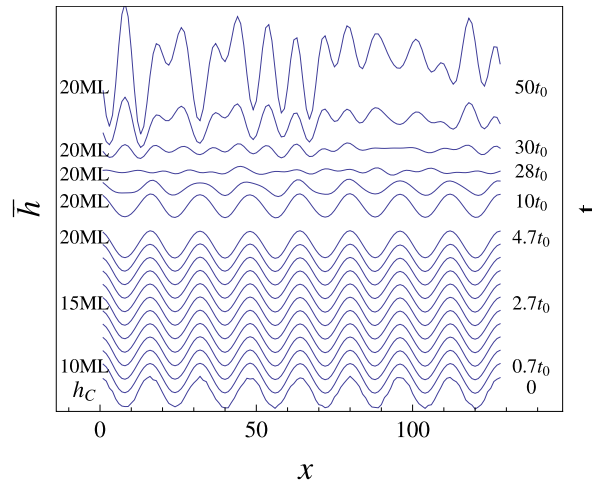


Fig. 6. (Color online.) Line scan of the surface geometry at each monolayer from initial thickness up to 20 ML during deposition and subsequent annealing, with $k_i = \frac{1}{2}k_{\text{ATG}}$ and $F = 0.1$ ML/s.

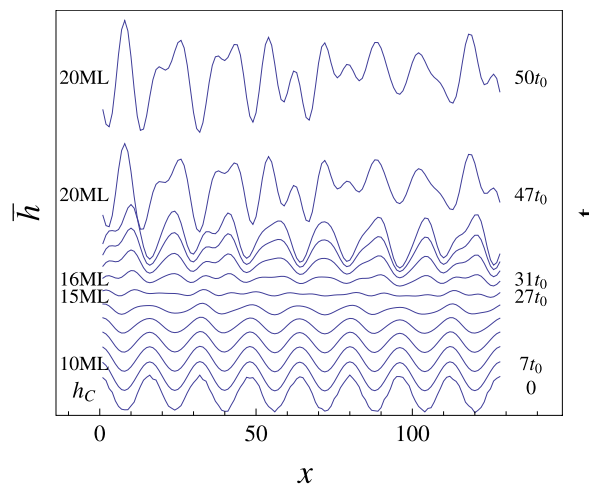


Fig. 7. (Color online.) Same characteristics as in Fig. 6 but with $F = 0.01$ ML/s.

out-of-phase geometry. Moreover, an instability with a spectrum similar to the flat substrate may be observed for a large enough deposition time. The geometry resulting from the instability defines the first stage on which quantum dots subsequently grow. Even though a systematic and explanatory comparison cannot be drawn between a simple linear analysis and

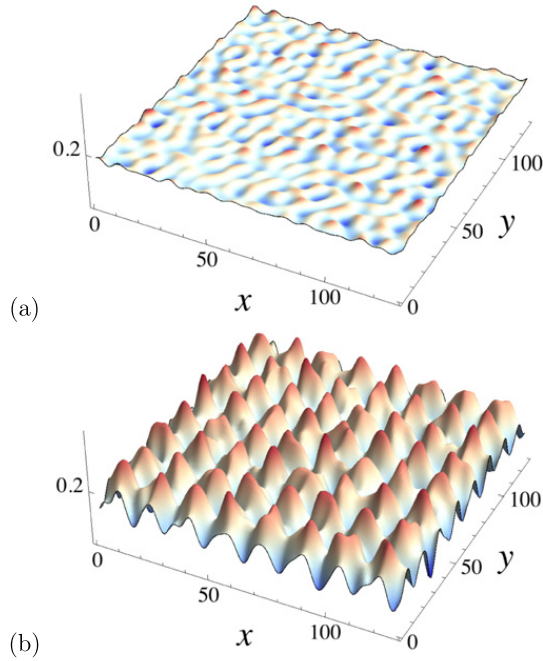


Fig. 8. (Color online.) Surface geometry with $k_i = \frac{1}{2}k_{\text{ATG}}$ and $F = 0.01$ ML/s corresponding to: (a) the time when the pattern wave-vector mode vanishes (even when it has a positive growth rate) in order to allow a shift from an in-phase to an out-of-phase configuration with respect to the pattern (corresponding to a 15 ML thick film); (b) a time after the phase shift where the instability corrugation is superimposed on an out-of-phase configuration (corresponding to a 20 ML thick film).

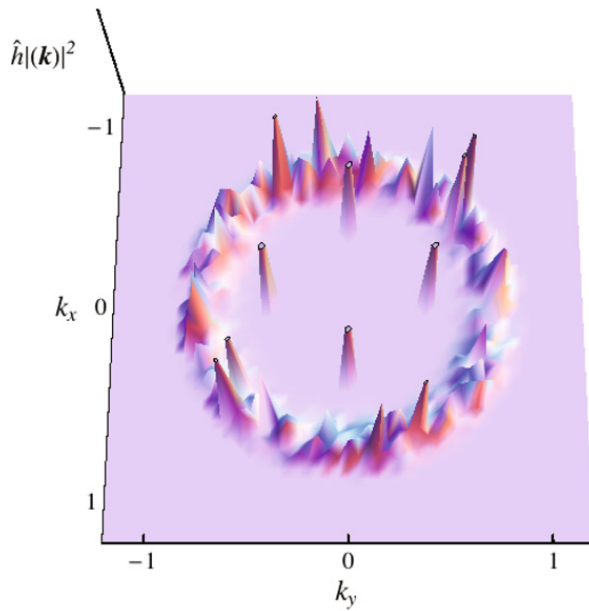


Fig. 9. (Color online.) Spectrum of the surface morphology for 25 ML deposited layers ($t = 67t_0$) for $k_i = \frac{1}{2}k_{\text{ATG}}$ and $F = 0.01$ ML/s, see the kinetic phase diagram of Fig. 5. The ring corresponds to the ‘classic’ spectrum of the ATG instability while the four peaks correspond to the pattern modes.

experiments, we believe that the kinetic phase diagram that we have exhibited gives some hints on the parameters relevant during growth and defines the basis of future work on the full non-linear regime.

4. Conclusion

We study here the dynamics of the morphological instability of a strained film on a patterned substrate. We solve the evolution equation during growth resulting from the continuum description of surface diffusion induced by elastic relaxation, surface energy and wetting interactions. We investigate the influence of the deposition flux on the initial stages of the instability in the linear approximation, and compare our findings with the results of the instability during annealing. For a given flux, we find different states (a configuration equal to the substrate geometry but either in-phase or out-of-phase, a ‘classical’ ATG instability-like morphology, etc.) depending on the time, pattern wavelength and film thickness. We study

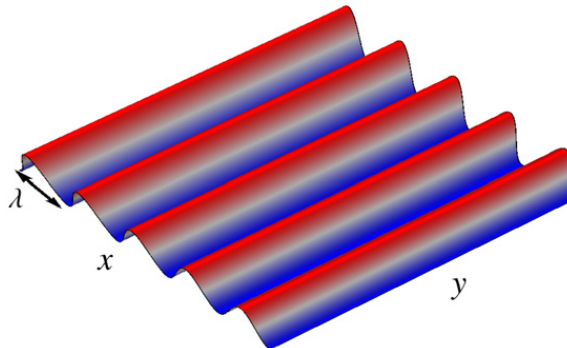


Fig. 10. (Color online.) Geometry of a 1D stripe pattern.

different growth scenarios where we deposit a given thickness but with different deposition flux and total duration of growth and annealing. We find that the kinetic phase diagram found analytically in the annealing case describes well the film configuration for a flux appropriate to describe usual growth conditions. In addition, as described in [Appendix A](#), we also find that this kinetic phase diagram also applies to describe the film geometry in the case of a 1D stripe pattern, and is therefore likely to be relevant in many different geometries and growth scenarios. Further investigation of the fully developed island regime will require a non-linear analysis. It was already pointed out that the translational symmetry-breaking in the growth direction due to wetting interactions, enforces a non-trivial dependence on the deposition flux which leads, on a flat substrate, to different non-linear regimes [29]. Extension of the latter analysis to the patterned case, where an extra symmetry-breaking arises from the elastic interactions, is currently under investigation.

Appendix A. 1D stripe pattern

We investigate here the influence of the pattern geometry by looking at a 1D pattern, see Fig. 10, where the film/substrate interface is basically

$$h_i(\mathbf{r}) = \epsilon \cos(k_i x) \quad (10)$$

This geometry mimics stripe patterns which are also often studied in experiments. The evolution equation during annealing at linear order is merely

$$h(\mathbf{k}, t) = h^0(\mathbf{k}) e^{\sigma t} - C(k, \bar{h}) h_i(\mathbf{k}) (e^{\sigma t} - 1) \quad (11)$$

with the surface initial condition $h^0(\mathbf{k})$ and the coefficient of the inhomogeneous solution $C(k, \bar{h})$ given in Ref. [25]. The kinetic phase diagram for both the egg-carton and stripe shapes during annealing are plotted in Figs. 2 and 5. The time for the phase exchange $t^{\text{ex}}(k_i, \bar{h})$ is the same for both patterns as it is defined in both cases by $t^{\text{ex}}(k_i, \bar{h}) = \ln[C/(C - 1)]/\sigma$. However, the t^{max} line, which delimits when the ‘classic’ instability overcomes the pattern influence, differs slightly for these two pattern shapes, see Fig. 5. The t^{max} line is indeed slightly shifted for smaller times for the stripe pattern, as the amplitude of the k_i mode is indeed smaller in this case compared to the egg-carton shape.

References

- [1] B. Voigtänder, Fundamental processes in Si/Si and Ge/Si epitaxy studied by scanning tunneling microscopy during growth, *Surf. Sci. Rep.* 43 (2001) 127.
- [2] J. Stangl, V. Holý, G. Bauer, Structural properties of self-organized semiconductor nanostructures, *Rev. Mod. Phys.* 76 (2004) 725.
- [3] I. Berbezier, A. Ronda, SiGe nanostructures, *Surf. Sci. Rep.* 64 (2009) 47.
- [4] D.S.L. Mui, D. Leonard, L.A. Coldren, P.M. Petroff, Surface migration induced self-aligned InAs islands grown by molecular beam epitaxy, *Appl. Phys. Lett.* 66 (1995) 1620.
- [5] W. Seifert, N. Carlsson, A. Petersson, L.E. Wernersson, L. Samuelson, Alignment of InP Stranski-Krastanow dots by growth on patterned GaAs/GaInP surfaces, *Appl. Phys. Lett.* 68 (1996) 1684.
- [6] T. Ishikawa, S. Kohmoto, K. Asakawa, Site control of self-organized InAs dots on GaAs substrates by in situ electron-beam lithography and molecular-beam epitaxy, *Appl. Phys. Lett.* 73 (1998) 1712.
- [7] A. Konkar, A. Madhukar, P. Chen, Stress-engineered spatially selective self-assembly of strained InAs quantum dots on nonplanar patterned GaAs(001) substrates, *Appl. Phys. Lett.* 72 (1998) 220.
- [8] E.S. Kim, N. Usami, Y. Shiraki, Selective epitaxial growth of dot structures on patterned Si substrates by gas source molecular beam epitaxy, *Semicond. Sci. Technol.* 14 (1999) 257.
- [9] P.D. Szkutnik, A. Sgarlata, A. Balzarotti, N. Motta, A. Ronda, I. Berbezier, Early stage of Ge growth on Si(001) vicinal surfaces with an 8° miscut along [110], *Phys. Rev. B* 75 (2007) 033305.
- [10] T.I. Kamins, R.S. Williams, Lithographic positioning of self-assembled Ge islands on Si(001), *Appl. Phys. Lett.* 71 (1997) 1201.
- [11] G. Jin, J.L. Liu, S.G. Thomas, Y.H. Luo, K.L. Wang, B.-Y. Nguyen, Controlled arrangement of self-organized Ge islands on patterned Si(001) substrates, *Appl. Phys. Lett.* 75 (1999) 2752.
- [12] T. Kitajima, B. Liu, S.R. Leone, Two-dimensional periodic alignment of self-assembled Ge islands on patterned Si(001) surfaces, *Appl. Phys. Lett.* 80 (2002) 497.

- [13] B. Yang, F. Liu, M.G. Lagally, Local strain-mediated chemical potential control of quantum dot self-organization in heteroepitaxy, *Phys. Rev. Lett.* 92 (2004) 025502.
- [14] Z. Zhong, W. Schröger, F. Schäffler, G. Bauer, G. Vastola, F. Montalenti, L. Miglio, Delayed plastic relaxation on patterned Si substrates: Coherent SiGe pyramids with dominant {111} facets, *Phys. Rev. Lett.* 98 (2007) 176102.
- [15] L. Vescan, T. Stoica, B. Hollander, A. Nassiopoulou, A. Olzierski, I. Raptis, E. Sutter, Self-assembling of Ge on finite Si(001) areas comparable with the island size, *Appl. Phys. Lett.* 82 (2003) 3517.
- [16] Z. Zhong, A. Halilovic, M. Muhlberger, F. Schäffler, G. Bauer, Ge island formation on stripe-patterned Si(001) substrates, *Appl. Phys. Lett.* 82 (2003) 445.
- [17] Z. Zhong, A. Halilovic, T. Fromherz, F. Schäffler, G. Bauer, Two-dimensional periodic positioning of self-assembled Ge islands on prepatterned Si(001) substrates, *Appl. Phys. Lett.* 82 (2003) 4779.
- [18] B. Sanduijav, D. Matei, G. Chen, G. Springholz, Shape transitions and island nucleation for Si/Ge molecular beam epitaxy on stripe-patterned Si(001) substrate, *Phys. Rev. B* 80 (2009) 125329.
- [19] A. Pascale, I. Berbezier, A. Ronda, P.C. Kelires, Self-assembly and ordering mechanisms of Ge islands on prepatterned Si(001), *Phys. Rev. B* 77 (2008) 075311.
- [20] H. Wang, Y. Zhang, F. Liu, Enhanced growth instability of strained film on wavy substrate, *J. Appl. Phys.* 104 (2008) 054301.
- [21] H. Hu, H.J. Gao, F. Liu, Theory of directed nucleation of strained islands on patterned substrates, *Phys. Rev. Lett.* 101 (2008) 216102.
- [22] P. Sutter, M.G. Lagally, Nucleationless three-dimensional island formation in low-misfit heteroepitaxy, *Phys. Rev. Lett.* 84 (2000) 4637.
- [23] R.J. Asaro, W.A. Tiller, Interface morphology development during stress-corrosion cracking: Part 1. Via surface diffusion, *Metall. Trans.* 3 (1972) 1789.
- [24] M.A. Grinfeld, Instability of the separation boundary between a nonhydrostatically stressed elastic body and a melt, *Sov. Phys. Dokl.* 31 (1986) 831.
- [25] X. Xu, J. Aqua, T. Frisch, Growth kinetics in a strained crystal film on a wavy patterned substrate, *J. Phys.: Condens. Matter* 24 (2012) 045002.
- [26] G.-H. Lu, F. Liu, Towards quantitative understanding of formation and stability of Ge hut islands on Si(001), *Phys. Rev. Lett.* 94 (2005) 176103.
- [27] J.-N. Aqua, T. Frisch, A. Verga, Nonlinear evolution of a morphological instability in a strained epitaxial film, *Phys. Rev. B* 76 (2007) 165319.
- [28] J.-N. Aqua, T. Frisch, Influence of surface energy anisotropy on the dynamics of quantum dot growth, *Phys. Rev. B* 82 (2010) 085322.
- [29] J.-N. Aqua, T. Frisch, A. Verga, Ordering of strained islands during surface growth, *Phys. Rev. E* 81 (2010) 021605.

Chapter 4

Isotropic nonlinear evolution of the Asaro-Tiller-Grindel'd instability



Quantum dot growth on a stripe-pattern

X. Xu, J.-N. Aqua *

Institut des Nanosciences de Paris, Université Pierre et Marie Curie, Paris 6, CNRS UMR 7588, 4 place Jussieu, 75252 Paris, France

ARTICLE INFO

Available online xxxx

Keywords:
 Nanostructures
 Pattern
 Island growth
 Epitaxy
 Elasticity

ABSTRACT

We study the development of the Asaro-Tiller-Grinfel'd instability on a thin strained film on top of a stripe-patterned substrate and the subsequent growth of self-organized quantum dots. We use a continuum model describing the evolution equation enforced by surface diffusion. We compute the elastic energy up to the first non-linear order and investigate the long time dynamics which describes the dot growth. We find different island locations depending on the substrate wavelength and thickness. As found in experiments, the instability long-time dynamics leads to islands located either on top or in the bottom of the pattern.

© 2013 Published by Elsevier B.V.

1. Introduction

The growth of self-organized islands on a patterned substrate was subject to intense experimental and theoretical works due to their link with application and the fundamental issues concerning growth mechanisms that they address [1–3]. The underlying goal is to achieve a given spatial order and a narrow size distribution which are both limited on a flat substrate, see e.g. [4]. This control is clearly important if one wants to achieve good electrical and optical properties of dots for their potential use in devices.

Of particular interest is the growth of islands on a stripe-patterned substrate. This geometry which is the simplest one may think of, allows to check the control and understanding of island growth on a pattern. However, on the experimental front, no clear scenario emerges as regards to the preferential location of the dots, even in the paradigmatic SiGe systems. Perfectly aligned and regularly spaced one dimensional (1D) arrays of Ge islands appeared on the stripe mesas in [5]. In this work, the pattern was obtained by photolithography and the separation between stripes was 100 nm, similar to the pattern height. This location was also obtained in [6] on larger and sparser stripes. In a slightly different but similar geometry, islands were also found to decorate the top of the undulation resulting from the deposition of a $\text{Si}_{1-x}\text{Ge}_x$ template layer on a 10° off $\text{Si}(001)$ substrate [2]. On the other hand, islands were shown to nucleate in [7] rather on the side of a pattern resulting from holographic lithography and reactive-ion etching, with a period of 500 nm and a height of 100 nm. Finally, in a different but comparable geometry, islands were conversely found in [8] in the bottom of a pit-patterned substrate.

In order to shed some light on the basic mechanisms at work in these systems, we study the evolution of the Asaro-Tiller-Grinfel'd (ATG) instability [9,10] on a pattern. This instability is known to be at work in low-strained SiGe films on Si and corresponds to a nucleationless evolution [11] which finally leads to islands. It must be distinguished with the nucleation of dots in the 2D–3D transition observed in higher strained $\text{Si}_{1-x}\text{Ge}_x$ films with a higher Ge content, see e.g. [12]. In order to study the instability, we use a basic continuum model which accounts for elasticity, wetting interactions and surface energy. It describes the evolution of the surface morphology as dictated by mass conservation associated with surface diffusion during annealing. We investigate the formation of islands by looking at the long-time evolution of the instability thanks to its non-linear analysis. We find different locations of the dots depending on the pattern wavelength and mean film height. Both parameters rule the external force resulting from the patterned film/substrate interface, especially its amplitude and frequency with respect to the instability characteristic wavelength.

2. Continuum model and non-linear analysis

We use a continuum description relevant to describe the instability dynamics on large scales. We first consider the diffusion equation during annealing

$$\frac{\partial h}{\partial t} = D \Delta_s \mu, \quad (1)$$

where $z = h(r,t)$ is the surface height at time t of the $r = (x,y)$ column, while D is an effective surface diffusion coefficient, Δ_s , the surface Laplacian, and μ , the chemical potential on the surface [13]. Different effects may be accounted for by adding extra terms to the basic chemical potential $\mu = \gamma\kappa + \mathcal{E}^{el}$, where \mathcal{E}^{el} is the elastic energy

* Corresponding author.

E-mail address: aqua@insp.jussieu.fr (J.-N. Aqua).

density on the surface, γ , the surface energy, and κ , the curvature $\kappa = -(h_{xx} + h_{yy}) + \dots$ at first order in the surface slope. Wetting interactions between the film and the substrate may be accounted for by an explicit dependence of the surface energy on the film thickness [14,15]. The film/substrate interface is patterned and is defined by $z = h_-(r)$, so that we write this dependence as

$$\gamma = \gamma[h(r) - h_-(r)], \quad (2)$$

where we use an exponentially decaying decrease in $\gamma(h)$ [16]. This dependence enforces an additional wetting potential in the chemical potential which merely reads $\Omega_{\text{eff}}^{\text{dy}}$, where Ω is the atomic volume.

In addition to the wetting interactions, the patterned interface also generates buried elastic dipoles which create an elastic field throughout the system. It may be computed by solving the mechanical equilibrium Navier-Cauchy equations $\partial_i \sigma_{ij} = 0$ in the film and in the substrate. An elastic stress is generated by the coherence of their interface and the lattice misfit between them, $m = 1 - a_f/a_s$, with the film and substrate lattice parameters a_f and a_s . For simplicity, we consider identical elastic properties for the film and substrate. The continuity of forces and displacements at the interface allows us to compute explicitly the solution in the small slope approximation where $|\nabla h_-|$ is supposed to be small. Finally, the film surface is also supposed to be free of stress, which also allows us to compute the full solution for the displacements in the second small slope approximation where $|\nabla h|$ is small. With this solution in hand, one can compute the elastic energy density on the surface $\mathcal{E}^{\text{el}} = \mathcal{E}_0 + \mathcal{E}_1 + \mathcal{E}_2 + \dots$ up to the first non-linear order. At zeroth order in the film and interface slopes, it corresponds to the flat film elastic energy density $\mathcal{E}_0 = Ym^2/(1-\nu)$, where Y is the film Young modulus and ν , its Poisson ratio. At first order, it is given by [13]

$$\frac{\mathcal{E}_1}{2(1+\nu)\mathcal{E}_0} = -\mathcal{H}_{ii}[h] + \mathcal{B}\{\mathcal{H}_{ii}[h_-]\}, \quad (3)$$

with summation over repeated indices and with the generalized Hilbert transforms defined in Fourier space [17]

$$\mathcal{H}_{ij}[h](k) = \frac{k_i k_j}{|k|} \mathcal{F}[h](k), \quad (4)$$

where i, j are either x or y . Moreover, the elastic field created by the buried elastic dipoles at the film/substrate interface is exponentially damped in the growth direction, which is described by the operator

$$\mathcal{B}[h](k) = e^{-|k|\bar{h}} \mathcal{F}[h](k), \quad (5)$$

with the mean film height $\bar{h} = \langle h \rangle - \langle h_- \rangle$. Finally, considering a 1D pattern parallel to the y -direction $z = h_-(x)$, see Fig. 1, we also computed the elastic energy up to the second order, which can be decomposed in three parts $\mathcal{E}_2 = \mathcal{E}_2^{++} + \mathcal{E}_2^{+-} + \mathcal{E}_2^{--}$, where the first contribution depends only on the upper surface height h contrary to

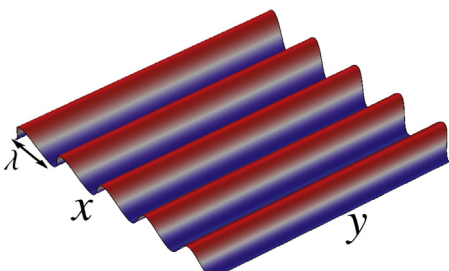


Fig. 1. 1D pattern on which the Asaro-Tiller-Grinfeld instability develops.

the last one which depends only on the interface h_- , while the second one is an interference term depending on both heights. The first contribution which involves only the film height naturally coincides with the second order computed for a flat film/substrate interface [18]

$$\frac{\mathcal{E}_2^{++}}{2\mathcal{E}_0(1+\nu)} = 2h\Delta h + |\nabla h|^2 + \mathcal{H}_{ij}[h]\theta_{ijkl}\mathcal{H}_{kl}[h] + 2\mathcal{H}_{ij}[h]\theta_{ijkl}\mathcal{H}_{kl}[h], \quad (6)$$

where $\theta_{ijj} = 1$ for $i, j = x, y$, $\theta_{iji} = -\theta_{iji} = \nu$ for $i \neq j$ while it vanishes otherwise. The new contributions correspond first to the external field associated with the buried dipoles of the film/substrate interface, which merely reads

$$\frac{\mathcal{E}_2^{--}}{2\mathcal{E}_0(1+\nu)} = -\mathcal{B}\left\{ \left| \frac{\partial h_-}{\partial x} \right|^2 + h_- \frac{\partial^2 h_-}{\partial x^2} \right\} + \mathcal{B}[\mathcal{H}_{xx}[h_-]]^2, \quad (7)$$

while the cross term which describes the interference between the dipoles of the film surface and the dipoles of the interface is

$$\begin{aligned} \frac{\mathcal{E}_2^{+-}}{2\mathcal{E}_0(1+\nu)} = & -h\mathcal{B}\left[\frac{\partial^2 h_-}{\partial x^2} \right] - 2\mathcal{H}_{xx}[h]\mathcal{B}\mathcal{H}_{xx}[h_-] - 2\nu\mathcal{H}_{yy}[h]\mathcal{B}\mathcal{H}_{xx}[h_-] \\ & - 2\mathcal{H}_{xx}\{h\mathcal{B}\mathcal{H}_{xx}[h_-]\} - 2\nu\mathcal{H}_{yy}\{h\mathcal{B}\mathcal{H}_{xx}[h_-]\}. \end{aligned} \quad (8)$$

3. Evolution

The characteristic length and time scales are set by the instability driving forces and are given by $l_0 = \gamma_f/2(1+\nu)\mathcal{E}_0$ and $t_0 = l_0^4/D\gamma_f$, where γ_f is the film characteristic surface energy. For a typical Si_{0.75}Ge_{0.25} film on a Si substrate, where the misfit strain is 1%, these are of the order of 27 nm and 25 s [18]. As regards the wetting effect, we consider a smooth exponentially decaying surface energy $\gamma(h) = \gamma_f[1 + c_w \exp(-h/\delta_w)]$, where c_w is extrapolated to 0.1, while δ_w is taken as one lattice parameter [18].

The dynamics associated with the evolution Eq. (1) at linear order corresponds to the early time dynamics of the instability. In the case of a flat substrate and without wetting interactions, a perturbation with a wave-vector vk grows exponentially with time with the ATG growth rate $\sigma = |k|^3 - k^4$ in dimensionless units defined with l_0 and t_0 [9,10]. This growth rate displays a maximum for a given $|k|$, which allows to define the instability characteristic length scale λ_{ATG} . When wetting interactions are acting, an extra $-k^2 e^{-h/\delta_w}$ term is present and enforces a negative σ for $h < h_c$, below which a thin film remains stable and does not develop the morphological instability. The evolution at linear order with the initial condition (9) and the pattern influence (Eq. (3)) was analyzed in Ref. [13] for a similar but slightly different 2D egg-carton shape. Kinetic phase diagrams were exhibited, which describe the surface geometry as a function of the pattern wavelength λ , the film thickness \bar{h} and the duration t of the evolution. Three main configurations were found. In the first two, the film displays mainly the pattern shape but is either in-phase (the maxima of the film lie on top of the maxima of the substrate) or out-of-phase (the film and substrate maxima and minima lie on top of each other). A continuous transition from the initial in-phase to the energy-minimizing out-of-phase configurations was evidenced, which occurs by the vanishing of the film roughness in order to allow the phase shift even for a positive growth rate [13]. The last film geometry which may be found in the linear analysis, is associated with the 'classic' ATG instability shape, well-defined in Fourier space by a ring of maxima which correspond to the wave-vectors which maximize the linear growth rate. In this last case, the influence of the pattern may be quantified in Fourier space, but is hardly visible in real space.

To go beyond the initial linear evolution, we numerically solve the non-linear evolution Eq. (1) using a pseudo-spectral method devised to stiff non-linear partial differential equations [19]. We consider an

initial condition where the film follows the substrate shape with a small random noise

$$h(r, t = 0) = h_-(r) + \bar{h} + R(r), \quad (9)$$

where R is a white noise which corresponds to a 1 monolayer (ML) initial roughness. This initial condition corresponds to experiments where surface diffusion does not have time to occur much during the film deposition so that the instability occurs mainly during annealing, which is especially relevant for thin and low strained films. Moreover, we consider a 1D stripe-patterned substrate $h_-(r) = h_-(x)$, with a basic cosine shape

$$h_-(x) = A_- \cos(2\pi x/\lambda), \quad (10)$$

see Fig. 1. The amplitude A_- is chosen such as the small-slope approximation is fulfilled, i.e. $A_-/\lambda \ll 1$. In Fourier space, the choice of Eqs. (9) and (10) leads to an initial spectrum with a flat noise in addition to the predominant mode $2\pi/\lambda$ in the x direction. Hence, the pattern introduces two new parameters which dictate its shape, given e.g. by the amplitude A_- and wavelength λ . In the following, we set the amplitude A_- so that the small slope approximation is fulfilled ($A_-/\lambda \ll 1$) and we vary the pattern wavelength while the instability characteristic wavelength λ_{ATG} is kept fixed. In order to simplify the analysis, we consider here an isotropic surface energy leading to isotropic island shapes which, strictly speaking, restricts the validity of our results to the prepyramid regime where only roughly isotropic small islands are present [3]. For solving Eq. (8), we used the same parameters as [18].

3.1. Equal pattern and instability wavelengths $\lambda = \lambda_{\text{ATG}}$

We first consider the simplest case where the pattern wavelength is equal to the instability one. We plot in Fig. 2 the evolution corresponding to a deposited thickness $\bar{h} = 15.3$ ML above the critical height defining the quantum dot growth. In this geometry, we notice that the initial instability (Fig. 2a) is already out-of-phase compared to the substrate as its maxima lie on top of the substrate minima. In this case, it can be shown, see e.g. [20], that the elastic energy is minimized in this out-of-phase geometry. As a consequence, small islands arise in the first stage of the dot growth in the bottom of the pattern, lying on top of a wetting layer, see Fig. 2b) for an intermediate time $t = 1.3 \times 10^3$ s. These islands are rather perfectly aligned by the pattern and form lines of dots with a rather well-defined inter-island distance, see Fig. 2c). As time increases, Ostwald coarsening occurs by mass diffusion on the surface so that larger islands which relax the elastic stress more efficiently grow at the expense of the smallest ones, see e.g. [17]. This process induces correlations between different rows of islands and a modulation over two substrate periods is clearly visible where one period over two is partially depleted of islands, see Fig. 2d). On a larger time, see Fig. 2e), a non-interrupted coarsening acts among these rather isotropic islands similarly to the case of a flat substrate, and the spatial order disappears during this random process.

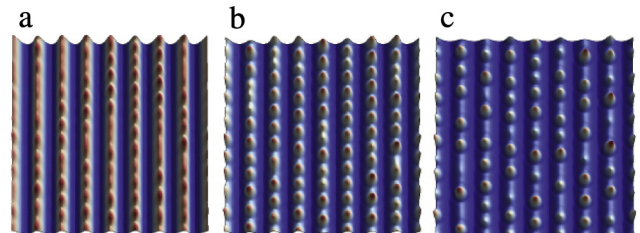


Fig. 3. Evolution of a 8.5 ML film for equal pattern and instability wavelengths $\lambda = 2\lambda_{\text{ATG}}$. The dimensionless time is 13, 22, 50 (i.e. 1.3, 2.2 and 5.0×10^3 s).

3.2. Case $\lambda = 2\lambda_{\text{ATG}}$

The previous system was characterized by a single characteristic length scale and we now turn to a priori more complex case with two different scales $\lambda = 2\lambda_{\text{ATG}}$. We plot in Figs. 3 and 4 the surface evolution for the thicknesses $\bar{h} = 8.5$ and 15.3 ML. In the first case, the deposited thickness is just above the critical thickness which is $h_c = 8.3$ ML with our parameters. The instability grows in phase with the pattern so that the first islands which grow are located on top of the pattern, see Fig. 3a). These seed islands lead to mature islands which are all located on top of the pattern, see Fig. 3b). In this case, the size dispersion is minimal and a relatively good spatial order is reached on top of the pattern. However, contrary to the case of equal wavelengths, island coarsens but remains at their upper position and no islands are created in the pattern valley. A crucial difference between the two systems is that when islands form on top of the pattern, there is not enough matter available in the valley to form new energy-minimizing islands (which would be of lower chemical potential and would drag matter from the upper islands) and matter concentrates and stays in the upper islands (which nevertheless relieves less efficiently the elastic energy). The film evolution thus follows states merely dictated by the growth kinetics. On larger time, Fig. 3c), the ordered configuration found in Fig. 3b) is destroyed by Ostwald coarsening where large islands on top of the pattern grow at the expense of the smallest ones.

In the case of a thicker film, $\bar{h} = 15.3$ ML, the instability grows faster. In this case, the first stage of the evolution is a phase exchange, where the instability shifts from its initial configuration where its maxima lie on top of the pattern ones, to a configuration where its maxima lie on top of the pattern minima, see Fig. 4a). This phase exchange was computed exactly in the linear regime and it does indeed correspond to small times for these parameters (film thickness and pattern wavelength). As a consequence, the first islands to grow arise in the pattern valleys, see Fig. 4b). Further coarsening leads to good spatial order and size dispersion where islands lie in line and with a given distance in the pattern, see Fig. 4c). Ostwald coarsening still occurs among these islands, see Fig. 4d) and e), and destroys the spatial ordering and leads to a lower size uniformity.

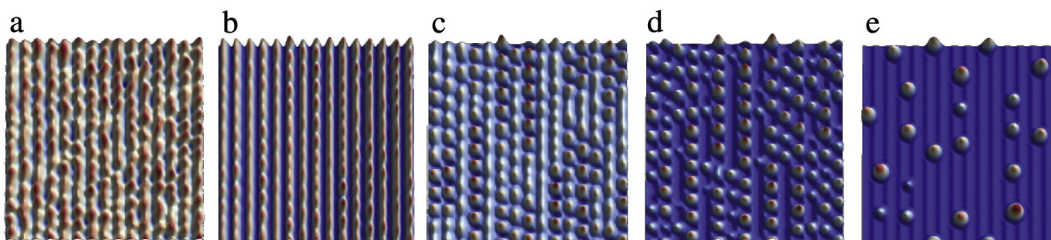


Fig. 2. Evolution of a 15.3 ML film for equal pattern and instability wavelengths $\lambda = \lambda_{\text{ATG}}$. The annealing time is 10, 13, 23, 50, 250 in dimensionless units (respectively 0.1, 1.3, 2.3, 5.0, and 25×10^3 s).

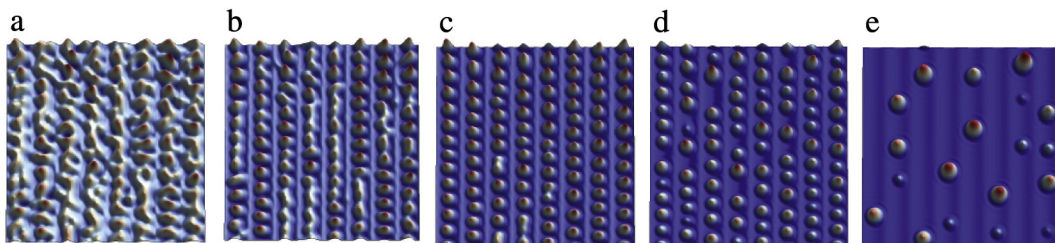


Fig. 4. Evolution of a 15.3 ML film for equal pattern and instability wavelengths $\lambda = 2\lambda_{ATG}$. The dimensionless time is 12, 16, 24, 60 and 250 (i.e. 1.2, 1.6, 2.4, 6.0, and 25×10^3 s).

3.3. Comparison

We find different island locations depending on the geometrical parameters: pattern wavelength and film thickness. In the case $\lambda = \lambda_{ATG}$ both for thin (not displayed here) and thick films, and $\lambda = 2\lambda_{ATG}$ for \bar{h} thick enough, islands arise only in the bottom of the stripes. On the contrary, for $\lambda = 2\lambda_{ATG}$ for \bar{h} thin enough, islands grow on top of the stripes. These different locations are correlated with the geometry of the initial instability which is the seed for the subsequent island growth. The location in the bottom occurs when the initial instability experienced a phase exchange with respect to the substrate, as already predicted by the linear analysis [13]. On the contrary, the location on the top occurs when the instability did not have time to exchange its phase compared to the pattern before the islands have arisen. This observation underlines the importance to describe the growth kinetics in order to precisely describe the island location which does not result from an equilibrium analysis. For the sake of completeness, we recall that in the high-strain regime where nucleation is at work, it was shown in [21] that strain relaxation favors the preferential nucleation in the bottom of a pit rather than on its top, whereas surface energy anisotropy does not favor one location compared to the other one.

4. Conclusion

We have studied the growth dynamics of quantum dots during annealing of a thin strained film on a patterned substrate. This dynamics describes the morphological instability enforced by surface diffusion and reminiscent of the Asaro-Tiller-Grinfel'd instability which leads to self-organized islands. We compute at the first non-linear order, the elastic energy created by a 1D stripe-patterned film/substrate interface. We solve numerically the evolution equation describing mass conservation during annealing. We find different island locations depending on the pattern wavelength compared to the ATG typical length scale, and on the film thickness. The islands are found to arise either on top or in

the bottom of the pattern. A good spatial order where islands gather in line may be found in some conditions. However, a non-interrupted coarsening occurs on a large enough time and leads to the disappearance of small islands to the benefit of the largest ones during annealing. This random process destroys the spatial order that was initially found, and a good spatial order is only achieved in a given range of annealing time. Further investigation to rationalize these findings and to study the influence of anisotropy on the coarsening and on the spatial organization is postponed for future work.

References

- [1] O.G. Schmidt, Lateral Alignment of Epitaxial Quantum Dots, Springer, 2007.
- [2] I. Berbezier, A. Ronda, *Surf. Sci. Rep.* 64 (2009) 47.
- [3] J.N. Aqua, I. Berbezier, L. Favre, T. Frisch, A. Ronda, *Phys. Rep.* 522 (2013) 59.
- [4] S. Miyamoto, O. Moutanabbir, E.E. Haller, K.M. Itoh, *Phys. Rev. B* 79 (2009) 165415.
- [5] G. Jin, J.L. Liu, S.G. Thomas, Y.H. Luo, K.L. Wang, B.-Y. Nguyen, *Appl. Phys. Lett.* 75 (1999) 2752.
- [6] B. Yang, F. Liu, M.G. Lagally, *Phys. Rev. Lett.* 92 (2004) 025502.
- [7] Z. Zhong, A. Halilovic, M. Muhlberger, F. Schaffler, G. Bauer, *Appl. Phys. Lett.* 82 (2003) 445.
- [8] Z. Zhong, W. Schwingen, F. Schäffler, G. Bauer, G. Vastola, F. Montalenti, L. Miglio, *Phys. Rev. Lett.* 98 (2007) 176102.
- [9] R.J. Asaro, W.A. Tiller, *Metall. Trans. 3* (1972) 1789.
- [10] M.A. Grinfeld, *Sov. Phys. Dokl.* (1986) 831.
- [11] P. Suttor, M.G. Lagally, *Phys. Rev. Lett.* 84 (2000) 4637.
- [12] C.-H. Lam, C.-K. Lee, L.M. Sander, *Phys. Rev. Lett.* 89 (2002) 216102.
- [13] X. Xu, J. Aqua, T. Frisch, *J. Phys. Condens. Matter.* 24 (2012) 045002.
- [14] C.-H. Chiu, H. Gao, in: S.P. Baker, et al., (Eds.), *Thin Films: Stresses and Mechanical Properties V*, MRS Symposia Proceedings No. 356, Materials Research Society, Pittsburgh, 1995, p. 33.
- [15] P. Müller, R. Kern, *Appl. Surf. Sci.* 102 (1996) 6.
- [16] G.-H. Lu, F. Liu, *Phys. Rev. Lett.* 94 (2005) 176103.
- [17] J.-N. Aqua, T. Frisch, A. Verga, *Phys. Rev. B* 76 (2007) 165319.
- [18] J.-N. Aqua, T. Frisch, *Phys. Rev. B* 82 (2010) 085322.
- [19] A.-K. Kassam, L.N. Trefethen, *SIAM J. Sci. Comput.* 26 (2005) 1214, <http://dx.doi.org/10.1137/S1064827502410633>.
- [20] H. Wang, Y. Zhang, F. Liu, *J. Appl. Phys.* 104 (2008) 054301.
- [21] H. Hu, H.J. Gao, F. Liu, *Phys. Rev. Lett.* 101 (2008) 216102.

Controlling self-organization of strained quantum dots

Xianbin Xu^{1,2} and Jean-Noël Aqua^{1,2}

¹UPMC Univ Paris 6, INSP, UMR 7588, 4 place Jussieu, 75252 Paris, France

²CNRS, INSP, UMR 7588, 4 place Jussieu, 75252 Paris, France

(Dated: June 6, 2013)

We devise a dynamical modelization of the growth of strained islands on a pattern. A morphological instability with a characteristic wavelength develops on a thin film in the presence of external forcing due to an underlying patterned interface with another wavelength. We find that islands can form in well-organized arrays located either in the peaks or valleys of the pattern depending on the film thickness and the ratio of the two characteristic wavelengths. These results are rationalized by a kinetic phase diagram and correlated with the morphology when the islands and the wetting layer grow. We find that the islands sizes are homogeneous when grown on appropriate patterns and their coarsening is significantly slowed down, in good agreement with experimental observations reported in the literature.

PACS numbers: 81.15.Hi, 68.35.Ct, 81.10.Aj, 46.70.Lk

The homogeneity and order of an assembly of nanostructures are crucial for their use in large scale electronic or optical systems, and challenge our understanding and control of the growth mechanisms at small scales. SiGe quantum dots grown in coherent epitaxy after a 2D-3D strain-relieving transition [1] exhibit strong size fluctuations related to their nucleation. By avoiding this stage, islands resulting from an instability with a long range order [2] are *a priori* good candidates for achieving uniform properties, but they also exhibited a poor homogeneity [3].

To reduce inhomogeneities, the growth of islands on morphologically patterned substrates has been extensively studied [4]. It may lead to uniform assemblies of well-ordered islands [5] but contradictory results are found under comparable conditions: Ge islands on Si(001) grew either on top or edge of the pattern [6–9], sidewalls [10], inside pits [11], or inside pits/on terraces at low/high temperature [12], revealing our incomplete understanding of the growth dynamics. Theoretical analyses focused firstly on equilibrium [11, 13–16]: Monte-Carlo simulations indicated that islands minimize the elastic energy on terraces rather than on pit-walls [17], while finite-element strain calculations showed that islands minimize energy inside pits with shallow enough sidewall angles [18]. Kinetic effects were investigated thanks to the computation of nucleation barriers [19], concluding that nucleation is favored in the valleys of a pattern thanks to the elastic relaxation. The linear instability analysis of the dynamics of a strained film on a sinusoidal substrate showed that growth is initially enhanced by the pattern while the lowest energy state corresponds to an anti-phase configuration [20].

We study in this Letter strained islands resulting from an instability grown on a pattern. We investigate the long-time evolution of the morphological Asaro-Tiller-Grinfel'd instability which leads to islands with a characteristic wavelength [21] on a pattern with a tunable wave-

length. We present a dynamical analysis of the growth and annealing on a pattern, generalizing a non-linear continuum model [22] which describes the nucleationless dynamics observed in low-strained ($x \lesssim 0.4$) $\text{Si}_{1-x}\text{Ge}_x$ films on Si [2]. Thanks to the analytical solution for the elastic field generated by the buried and patterned film/substrate interface, we numerically solve the surface diffusion equation on large scale systems and perform a systematic analysis of the resulting morphologies at large time. We investigate the parameters dictating the islands position and characteristics and relate them to the instability dynamics.

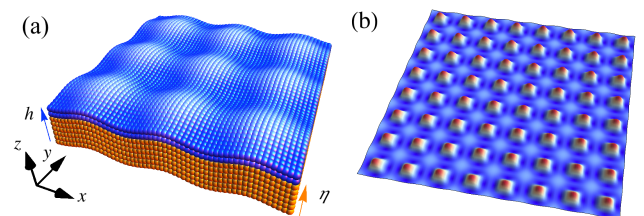


FIG. 1. (a) Film with a free surface at $z=h(x, y, t)$ deposited on a pattern at $z=\eta(x, y)$. (b) Stationary morphology resulting from the numerical integration of (1) on a $128l_0 \times 128l_0$ box, for $\lambda_\eta/\lambda_{\text{ATG}}=1$ and a film thickness $\bar{H}/H_c=1.8$.

Dynamical model.—We study a crystalline film bounded by a free surface at $z=h(\mathbf{r}, t)$ and the film/substrate interface at $z=\eta(\mathbf{r})$ where $\mathbf{r}=(x, y)$, see Fig. 1. The morphological evolution results from the surface diffusion due to elastic relaxation [22]

$$\frac{\partial h}{\partial t} = D\Delta[\mathcal{E}^{\text{el}} - \gamma\Delta h + \mu_w + \mu_{\text{anis}}] + F, \quad (1)$$

where D is the diffusion coefficient, F , the deposition flux and \mathcal{E}^{el} , the elastic energy density. The surface energy $\gamma = \gamma_w(h) + \gamma_{\text{anis}}(\mathbf{n})$ depends on the film height h and surface local orientation \mathbf{n} [23, 24], implying the wetting and anisotropic potentials $\mu_w(\text{anis}) = \frac{\delta}{\delta h} \int dS \gamma_w(\text{anis})$.

Wetting describes the influence of the film/substrate interface on the surface configuration [25]. It is described here by $\gamma_w = \gamma_f[1 + c_w \exp(-H/\delta_w)]$ which depends on the local film thickness $H(\mathbf{r}) = h(\mathbf{r}) - \eta(\mathbf{r})$, where γ_f is the film surface energy while c_w and δ_w can be derived from ab-initio calculations or experimental results [22]. Such a wetting potential even with small variations inhibits the instability below a critical thickness H_c of the order of a few nanometers [22] and leads to the formation of a wetting layer, in agreement with experimental results [4]. We use the anisotropic surface energy $\gamma_{\text{anis}}(\mathbf{n})$ given in [22], which describes a shallow (001) minimum and stiff (105) orientations according to experimental findings [26]. Finally, the pattern crucially affects the elastic energy and we generalize the computation of [22] to a patterned geometry by solving analytically the mechanical equilibrium equations in the small-slope approximation. The film/substrate interface is coherent so that displacements are generated throughout the system due to the misfit m between the film and substrate lattice parameters. A flat film is thence characterized by the elastic energy density $\bar{\mathcal{E}}_0$ [27], which is associated with the characteristic length scale $l_0 = \gamma_f/\bar{\mathcal{E}}_0$. Up to second order in the slope, $\mathcal{E}^{\text{el}} = \mathcal{E}_1 + \mathcal{E}_2$ where

$$\mathcal{E}_1 = -\mathcal{H}_{ii}[h] + \mathcal{B}[\mathcal{H}_{ii}[\eta]], \quad (2)$$

in units of $\bar{\mathcal{E}}_0$, with summation over repeated indices $i=x, y$, $\mathcal{H}_{ij}[h] = (k_i k_j / |\mathbf{k}|) h(\mathbf{k})$ in Fourier space along \mathbf{r} . Moreover, $\mathcal{B}[h] = \exp(-|\mathbf{k}| \bar{H}) h(\mathbf{k})$ describes the buried dipoles generated by the film/substrate interface with $\bar{H} = \langle H(\mathbf{r}) \rangle$. The linear analysis of (1) shows that above some critical thickness H_c , an harmonic modulation $H(\mathbf{r}, t) = \bar{H} + \epsilon \exp[i\mathbf{k} \cdot \mathbf{r} + \sigma t]$ has a positive growth rate σ for a continuum range of wavevectors which is maximum for $k_{\text{ATG}} = 2\pi/\lambda_{\text{ATG}}$, defining the instability wavelength λ_{ATG} [22]. At second order, $\mathcal{E}_2 = \mathcal{E}_2^{hh} + \mathcal{E}_2^{h\eta} + \mathcal{E}_2^{\eta\eta}$ with

$$\begin{aligned} \mathcal{E}_2^{\eta\eta} &= -\mathcal{B}[\eta \Delta \eta + |\nabla \eta|^2] + \mathcal{B}[\mathcal{H}_{ij}[\eta]] \theta_{ij}^{kl} \mathcal{B}[\mathcal{H}_{kl}[\eta]], \\ \mathcal{E}_2^{h\eta} &= -h \mathcal{B}[\Delta \eta] - 2 \mathcal{H}_{ij}[h] \theta_{ij}^{kl} \mathcal{B}[\mathcal{H}_{kl}[\eta]] \\ &\quad - 2 \mathcal{H}_{ij}[h \theta_{ij}^{kl} \mathcal{B}[\mathcal{H}_{kl}[\eta]]], \end{aligned} \quad (3)$$

while \mathcal{E}_2^{hh} and the geometrical tensor θ_{ij}^{kl} are given in [23]. Given the solution of the elastic equations (2)-(3), the evolution may be efficiently and systematically computed on large scales thanks to a numerical resolution of (1), where non-linearities prevent the instability to trivially diverge. Initially, $h(\mathbf{r}, t=0) = \eta(\mathbf{r})$, and we perform deposition up to \bar{t} for a given thickness \bar{H} , adding a white deposition noise in the r.h.s. of (1), and then consider annealing ($F=0$). As seen in experiments [22], the instability does not significantly grow during deposition with the flux usually used and an amplitude of the white noise of a few monolayers, so that we will not discuss these parameters [28].

Results.—The surface evolution results from the balance between (i) the surface curvature $-\Delta h$, lower in

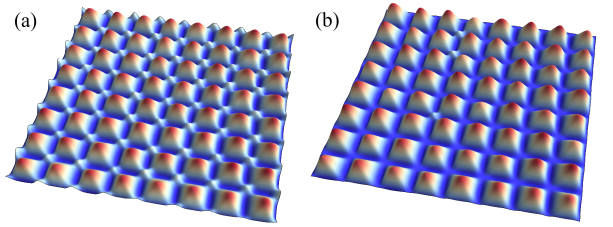


FIG. 2. Evolution for $\lambda_\eta/\lambda_{\text{ATG}} = 1.4$ and $\bar{H}/H_c = 7$. (a) The intermediate stage displays both islands on the peaks and valleys while (b) coarsening favors the latter.

the more coordinated regions (film valleys); (ii) the h -dependent elastic contribution $-\mathcal{H}_{ii}[h] + \mathcal{E}_2^{hh}$, lower in the relaxed regions (surface peaks); both effects are independent of the pattern; (iii) the buried dipoles potential $\mathcal{B}[\mathcal{H}_{ii}[\eta]] + \mathcal{E}_2^{\eta\eta}$, lower on the pattern valleys; and (iv) the interference contribution $\mathcal{E}_2^{h\eta}$, lower at peaks on the pattern for a film following the latter. We first study a pattern with an egg-carton shape, generic for other geometries, $\eta(\mathbf{r}) = A [\cos(2\pi x/\lambda_\eta) + \cos(2\pi y/\lambda_\eta)]$, Fig. 1. The instability, with the characteristic wavelength λ_{ATG} , grows on top of the pattern with λ_η . Of special interest is the ratio $\lambda_\eta/\lambda_{\text{ATG}}$ which rules the growth rate of the initial profile, and the film thickness \bar{H} , which rules the wetting and the buried dipoles interactions. As found on unpatterned substrates, the combination of anisotropy, elasticity and wetting leads to a slowdown in Ostwald coarsening [22], sometimes after some partial ripening. Consequently, we mainly examine stationary states (when the surface roughness, island density ... are constant) characterized by pyramids with (105) facets [29]. The following results were derived for $c_w = 0.1$, $\delta_w = 0.01$ and $A/l_0 = 0.1$ but are generic for other parameters [30].

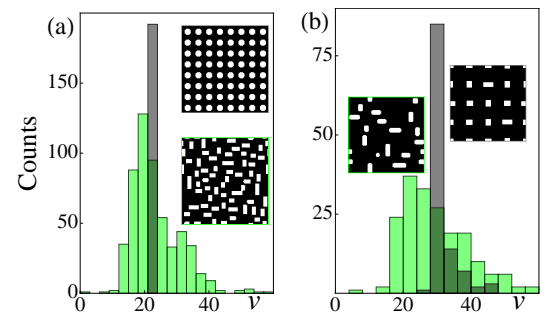


FIG. 3. Island size distribution in the stationary state on a pattern (grey), compared to the flat substrate case with similar conditions (green) for (a) $\lambda_\eta/\lambda_{\text{ATG}} = 1$, $\bar{H}/H_c = 1.8$, (b) $\lambda_\eta/\lambda_{\text{ATG}} = 2.7$, $\bar{H}/H_c = 1.1$.

We first consider the wavelength coincidence ($\lambda_\eta = \lambda_{\text{ATG}}$) and depict two typical geometries in Figs. 1 and 2 resulting from the numerical resolution of Eq. (1). For $\bar{H}/H_c = 1.8$, islands arise after the initial instability, grow

and remain in the valleys of the pattern, forming a well-organized array, Fig. 1. The island size distribution (ISD) in the stationary state is narrow and significantly improved compared to the flat substrate case, Fig. 3. Each island grows in one valley and gathers a rather uniform volume, reducing the chemical potential differences between islands and coarsening, thus consolidating their uniformity. For $\bar{H}/H_c = 7$, a similar evolution occurs but with intermediate states where islands coexist both in the valleys and peaks, Fig. 2; however, the former gradually disappear, leading to uniform islands in the valleys.

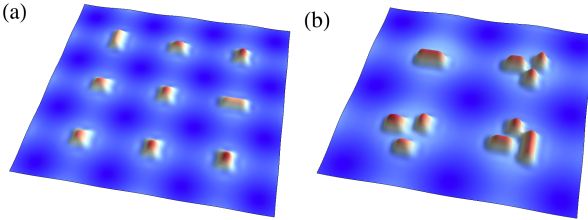


FIG. 4. Stationary morphology for $\bar{H}/H_c = 1.1$ and (left) $\lambda_\eta/\lambda_{ATG} = 2.7$ and (right) $\lambda_\eta/\lambda_{ATG} = 6$.

When $\lambda_\eta/\lambda_{ATG} \gtrsim 1$, similar results are found except when \bar{H} is only slightly larger than H_c , Fig. 4. There, islands grow and remain on the pattern peaks. Each peak is decorated by a single island when $\lambda_\eta/\lambda_{ATG}$ is not too large, and the islands display a narrow ISD, Fig. 3. For larger $\lambda_\eta/\lambda_{ATG}$, clusters of islands arise on the peaks at low \bar{H} as the typical volume available for each top becomes large compared to the typical volume of isolated islands found at low λ_η . For large \bar{H}/H_c and $\lambda_\eta/\lambda_{ATG}$, and for large $\lambda_\eta/\lambda_{ATG}$, a mainly disordered configuration similar to the flat substrate case occurs as the influence of the pattern is low, Fig. 3.

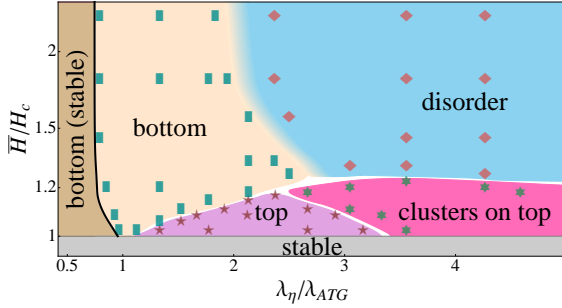


FIG. 5. Phase diagram displaying the localization of islands grown on an egg-carton substrate as a function of the film thickness to critical height ratio \bar{H}/H_c and the pattern to instability wavelength ratio $\lambda_\eta/\lambda_{ATG}$. Symbols show the simulations which set the boundaries. The instability does not develop on the left side of the solid line and when $\bar{H} < H_c$.

Our results are summarized in the phase diagram Fig. 5, displaying the morphology in the stationary state as a function of $\lambda_\eta/\lambda_{ATG}$ and \bar{H}/H_c . For small $\lambda_\eta/\lambda_{ATG}$,

a corrugation with λ_η has a negative growth rate (capillarity overcomes relaxation) and shrinks after skipping to an out-of-phase configuration (label ‘bottom (stable)'). For $\lambda_\eta/\lambda_{ATG} \gtrsim 1$, islands grow in the valleys for large \bar{H} (‘bottom') but possibly on the peaks when \bar{H} is slightly above H_c (‘top'). Finally, for large $\lambda_\eta/\lambda_{ATG}$, island clusters arise on the peaks for thin films (‘clusters on top') while a disordered morphology occurs otherwise (‘disorder').

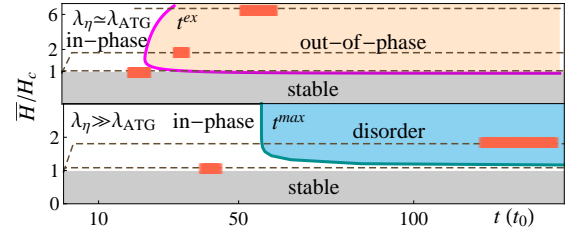


FIG. 6. Typical kinetic phase diagram for (top) $\lambda_\eta/\lambda_{ATG} = 1.4$ and (bottom) $\lambda_\eta/\lambda_{ATG} = 6$, displaying the morphology as a function of time t and thickness \bar{H} . The dotted line represents the thickness evolution during deposition and annealing. Orange rectangles indicate the time when islands form. The t^{ex} line characterizes the shift from in- to out-of-phase of the linear solution of (1) [31], while t^{max} characterizes the time when $h(k_{ATG}) = h(k_\eta)$ for this solution [31].

Initial evolution.—To rationalize these findings, we investigate the instability initial evolution which is described by the linear solution of Eq. (1) [31]. The initial condition corresponds to a film following the pattern (in-phase). When $\lambda_\eta/\lambda_{ATG}$ is not too large, the film skips in the linear regime from in- to out-of-phase after the time t^{ex} . Otherwise, when $\lambda_\eta/\lambda_{ATG}$ is large, the k_{ATG} mode may become larger than k_η after some time t^{max} , before this phase-shift occurs, Fig. 6. However, the linear solution describes only the initial evolution and we indicate in Fig. 6 the typical time when the islands emerge in the full non-linear analysis, which is best characterized by the saturation of the surface roughness once the islands form, Fig. 7 [32]. We find in our systematic analysis that

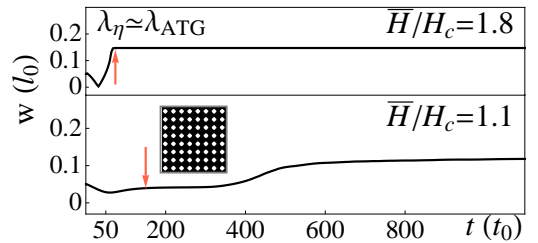


FIG. 7. Evolution of the surface roughness w for $\lambda_\eta/\lambda_{ATG} = 1.4$ and $\bar{H}/H_c = 1.1$ and 1.8 (solid line). The snapshot of the islands for $t = 200$ is displayed in the inset when $\bar{H}/H_c = 1.1$. Orange arrows indicate the time of appearance of well-defined islands.

the island localization in the stationary state corresponds

to the morphology of the instability when the islands and the wetting layer form. Note that in some special cases (especially near the frontier between the ‘top’ and ‘bottom’ regions in Fig. 5), coarsening due to non-linearities may cause the disappearance of some islands, either to the benefit of islands on similar positions, or, when they coexist, from peaks to valleys where strain is more efficiently relaxed. For example, when $\lambda_\eta/\lambda_{\text{ATG}} = 1.4$ and $\bar{H}/H_c = 1.1$, Fig. 7, the first islands to grow are isotropic and display a small size dispersion which lowers the coarsening driving force. The system evolves slowly before small fluctuations eventually lead to ripening and the formation of larger pyramids which coarsening is then again interrupted. Therefore, both the anisotropy and the narrow ISD enforced by patterning cause the coarsening slowdown.

Beyond single-mode—Many patternings generate arrays of pits instead of sinusoidal shapes. They may be characterized by their wavelength λ_η , depth A and width w and we study a nearly-gaussian pit profile $\eta = -A \exp\{-\lambda_\eta [\cos(2\pi x/\lambda_\eta) + \cos(2\pi y/\lambda_\eta) + 2]/w\}$. When $\lambda_\eta/\lambda_{\text{ATG}} = 1.4$ and $w/\lambda_{\text{ATG}} = 1$, we find that the islands locate on the terraces in between the pits when $\bar{H}/H_c = 1.1$, while they grow inside the pits when $\bar{H}/H_c = 1.8$, Fig. 8. Both results are similar to peak and valley locations in the egg-carton case for $\lambda_\eta/\lambda_{\text{ATG}} = 1.4$ and $\bar{H}/H_c = 1.1$ and 1.8 respectively, Fig. 5. Similar island locations in the egg-carton and pit cases may also be found at constant λ_η and \bar{H} when changing w . Looking at the Fourier transform of the pattern (which is also the surface initial condition) rationalizes these similarities as it characterizes the initial spectrum which linear evolution rationalizes the islands location as explained above. It is noteworthy that a small change in the deposited thickness (\bar{H} shifts in the example of Fig. 8 from 5 nm to 8 nm on a $\text{Si}_{0.75}\text{Ge}_{0.25}$ film) may lead to a dramatic change in the island localization.

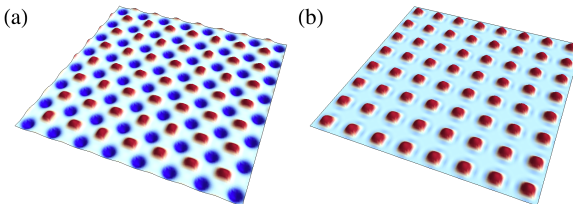


FIG. 8. Islands grown on pits with $\lambda_\eta/\lambda_{\text{ATG}} = 1.4$, $w/\lambda_{\text{ATG}} = 1$ and (a) $\bar{H}/H_c = 1.1$ while (b) $\bar{H}/H_c = 1.8$.

Relation with experiments.—A systematic experimental investigation of the island positioning as a function of λ_η and \bar{H} in low- x $\text{Si}_{1-x}\text{Ge}_x$ films on Si would be valuable to check the modelization and rationalize the island positioning. Similarly to experiments of Ge films on Si [4, 5], we find in some conditions uniform and ordered islands which do not coarsen and locate either on peaks or

valleys of the pattern. However, our model describes the nucleationless evolution occurring on low- x films [2, 22] but not on high-strained Ge films where nucleation is crucial in the initial stage [1, 33]. Other parameters may also be important: (i) the pattern geometry which defines the surface initial condition; (ii) alloying, especially at high temperature, may be relevant in particular to describe a pattern smoothing [16, 34]; (iii) evaporation and condensation may also come into play when epitaxy is not performed in high-vacuum conditions [35]. By considering a minimal modelization already relevant on flat substrates [22], our results are aimed at identifying the basic mechanisms at work.

In Summary, we devise a dynamical continuum model describing the morphological instability and quantum dot growth in strained films on a pattern. We solve elasticity at non-linear order to investigate the long-time dynamics. We find different regimes where islands form ordered and uniform arrays either on the pattern peaks or valleys depending on the film thickness and ratio between the instability wavelength to the pattern characteristic length. These findings are rationalized by the linear analysis valid prior to island growth. Extension of this work to other geometries and to the nucleation case using kinetic Monte-Carlo simulations [36] are under investigation.

-
- [1] D. J. Eaglesham and M. Cerullo, *Phys. Rev. Lett.* **64**, 1943 (1990); Y. W. Mo, D. E. Savage, B. S. Swartzentruber, and M. G. Lagally, *Phys. Rev. Lett.* **65**, 1020 (1990).
 - [2] P. Sutter and M. G. Lagally, *Phys. Rev. Lett.* **84**, 4637 (2000); R. M. Tromp, F. M. Ross, and M. C. Reuter, *Phys. Rev. Lett.* **84**, 4641 (2000).
 - [3] see e.g. J. A. Floro, M. B. Sinclair, E. Chason, L. B. Freund, R. D. Tweten, R. D. Hwang, and G. A. Lucadamo, *Phys. Rev. Lett.* **84**, 701 (2000); S. Miyamoto, O. Moutanabbir, E. E. Haller, and K. M. Itoh, *Phys. Rev. B* **79**, 165415 (2009).
 - [4] J. N. Aqua, I. Berbezier, L. Favre, T. Frisch, and A. Ronda, *Phys. Rep.* **522**, 59 (2013).
 - [5] M. Grydlik, G. Langer, T. Fromherz, F. Schäffler, and M. Brehm, *Nanotechnol.* **24**, 105601 (2013).
 - [6] G. Jin, J. L. Liu, S. G. Thomas, Y. H. Luo, K. L. Wang, and B.-Y. Nguyen, *Appl. Phys. Lett.* **75**, 2752 (1999).
 - [7] T. Kitajima, B. Liu, and S. R. Leone, *Appl. Phys. Lett.* **80**, 497 (2002).
 - [8] B. Yang, F. Liu, and M. G. Lagally, *Phys. Rev. Lett.* **92**, 025502 (2004).
 - [9] P. D. Szkutnik, A. Sgarlata, S. Nufris, N. Motta, and A. Balzarotti, *Phys. Rev. B* **69**, 201309 (2004).
 - [10] Z. Zhong, A. Halilovic, M. Muhlberger, F. Schäffler, and G. Bauer, *Appl. Phys. Lett.* **82**, 445 (2003).
 - [11] Z. Zhong, A. Halilovic, T. Fromherz, F. Schäffler, and G. Bauer, *Appl. Phys. Lett.* **82**, 4779 (2003); Z. Zhong, W. Schwinger, F. Schäffler, G. Bauer, G. Vastola, F. Montalenti, and L. Miglio, *Phys. Rev. Lett.* **98**,

- 176102 (2007); M. Bollani, D. Chrastina, A. Fedorov, R. Sordan, A. Picco, and E. Bonera, *Nanotechnol.* **21**, 475302 (2010); Y. J. Ma, Z. Zhong, X. J. Yang, Y. L. Fan, and Z. M. Jiang, *Nanotechnol.* **24**, 015304 (2013).
- [12] I. Berbezier and A. Ronda, *Surf. Sci. Rep.* **64**, 47 (2009).
- [13] R. V. Kukta and D. Kouris, *J. Appl. Phys.* **97**, 033527 (2005).
- [14] A. Bavard, J. Eymery, A. Pascale, and F. Fournel, *Phys. Stat. Sol. (b)* **243**, 3963 (2006).
- [15] G. Katsaros, J. Tersoff, M. Stoffel, A. Rastelli, P. Acosta-Diaz, G. S. Kar, G. Costantini, O. G. Schmidt, and K. Kern, *Phys. Rev. Lett.* **101**, 096103 (2008).
- [16] T. U. Schülli, G. Vastola, M.-I. Richard, A. Malachias, G. Renaud, F. Uhlík, F. Montalenti, G. Chen, L. Miglio, F. Schäffler, and G. Bauer, *Phys. Rev. Lett.* **102**, 025502 (2009).
- [17] A. Pascale, I. Berbezier, A. Ronda, and P. C. Kelires, *Phys. Rev. B* **77**, 075311 (2008).
- [18] G. Vastola, M. Grydlik, M. Brehm, T. Fromherz, G. Bauer, F. Boioli, L. Miglio, and F. Montalenti, *Phys. Rev. B* **84**, 155415 (2011).
- [19] H. Hu, H. J. Gao, and F. Liu, *Phys. Rev. Lett.* **101**, 216102 (2008).
- [20] H. Wang, Y. Zhang, and F. Liu, *J. Appl. Phys.* **104**, 054301 (2008).
- [21] R. J. Asaro and W. A. Tiller, *Metall. Trans.* **3**, 1789 (1972); M. A. Grinfeld, *Sov. Phys. Dokl.* **31**, 831 (1986).
- [22] J.-N. Aqua, A. Gouyé, A. Ronda, T. Frisch, and I. Berbezier, *Phys. Rev. Lett.* **110**, 096101 (2013).
- [23] J.-N. Aqua and T. Frisch, *Phys. Rev. B* **82**, 085322 (2010).
- [24] J. N. Aqua, A. Gouyé, T. Auphan, T. Frisch, A. Ronda, and I. Berbezier, *Appl. Phys. Lett.* **98**, 161909 (2011).
- [25] see e.g. P. Müller and R. Kern, *Appl. Surf. Sci.* **102**, 6 (1996); C.-H. Chiu and H. Gao, in *Thin Films: Stresses and Mechanical Properties V, MRS Symposia Proceedings No. 356*, edited by S. P. Baker *et al.* (Materials Research Society, Pittsburgh, 1995) p. 33.
- [26] J. Tersoff, B. J. Spencer, A. Rastelli, and H. von Känel, *Phys. Rev. Lett.* **89**, 196104 (2002).
- [27] $\bar{\mathcal{E}}_0 = 4Ym^2(1+\nu)/(1-\nu)$ where Y is the Young's modulus and ν , the Poisson's ratio.
- [28] a dependence on F may arise for large F as shown in J.-N. Aqua, T. Frisch, and A. Verga, *Phys. Rev. E* **81**, 021605 (2010).
- [29] While other shapes arise at large thickness.
- [30] They are still relevant in the range $0.01 < A/l_0 < 0.4$ when the pattern slope is lower than the (105) slope, and for $c_w = 0.05, 0.1$ and 0.2 .
- [31] X. Xu, J.-N. Aqua, and T. Frisch, *J. Phys. : Condens. Matter* **24**, 045002 (2012); *C. R. Phys.* **14**, 199 (2013).
- [32] The linear evolution is made of exponentials and its initial decrease corresponds to the shift from in- to out-of-phase [31].
- [33] C.-H. Lam, C.-K. Lee, and L. M. Sander, *Phys. Rev. Lett.* **89**, 216102 (2002).
- [34] R. Bergamaschini, J. Tersoff, Y. Tu, J. J. Zhang, G. Bauer, and F. Montalenti, *Phys. Rev. Lett.* **109**, 156101 (2012).
- [35] P. Liu, C. Lu, and Y. W. Zhang, *Phys. Rev. B* **76**, 085336 (2007).
- [36] J.-N. Aqua and T. Frisch, *Phys. Rev. B* **78**, 121305(R) (2008); P. Gaillard, J.-N. Aqua, and T. Frisch, *Phys. Rev. B* **87**, 125310 (2013).

Bibliography

- [ALE 88] ALERHAND O., VANDERBILT D., MEADE R. D., JOANNOPOULOS J.
Spontaneous formation of stress domains on crystal surfaces. *Physical review letters*, vol. 61, n° 17, 1988, p. 1973–1976, APS.
- [AQU 07] AQUA J.-N., FRISCH T., VERGA A.
Nonlinear evolution of a morphological instability in a strained epitaxial film. *Phys. Rev. B*, vol. 76, 2007, Page 165319, APS.
- [AQU 10a] AQUA J.-N., FRISCH T.
Influence of surface energy anisotropy on the dynamics of quantum dot growth. *Phys. Rev. B*, vol. 82, 2010, Page 085322, American Physical Society.
- [AQU 10b] AQUA J.-N. AND FRISCH T., VERGA A.
Ordering of strained islands during surface growth. *Phys. Rev. E*, vol. 81, 2010, Page 021605, American Physical Society.
- [AQU 11] AQUA J.-N., GOUYÉ A., AUPHAN T., FRISCH T., RONDA A., BERBEZIER I.
Orientation dependence of the elastic instability on strained SiGe films. *Appl. Phys. Lett.*, vol. 98, 2011, Page 161909.
- [AQU 13] AQUA J.-N., GOUYÉ A., RONDA A., FRISCH T., BERBEZIER I.
Interrupted Self-Organization of SiGe Pyramids. *Physical Review Letters*, vol. 110, n° 9, 2013, Page 096101, APS.
- [ASA 72a] ASARO R. J., TILLER W. A.
Interface morphology developppment during stress-corrosion cracking: Part 1. Via surface diffusion. *Metall. Trans.*, vol. 3, 1972, Page 1789.
- [ASA 72b] ASARO R. J., TILLER W. A.
Interface morphology developppment during stress-corrosion cracking: Part 1. Via surface diffusion. *Metall. Trans.*, vol. 3, 1972, p. 1789–1796. ; M. A. Grinfel'd, Sov. Phys. Dokl. 31, 831 (1986).
- [BAI 88] BAIBICH M. N., BROTO J. M., FERT A., VAN DAU F. N., PETROFF F., ETIENNE P., CREUZET G., FRIEDERICH A., CHAZELAS J.
Giant Magnetoresistance of (001)Fe/(001)Cr Magnetic Superlattices. *Phys. Rev. Lett.*, vol. 61, 1988, p. 2472–2475, American Physical Society.

Bibliography

- [Bal 05] BALIBAR S., ALLES H., PARSHIN A. Y.
Helium crystals under stress: the Grinfeld instability. *Rev. Mod. Phys.*, vol. **77**, 2005,
Page 317.
- [BER 92] BERREHAR J., CAROLI C., LAPERSONNE-MEYER C., SCHOTT M.
Surface patterns on single-crystal films under uniaxial stress: Experimental evidence
for the Grinfeld instability. *Physical Review B*, vol. **46**, n° 20, 1992, Page 13487,
APS.
- [BER 95] BERMOND J. M., MÉTOIS J. J., EGÉA X., FLORET F.
The equilibrium shape of silicon. *Surf. Sci.*, vol. **330**, 1995, Page 48.
- [BER 98] BERBEZIER I., GALLAS B., DERRIEN J.
Elastic strain relaxation in $\text{Si}_{1-x}\text{Ge}_x$ layers epitaxially grown on Si substrates. *Surf.*
Rev. Lett., vol. **5**, 1998, Page 133.
- [BER 02] BERBEZIER I., RONDA A., PORTAVOCE A.
SiGe nanostructures: new insights into growth processes. *J. Phys. : Condens. Matter*,
vol. **14**, 2002, Page 8283.
- [BER 09] BERBEZIER I., RONDA A.
SiGe nanostructures: strain control, dopant incorporation and properties. *Surface Sci-
ence Reports*, vol. **64**, 2009, p. 47–98.
- [BER 12] BERGAMASCHINI R., TERSOFF J., TU Y., ZHANG J., BAUER G., MONTAL-
ENTI F.
Anomalous smoothing preceding island formation during growth on patterned sub-
strates. *Physical review letters*, vol. **109**, n° 15, 2012, Page 156101, APS.
- [BIN 89] BINASCH G., GRÜNBERG P., SAURENBACH F., ZINN W.
Enhanced magnetoresistance in layered magnetic structures with antiferromagnetic in-
terlayer exchange. *Physical Review B*, vol. **39**, 1989, p. 4828–4830.
- [BOD 86] BODENSOHN J., NICOLAI K., LEIDERER P.
The growth of atomically rough ^4He crystals. *Zeitschrift für Physik B Condensed Mat-
ter*, vol. **64**, n° 1, 1986, p. 55–64, Springer.
- [BOL 10] BOLLANI M., CHRASTINA D., FEDEROV A., SORDAN R., PICCO A., BON-
ERA E.
Ge-rich islands grown on patterned Si substrates by low-energy plasma-enhanced
chemical vapour deposition. *Nanotechn.*, vol. **21**, 2010, Page 475302.
- [BOY 97] BOYKIN T. B.
Improved fits of the effective masses at Γ in the spin-orbit, second-nearest-neighbor
 sp^3s^* model: Results from analytic expressions. *Physical Review B*, vol. **56**,
n° 15, 1997, Page 9613, APS.
- [BUT 92] BUTZ R., KAMPERS S.
2xn surface structure of SiGe layers deposited on Si(100). *Appl. Phys. Lett.*, vol. **61**,
1992, Page 1307, AIP.

- [CHE 95] CHEN K. M., JESSON D. E., PENNYCOOK S. J., MOSTOLLER M., KAPLAN T., THUNDAT T., WARMACK R. J.
Step Instabilities: A New Kinetic Route to 3D Growth. *Phys. Rev. Lett.*, vol. 75, 1995, Page 1582, American Physical Society.
- [CHE 06] CHEN G., LICHTENBERGER H., BAUER G., JANTSCH W., SCHÄFFLER F.
Initial stage of the two-dimensional to three-dimensional transition of a strained SiGe layer on a pit-patterned Si(001) template. *Phys. Rev. B*, vol. 74, 2006, Page 035302, American Physical Society.
- [CHI 93] CHIU C.-H., GAO H.
Stress singularities along a cycloid rough surface. *Int. J. Solids Structures*, vol. 30, 1993, Page 2983.
- [CHI 94] CHIU C.-H., GAO H.
A numerical study of stress controlled surface diffusion during epitaxial film growth. *MRS Proceedings*, vol. 356 Cambridge Univ Press, 1994.
- [CHI 04] CHIU C.-H.
Stable and uniform arrays of self-assembled nanocrystalline islands. *Phys. Rev. B*, vol. 69, 2004, Page 165413, American Physical Society.
- [CHI 06] CHIU C. H., HUANG Z.
Common features of nanostructure formation induced by the surface undulation on the Stranski-Krastanow systems. *Appl. Phys. Lett.*, vol. 89, 2006, Page 171904, AIP.
- [CHO 94] CHO A.
Molecular Beam Epitaxy, Key Papers in Physics. American Institute of Physics, New York, 1994.
- [COE 02] COE S., WOO W.-K., MOUNGI BAWENDI V. B.
Electroluminescence from single monolayers of nanocrystals in molecular organic devices. *Nature*, vol. 420, n° 6917, 2002, p. 800–803, Nature Publishing Group.
- [COL 94] COLVIN V., SCHLAMP M., ALIVISATOS A. et al.
Light-emitting diodes made from cadmium selenide nanocrystals and a semiconducting polymer. *Nature*, vol. 370, n° 6488, 1994, p. 354–357.
- [CRO 98] CRONENWETT S. M., OOSTERKAMP T. H., KOUWENHOVEN L. P.
A tunable Kondo effect in quantum dots. *Science*, vol. 281, n° 5376, 1998, p. 540–544, American Association for the Advancement of Science.
- [CUL 92] CULLIS A. G., ROBBINS D. J., PIDDUCK A. J., SMITH P. W.
The characteristics of strain-modulated surface undulations formed upon epitaxial $\text{Si}_{1-x}\text{Ge}_x$ alloy layers on Si. *J. Cryst. Growth*, vol. 123, 1992, Page 333.
- [EAG 90a] EAGLESHAM D. J., CERULLO M.
Dislocation-free Stranski-Krastanow growth of Ge on Si(100). *Phys. Rev. Lett.*, vol. 64, 1990, Page 1943, American Physical Society.
- [EAG 90b] EAGLESHAM D. J., CERULLO M.
Dislocation-free Stranski-Krastanow growth of Ge on Si(100). *Phys. Rev. Lett.*,

Bibliography

- vol. **64**, n° 16, 1990, Page 1943. ; H. Gao and W. Nix, *Annu. Rev. Mater. Sci.* **29**, 173 (1999); P. Sutter *et al.*, *Phys. Rev. Lett.* **84**, 4637 (2000); R. M. Tromp *et al.*, *ibid.* **84**, 4641 (2000); J. Tersoff *et al.*, *ibid.* **89**, 196104 (2002); I. Berbezier *et al.*, *J. Phys.: Condens. Matter* **14**, 8283 (2002); A. Rastelli *et al.*, *Phys. Rev. Lett.* **95**, 026103 (2005).
- [EAG 90c] EAGLESHAM D., GOSSMANN H., CERULLO M.
Island formation in Ge on Si heteroepitaxy. *Epitaxial Heterostructures*, vol. 198, 1990, Page 51, Cambridge Univ Press.
- [EAG 93a] EAGLESHAM D. J., UNTERWALD F. C., JACOBSON D. C.
Growth morphology and the equilibrium shape: The role of “surfactants” in Ge/Si island formation. *Phys. Rev. Lett.*, vol. 70, 1993, Page 966.
- [EAG 93b] EAGLESHAM D. J., WHITE A. E., FELDMAN L. C., MORIYA N., JACOBSON D. C.
Equilibrium shape of Si. *Phys. Rev Lett.*, vol. 70, 1993, Page 1643.
- [ESA 70] ESAKI L., TSU R.
Superlattice and negative differential conductivity in semiconductors. *IBM Journal of Research and Development*, vol. 14, n° 1, 1970, p. 61–65, IBM.
- [FLO 99] FLORO J. A., CHASON E., FREUND L. B., TWESTEN R. D., HWANG R. Q., LUCADAMO G. A.
Evolution of coherent islands in $\text{Si}_{1-x}\text{Ge}_x/\text{Si}(001)$. *Phys. Rev. B*, vol. **59**, 1999, Page 1990, American Physical Society.
- [FLO 00] FLORO J. A., SINCLAIR M. B., CHASON E., FREUND L. B., TWESTEN R. D., HWANG R. Q., LUCADAMO G. A.
Novel SiGe Island Coarsening Kinetics: Ostwald Ripening and Elastic Interactions. *Phys. Rev. Lett.*, vol. 84, 2000, p. 701–704, American Physical Society.
- [FUJ 02] FUJIKAWA Y., AKIYAMA K., NAGAO T., SAKURAI T., LAGALLY M. G., HASHIMOTO T., MORIKAWA Y., TERAKURA K.
Origin of the Stability of Ge(105) on Si: A New Structure Model and Surface Strain Relaxation. *Phys. Rev. Lett.*, vol. 88, 2002, Page 176101, American Physical Society.
- [GAO 99a] GAO H., NIX W.
Surface roughening of heteroepitaxial thin film. *Annu. Rev. Mater. Sci.*, vol. **29**, 1999, Page 173.
- [GAO 99b] GAO H., NIX W. D.
Surface roughening of heteroepitaxial thin films. *Annual Review of Materials Science*, vol. 29, n° 1, 1999, p. 173–209, Annual Reviews 4139 El Camino Way, PO Box 10139, Palo Alto, CA 94303-0139, USA.
- [GOL 03] GOLOVIN A. A., DAVIS S. H., VOORHEES P. W.
Self-organization of quantum dots in epitaxially strained solid films. *Phys. Rev. E*, vol. **68**, 2003, Page 056203.

- [GOL 05] GOLDFARB I.
Effect of Strain on the Appearance of Subcritical Nuclei of Ge Nanohuts on Si(001).
Phys. Rev. Lett., vol. 95, 2005, Page 025501, American Physical Society.
- [GRI 86] GRINFELD M. A.
Instability of the separation boundary between a nonhydrostatically stressed elastic body and a melt. *Sov. Phys. Dokl.*, vol. 31, 1986, Page 831.
- [HU 08] HU H., GAO H. J., LIU F.
Theory of Directed Nucleation of Strained Islands on Patterned Substrates. *Phys. Rev. Lett.*, vol. 101, 2008, Page 216102, American Physical Society.
- [HUL 92] HULL R., BEAN J., PETICOLAS L., BAHNCK D., WEIR B., FELDMAN L.
Quantitative analysis of strain relaxation in $\text{Ge}_{\frac{1}{2}} \text{Si}_{\frac{1}{2}}$ (110) heterostructures and an accurate determination of stacking fault energy in $\text{Ge}_{\frac{1}{2}} \text{Si}_{\frac{1}{2}}$ alloys. *Applied physics letters*, vol. 61, n° 23, 1992, p. 2802–2804, AIP.
- [JES 00] JESSON D. E., KÄSTNER M., VOIGTLÄNDER B.
Direct Observation of Subcritical Fluctuations during the Formation of Strained Semiconductor Islands. *Phys. Rev. Lett.*, vol. 84, 2000, Page 330, American Physical Society.
- [JIN 99] JIN G., LIU J. L., THOMAS S. G., LUO Y. H., WANG K. L., NGUYEN B.-Y.
Controlled arrangement of self-organized Ge islands on patterned Si (001) substrates. *Appl. Phys. Lett.*, vol. 75, 1999, Page 2752, AIP.
- [JOY 85] JOYCE B.
Molecular beam epitaxy. *Reports on Progress in Physics*, vol. 48, n° 12, 1985, Page 1637, IOP Publishing.
- [KÄS 99] KÄSTNER M., VOIGTLÄNDER B.
Kinetic Self-Limiting Growth of Ge Islands on Si(001). *Phys. Rev. Lett.*, vol. 82, 1999, Page 2745, American Physical Society.
- [KAM 97] KAMINS T. I., WILLIAMS R. S.
Lithographic positioning of self-assembled Ge islands on Si(001). *Appl. Phys. Lett.*, vol. 71, 1997, Page 1201, AIP.
- [KAN 98] KANE B. E.
A silicon-based nuclear spin quantum computer. *nature*, vol. 393, n° 6681, 1998, p. 133–137, Nature Publishing Group.
- [KAS 00] KASTNER M.
The single electron transistor and artificial atoms. *Ann. Phys.(Leipzig)*, vol. 9, n° 11-12, 2000, p. 885–894.
- [KAT 08] KATSAROS G., TERSOFF J., STOFFEL M., RASTELLI A., ACOSTA-DIAZ P., KAR G. S., COSTANTINI G., SCHMIDT O. G., KERN K.
Positioning of Strained Islands by Interaction with Surface Nanogrooves. *Phys. Rev. Lett.*, vol. 101, 2008, Page 096103, American Physical Society.

Bibliography

- [KIM 98] KIM E. S., USAMI N., SHIRAKI Y.
Control of Ge dots in dimension and position by selective epitaxial growth and their optical properties. *Appl. Phys. Lett.*, vol. 72, 1998, Page 1617.
- [KIM 99] KIM E. S., USAMI N., SHIRAKI Y.
Selective epitaxial growth of dot structures on patterned Si substrates by gas source molecular beam epitaxy. *Semicond. Sci. Technol.*, vol. 14, 1999, Page 257.
- [KIT 02] KITAJIMA T., LIU B., LEONE S. R.
Two-dimensional periodic alignment of self-assembled Ge islands on patterned Si(001) surfaces. *Appl. Phys. Lett.*, vol. 80, 2002, Page 497, AIP.
- [KOH 03] KOHLERT P., KASSNER K., MISBAH C.
Large-amplitude behavior of the Grinfeld instability: a variational approach. *Eur. Phys. J. B*, vol. 35, 2003, Page 493.
- [LEV 07] LEVINE M. S., GOLOVIN A. A., DAVIS S. H., VOORHEES P. W.
Self-assembly of quantum dots in a thin epitaxial film wetting an elastic substrate. *Phys. Rev. B*, vol. 75, 2007, Page 205312.
- [LI 03] LI K., BOWLER D. R., GILLAN M. J.
Tight binding studies of strained Ge/Si(001) growth. *Surf. Sci.*, vol. 526, 2003, Page 356.
- [LIP 10] LIPPS F., PEZZOLI F., STOFFEL M., DENEKE C., THOMAS J., RASTELLI A., KATAEV V., SCHMIDT O. G., BÜCHNER B.
Electron spin resonance study of Si/SiGe quantum dots. *Phys. Rev. B*, vol. 81, 2010, Page 125312.
- [LU 05] LU G.-H., LIU F.
Towards Quantitative Understanding of Formation and Stability of Ge Hut Islands on Si(001). *Phys. Rev. Lett.*, vol. 94, 2005, Page 176103.
- [MA 13] MA Y., ZHONG Z., YANG X., FAN Y., JIANG Z.
Factors influencing epitaxial growth of three-dimensional Ge quantum dot crystals on pit-patterned Si substrate. *Nanotechnology*, vol. 24, n° 1, 2013, Page 015304, IOP Publishing.
- [MAT 74] MATTHEWS J. W., BLAKESLEE A. E.
Defects in epitaxial multilayers: I. Misfit dislocations. *J. Cryst. Growth*, vol. 27, 1974, Page 118.
- [MCK 08] MCKAY M. R., VENABLES J. A., DRUCKER J.
Kinetically Suppressed Ostwald Ripening of Ge/Si(100) Hut Clusters. *Phys. Rev. Lett.*, vol. 101, 2008, Page 216104, American Physical Society.
- [MED 98] MEDEIROS-RIBEIRO G., BRATKOVSKI A. M., KAMINS T. I., OHLBERG D. A. A., WILLIAMS S. R.
Shape Transition of Germanium Nanocrystals on a Silicon (001) Surface from Pyramids to Domes. *Science*, vol. 279, 1998, Page 353.

- [MIC 05] MICHALET X., PINAUD F., BENTOLILA L., TSAY J., DOOSE S., LI J., SUNDARESAN G., WU A., GAMBHIR S., WEISS S.
Quantum dots for live cells, in vivo imaging, and diagnostics. *Science*, vol. 307, n° 5709, 2005, p. 538–544, American Association for the Advancement of Science.
- [MIG 04] MIGAS D. B., CEREDA S., MONTALENTI F., MIGLIO L.
Electronic and elastic contributions in the enhanced stability of Ge(1 0 5) under compressive strain. *Surf. Sci.*, vol. 556, 2004, Page 121.
- [MIY 09] MIYAMOTO S., MOUTANABBIR O., HALLER E. E., ITOH K. M.
Spatial correlation of self-assembled isotopically pure Ge/Si (001) nanoislands. *Physical Review B*, vol. 79, n° 16, 2009, Page 165415, APS.
- [MO 90] MO Y. W., SAVAGE D. E., SWARTZENTRUBER B. S., LAGALLY M. G.
Kinetic pathway in Stranski-Krastanov growth of Ge on Si(001). *Phys. Rev. Lett.*, vol. 65, 1990, Page 1020, American Physical Society.
- [MON 09] MONTORO L. A., LEITE M. S., BIGGEMANN D., PETERNELLA F. G., BATENBURG K. J., MEDEIROS-RIBEIRO G., RAMIREZ A. J.
Revealing Quantitative 3D Chemical Arrangement on Ge-Si Nanostructures. *J. Phys. Chem. C*, vol. 113, 2009, Page 9018, American Chemical Society.
- [MÜL 96] MÜLLER P., KERN R.
The physical origin of the two-dimensional towards three-dimensional coherent epitaxial Stranski-Krastanov transition. *Applied surface science*, vol. 102, 1996, p. 6–11, Elsevier.
- [MÜL 08] MÜLLER P., MÉTOIS J. J.
Anisotropy of the surface thermodynamic properties of silicon. *Thin Solid Films*, vol. 517, 2008, Page 65.
- [NOZ 91] NOZIÈRES P.
Shape and growth of crystals. *C. Godrèche (Ed.), Solids far from equilibrium*, Page 1 Cambridge University Press, Cambridge, 1991.
- [OZK 97a] OZKAN C. S., NIX W. D., GAO H.
Strain relaxation and defect formation in heteroepitaxial $\text{Si}_{1-x}\text{Ge}_x$ films via surface roughening induced by controlled annealing experiments. *Appl. Phys. Lett.*, vol. 70, 1997, Page 2247, AIP.
- [OZK 97b] OZKAN C. S., NIX W. D., GAO H.
Strain relaxation and defect formation in heteroepitaxial SiGe films via surface roughening induced by controlled annealing experiments. *Applied physics letters*, vol. 70, 1997, Page 2247.
- [PAN 06] PANG Y., HUANG R.
Nonlinear effect of stress and wetting on surface evolution of epitaxial thin films. *Phys. Rev. B*, vol. 74, 2006, Page 075413.
- [PAS 08] PASCALE A., BERBEZIER I., RONDA A., KELIRES P. C.
Self-assembly and ordering mechanisms of Ge islands on prepatterned Si(001). *Phys. Rev. B*, vol. 77, 2008, Page 075311, American Physical Society.

Bibliography

- [PAU 04] PAUL D. J.
Si/SiGe heterostructures: from material and physics to devices and circuits. *Semiconductor Science and Technology*, vol. 19, n° 10, 2004, Page R75, IOP Publishing.
- [PCH 97] PCHELYAKOV O., MARKOV V., NIKIFOROV A., SOKOLOV L.
Surface processes and phase diagrams in MBE growth of SiGe heterostuctures. *Thin Solid Films*, vol. 306, n° 2, 1997, p. 299–306, Elsevier.
- [PEO 85] PEOPLE R., BEAN J.
Calculation of critical layer thickness versus lattice mismatch for GeSi/Si strained-layer heterostructures. *Applied Physics Letters*, vol. 47, 1985, Page 322.
- [PID 92] PIDDUCK A. J., ROBBINS D. J., CULLIS A. G., LEONG W. Y., PITT A. M.
Evolution of surface morphology and strain during SiGe epitaxy. *Thin Solid Films*, vol. 222, 1992, Page 78.
- [PIM 98] PIMPINELLI A., VILLAIN J.
Physics of Crystal Growth. Cambdrige University Press, 1998.
- [PRE 08a] PRESS D., LADD T. D., ZHANG B., YAMAMOTO Y.
Complete quantum control of a single quantum dot spin using ultrafast optical pulses. *Nature*, vol. 456, n° 7219, 2008, p. 218–221, Nature Publishing Group.
- [PRE 08b] PRESS D., LADD T. D., ZHANG B., YAMAMOTO Y.
Complete quantum control of a single quantum dot spin using ultrafast optical pulses. *Nature*, vol. 456, n° 7219, 2008, p. 218–221, Nature Publishing Group.
- [RAS 03a] RASTELLI A., VON KÄNEL H.
Island formation and faceting in the SiGe/Si(001) system. *Surf. Sci.*, vol. 532, 2003, Page 769.
- [RAS 03b] RASTELLI A., VON KÄNEL H., SPENCER B. J., TERSOFF J.
Prepyramid-to-pyramid transition of SiGe islands on Si(001). *Phys. Rev. B*, vol. 68, 2003, Page 115301, American Physical Society.
- [RAS 06] RASTELLI A., STOFFEL M., KATSAROS G., TERSOFF J., DENKER U., MERDZHANOVA T., KAR G. S., COSTANTINI G., KERN K., VON KÄNEL H., SCHMIDT O. G.
Reading the footprints of strained islands. *Microelecr. J.*, vol. 37, 2006, Page 1471.
- [RAT 04] RATTO F., ROSEI F., LOCATELLI A., CHERIFI S., FONTANA S., HEUN S., SZKUTNIK P.-D., SGARLATA A., DE CRESCENZI M., MOTTA N.
Composition of Ge(Si) islands in the growth of Ge on Si(111). *Appl. Phys. Lett.*, vol. 84, 2004, Page 4526, AIP.
- [REZ 10] REZAEV R., KIRAVITTAYA S., FOMIN V., RASTELLI A., SCHMIDT O.
Engineering self-assembled SiGe islands for robust electron confinement in Si. *Physical Review B*, vol. 82, n° 15, 2010, Page 153306, APS.
- [RIC 81] RICE J. R., CHUANG T.-J.
Energy Variations in Diffusive Cavity Growth. *J. Am. Ceram. Soc.*, vol. 64, 1981, Page 46, Blackwell Publishing Ltd.

- [SIM 10a] SIMMONS C. B., KOH T. S., SHAJI N., THALAKULAM M., KLEIN L. J., QIN H., LUO H., SAVAGE D. E., LAGALLY M. G., RIMBERG A. J., JOYNT R., BLICK R., FRIESEN M., COPPERSMITH S. N., ERIKSSON M. A.
Pauli spin blockade and lifetime-enhanced transport in a Si/SiGe double quantum dot. *Phys. Rev. B*, vol. 82, 2010, Page 245312, American Physical Society.
- [SIM 10b] SIMMONS C., KOH T. S., SHAJI N., THALAKULAM M., KLEIN L., QIN H., LUO H., SAVAGE D., LAGALLY M., RIMBERG A. et al.
Pauli spin blockade and lifetime-enhanced transport in a Si/SiGe double quantum dot. *Physical Review B*, vol. 82, n° 24, 2010, Page 245312, APS.
- [SPE 91] SPENCER B. J., VOORHEES P. W., DAVIS S. H.
Morphological Instability in Epitaxially Strained Dislocation-Free Solid Films. *Phys. Rev. Lett.*, vol. 67, 1991, Page 3696.
- [SPE 93] SPENCER B. J., VOORHEES P. W., DAVIES S. H.
Morphological instability in epitaxially strained dislocation-free solid films: linear stability theory. *J. Appl. Phys.*, vol. 73, 1993, Page 4955.
- [SPE 94] SPENCER B. J., MEIRON D. I.
Nonlinear evolution of the stress-driven morphological instability in a two-dimensional semi-infinite solid. *Acta Metall. Mater.*, vol. 42, 1994, Page 3629.
- [SPE 97] SPENCER B. J., TERSOFF J.
Equilibrium Shapes and Properties of Epitaxially Strained Islands. *Phys. Rev. Lett.*, vol. 79, 1997, Page 4858, American Physical Society.
- [SPE 05] SPENCER B. J., BLANARIU M.
Shape and Composition Map of a Prepyramid Quantum Dot. *Phys. Rev. Lett.*, vol. 95, 2005, Page 206101, American Physical Society.
- [SRO 89] SROLOVITZ D. J.
On the stability of surfaces of stressed solids. *Acta Metall.*, vol. 37, 1989, Page 621.
- [STO 95] STONEHAM A. M., JAIN S. C.
GeSi strained layers and their applications. Institute of Physics Publishing, 1995.
- [SUT 00] SUTTER P., LAGALLY M. G.
Nucleationless Three-Dimensional Island Formation in Low-Misfit Heteroepitaxy. *Phys. Rev. Lett.*, vol. 84, 2000, Page 4637.
- [SZK 04] SZKUTNIK P. D., SGARLATA A., NUFRIS S., MOTTA N., BALZAROTTI A.
Real-time scanning tunneling microscopy observation of the evolution of Ge quantum dots on nanopatterned Si(001) surfaces. *Phys. Rev. B*, vol. 69, 2004, Page 201309, American Physical Society.
- [SZK 07] SZKUTNIK P. D., SGARLATA A., BALZAROTTI A., MOTTA N., RONDA A., BERBEZIER I.
Early stage of Ge growth on Si(001) vicinal surfaces with an 8° miscut along [110]. *Phys. Rev. B*, vol. 75, 2007, Page 033305.

Bibliography

- [TAL 07] TALBOT D., DAY S. C. T. W. A., NEVER F. B. T., FROM TRASH C. E.
TR10: Nanocharging Solar. *Algae*, vol. 4, 2007, Page 17.
- [TER 92] TERSOFF J.
Missing dimers and strain relief in Ge films on Si (100). *Physical Review B*, vol. 45, n° 15, 1992, Page 8833, APS.
- [TER 02] TERSOFF *et al.* J.
Barrierless Formation and Faceting of SiGe Islands on Si(001). *Phys. Rev. Lett.*, vol. 89, 2002, Page 196104, American Physical Society.
- [THI 92] THIEL M., WILLIBALD A., EVERE P., LEVCHENKO A., LEIDERER P., BALIBAR S.
Stress-induced melting and surface instability of 4He crystals. *Europhysics letters*, vol. 20, n° 8, 1992, p. 707–713, EDP sciences.
- [TRO 00] TROMP R. M., ROSS F. M., REUTER M. C.
Instability-Driven SiGe Island Growth. *Phys. Rev. Lett.*, vol. 84, 2000, Page 4641.
- [TSA 87] TSAO J., DODSON B., PICRAUX S., CORNELISON D.
Critical Stresses for $\text{Si}_{\{x\}} \text{Ge}_{\{1-x\}}$ Strained-Layer Plasticity. *Physical review letters*, vol. 59, n° 21, 1987, p. 2455–2458, APS.
- [VAI 00] VAILIONIS A., CHO B., GLASS G., DESJARDINS P., CAHILL D. G., GREENE J. E.
Pathway for the Strain-Driven Two-Dimensional to Three-Dimensional Transition during Growth of Ge on Si(001). *Phys. Rev. Lett.*, vol. 85, 2000, Page 3672, American Physical Society.
- [VOI 01] VOIGTLÄNDER B.
Fundamental processes in Si/Si and Ge/Si epitaxy studied by scanning tunneling microscopy during growth. *Surface Science Reports*, vol. 43, n° 5, 2001, p. 127–254, Elsevier.
- [VOL 00] VOLPI F., PORTAVOCE A., RONDA A., SHI Y., GAY J., BERBEZIER I.
Nucleation and evolution of $\text{Si}_{1,\dot{x}}\text{Ge}_x$ islands on Si(001). *Thin Solid Films*, vol. 380, n° 1, 2000, p. 46 - 50.
- [VVE 10] VVEDENSKY D. D.
Oxford Handb Nanosci Technol, vol. 3. ed. A. V. Narlikar and Y. Y. Fu, Oxford University Press, Oxford, England, 2010.
- [WAN 08] WANG H., ZHANG Y., LIU F.
Enhanced growth instability of strained film on wavy substrate. *J. Appl. Phys.*, vol. 104, 2008, Page 054301, AIP.
- [WU 95] WU F., CHEN X., ZHANG Z. Y., LAGALLY M. G.
Reversal of Step Roughness on Ge-Covered Vicinal Si(001). *Phys. Rev. Lett.*, vol. 74, 1995, Page 574.
- [WUL 01] WULFF G.
Zur Frage der Geschwindigkeit des Wachstums und der Auflösung der Kristallfläschchen. *Z. Kristallogr.*, vol. 34, 1901, Page 449.

- [XIA 02] XIANG Y., E W.
Nonlinear evolution equation for the stress-driven morphological instability. *J. Appl. Phys.*, vol. **91**, 2002, Page 9414.
- [XU 12] XU X., AQUA J., FRISCH T.
Growth kinetics in a strained crystal film on a wavy patterned substrate. *J. Phys. : Condens. Matter*, vol. 24, 2012, Page 045002.
- [XU 13] XU X., AQUA J.-N., FRISCH T.
Growth of a strained epitaxial film on a patterned substrate. *Comptes Rendus Physique*, , 2013, Elsevier.
- [YAN 93] YANG W. H., SROLOVITZ D. J.
Cracklike Surface Instabilities in Stressed Solids. *Phys. Rev. Lett.*, vol. **71**, 1993, Page 1593.
- [YAN 04] YANG B., LIU F., LAGALLY M. G.
Local Strain-Mediated Chemical Potential Control of Quantum Dot Self-Organization in Heteroepitaxy. *Phys. Rev. Lett.*, vol. 92, 2004, Page 025502, American Physical Society.
- [ZHA 00] ZHANG Y. W.
Self-organization, shape transition, and stability of epitaxially strained islands. *Phys. Rev. B*, vol. **61**, 2000, Page 10388.
- [ZHA 10] ZHANG J., MONTALENTI F., RASTELLI A., HRAUDA N., SCOPECE D., GROISS H., STANGL J., PEZZOLI F., SCHÄFFLER F., SCHMIDT O. et al.
Collective shape oscillations of SiGe islands on pit-patterned Si (001) substrates: a coherent-growth strategy enabled by self-regulated intermixing. *Physical review letters*, vol. 105, n° 16, 2010, Page 166102, APS.
- [ZHO 96] ZHONG L., HOJO A., MATSUSHITA Y., AIBA Y., HAYASHI K., TAKEDA R., SHIRAI H., SAITO H., MATSUSHITA J., YOSHIKAWA J.
Evidence of spontaneous formation of steps on silicon (100). *Phys. Rev. B*, vol. 54, 1996, Page R2304, American Physical Society.
- [ZHO 03a] ZHONG Z., HALILOVIC A., FROMHERZ T., SCHAFFLER F., BAUER G.
Two-dimensional periodic positioning of self-assembled Ge islands on prepatterned Si (001) substrates. *Appl. Phys. Lett.*, vol. 82, 2003, Page 4779, AIP.
- [ZHO 03b] ZHONG Z., HALILOVIC A., MUHLBERGER M., SCHAFFLER F., BAUER G.
Ge island formation on stripe-patterned Si(001) substrates. *Appl. Phys. Lett.*, vol. 82, 2003, Page 445, AIP.
- [ZHO 07a] ZHONG Z., SCHWINGER W., SCHÄFFLER F., BAUER G., VASTOLA G., MONTALENTI F., MIGLIO L.
Delayed Plastic Relaxation on Patterned Si Substrates: Coherent SiGe Pyramids with Dominant {111} Facets. *Phys. Rev. Lett.*, vol. 98, 2007, Page 176102, American Physical Society.
- [ZHO 07b] ZHONG Z., SCHWINGER W., SCHÄFFLER F., BAUER G., VASTOLA G., MONTALENTI F., MIGLIO L.

Bibliography

Delayed Plastic Relaxation on Patterned Si Substrates: Coherent SiGe Pyramids with Dominant 111 Facets. *Phys. Rev. Lett.*, vol. 98, 2007, Page 176102, American Physical Society.